学位論文(要約)

Investigation of amorphous calcium carbonate (ACC) in biomineralization

(生体鉱化作用における非晶質炭酸カルシウム(ACC)の研究)

平成 24 年 12 月博士（理学）申請

東京大学大学院理学系研究科

地球惑星科学専攻

横尾　直樹

Abstract

Amorphous calcium carbonate (ACC) is the unique inorganic material only found as biomineral in nature. In order to deepen the understanding of biomineralization involved with ACC, two kinds of hard tissues, cuticle of terrestrial isopod and larval shells of mollusks, have been investigated in this thesis. The reason to select the former material is mainly to characterize the mineralogical or crystallographic features of crystalline calcium carbonate (calcite) transformed from ACC. The latter material was selected to elucidate the existence or nonexistence of ACC in the larval shells, through the detailed characterization of the microstructure of the shells at several stages after fertilization.

Previous studies reported that the cuticle of the terrestrial isopod, *Armadillidium vulgare*, at the intermolt stage consists of three calcified layers and one uncalcified layer; distal layer (calcite), transition zone (calcite), endocuticle (ACC), and membranous layer (uncalcified). The present study has revealed that calcite in the transition zone is crystallized from ACC and the calcite crystals have distinct features with respect to their crystal orientations; the crystals in the upper transition zone have the identical orientations to those of calcite in the distal layer, whereas the lower transition zone consists of nano-crystalline calcites with their ***c***-axis parallel to the organic fibers. Hence, calcite crystals in the upper transition zone are suggested to be formed by epitaxial growth, taking over the crystal orientation from the distal layer. In contrast, crystallization is regulated by organic fibers in the lower transition zone. These results suggest that the calcite transformed from ACC can have various crystallographic features, depending on the substrates or templates. On the other hand, considerable amounts of phosphorus were detected in the transition zone and endocuticle. Hence, as reported in previous studies of ACC formed in crustaceans, phosphorus compounds probably work as the stabilizer of ACC or inhibitor of the crystallization also in *A. vulgare*. Combined with the observations of the cuticle at several molt stages, the calcification and crystallization process in the cuticles of *A. vulgare* can be illustrated as in Figure 1.

５年以内に雑誌等で刊行予定のため、非公開とする。

Fig. 1. Schematic illustration of the cuticle formation processes in a molting cycle. (1) Organic membranes are formed under the old cuticle. (2) ACC deposits under the epicuticle. (3) ACC deposits continuously and the crystallization starts from the surface. (4) Organic fibers induce ACC crystallization at the lower transition zone. (5) Both of the crystallization processes from the surface and along the organic fibers are completed.

Larval shells of *Pinctada fucata* and the other species have been investigated to elucidate the shell microstructure and possibility of the existence of ACC during their developments. The shells were mainly investigated using transmission electron microscopy (TEM) with the specimens prepared using the focused-ion-beam (FIB) technique. A three-layered structure has been identified in the larval shell of *P. fucata*, as reported in previous studies. From detailed TEM analyses, each layer has the following characteristic structure;

(1) The outer prismatic layer contains dense multiple {110} twins and few grain boundaries (Fig. 2).

(2) The middle globular layer is actually the mixture of the areas with multiple {110} twins and with a polycrystalline feature. However, the ***c***-axes of the aragonite crystals are oriented normal to the surface, regardless of such structural difference.

(3) The inner prismatic layer consists of "prismatic crystals" with distinct grain boundaries.

５年以内に雑誌等で刊行予定のため、非公開とする。

Fig. 2. Results of the observation of 18 h shell by SEM/TEM. (a) Outer appearance. (b) Cross-sectional TEM image of the initial calcified layer. (c) SAED pattern from the circle in (b). (d) Plane-view image of the layer. (e) SAED pattern from the plan-view specimen, indicating dense {110} multiple twins. (f) Magnified image of (d).

Although the analysis of the shell microstructure was not as complete as that for *P. fucata*, I have investigated the larval shells of other three species selected from seawater Gastropoda, freshwater Bivalvia, and freshwater Gastropoda. All of them have a three- layered structure, all of which consist of aragonite whose ***c***-axes are oriented normal to the shell surface. Hence, the basic design of the larval shell is very close among these species, or in Bivalvia and Gastropoda. During these analyses, I did not find ACC or any structures which suggest the existence of ACC as a precursor phase in the larval shells of *P. fucata* and other species. Considering the results for *A. vulgare* and characterization of synthetic ACC (Appendix), the transformation of ACC to aragonite by the FIB process seems unlikely.

要旨

非晶質炭酸カルシウム(ACC)は炭酸カルシウムの含水多形のひとつであり、自然界においては生物中でのみその存在が確認される。特に近年、生物中での ACC の報告が多くなされており、炭酸カルシウムから成る殻の形成プロセスを解明するためには、ACC についてより深く理解する必要がある。本研究では、ACC の殻形成に対する関与を調べるため、陸生甲殻類の外骨格および軟体動物幼生の殻について観察・分析を行った。これらの試料は、これまでに ACC を前駆体とした炭酸カルシウム結晶形成が行われているという示唆がなされている。特に陸生甲殻類では、最外層(distal layer)の下部に形成される遷移層(transition zone)が脱皮直後に ACC から成っていることが示されており、ACC-カルサイトの結晶化について、その特徴を理解するのに適当な試料であるといえる。また、軟体動物幼生の殻では､現在のところ ACC を前駆体としてアラゴナイトが形成されるという説が有力であるが、未だ ACC の有無について明確な結論は出ておらず、より詳細な殻微細構造の観察や結晶学的な分析が必要である。

オカダンゴムシ *Armadillidium vulgare* の脱皮間期における外骨格は、先行研究により、最外層、遷移層、内皮層(endocuticle)という 3 つの石灰化した層と、膜性板(membranous layer)という有機物のみから成る層がある。このうち、最外層と遷移層はカルサイトから成り、内皮層は ACC を安定的に保持するとされる。本研究の観察により、これまで遷移層として示されてきた層が、構造などの違いから上部遷移層(upper transition zone)と、下部遷移層(lower transition zone)とに分けられることなどが示された。上部遷移層では、さらに外側に形成される板状カルサイト層からエピタキシャル成長することで方位の揃った比較的大きな結晶を形成するのに対し、下部遷移層では、層内に含まれる、キチンを主成分とした有機繊維に方位を制御された微細なカルサイト結晶によって層が形成されることがわかった。遷移層は脱皮直後には ACC から成ることが先行研究により示されており､ACC が結晶化する際、エピタキシャル成長する場合と繊維に沿った結晶化をする場合との少なくとも二つ

のパターンが存在すると示唆された。元素分析の結果から、内皮層における ACC の安定化には、リンの化合物が大きく関与していると示唆された。 さらに、脱皮中試料における観察結果から、遷移層の外側に形成される最外層も、ごく初期には ACC を保持し、それが前駆体となってカルサイトが形成されることがわかった。これらの結果から、殻は Fig. 1 のような形成プロセスをたどると考えられる。

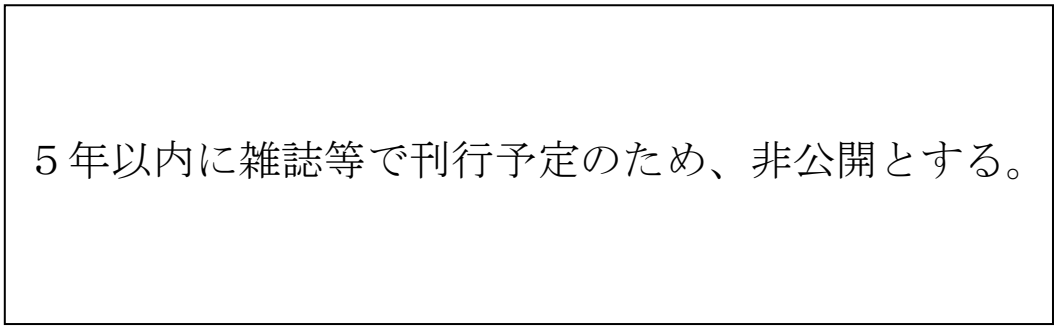

Fig. 1. 本研究の結果などから推測されるオカダンゴムシの殻形成プロセス。(a) 脱皮直前の新殻は有機物のみから成る。 (b) 殻の外表面側に ACC が沈着する。(c) ACC がさらに沈着し、外表面側から結晶化が開始される。(d) 外表面側からの結晶化が進行するほか、繊維に沿った結晶化も開始される。(e) いずれの結晶化もほぼ終了し、下部には ACC が安定的に存在する(脱皮間期)。

アコヤガイ *Pinctada fucata*、および他三種の幼殻について、微細構造の共通性や ACC の有無について調べた。殻構造は主に集束イオンビーム装置(FIB)を用いて試料を作製し、透過型電子顕微鏡(TEM)を用いて観察した。 その結果、アコヤガイ幼殻は最終的に以下に示すような三層構造を呈すると示された。

(1) {110}双晶を密に含み結晶粒界をもたない、柱状コントラストを示す層(外層) (Fig. 2)。

(2) {110}双晶を密に含む領域と多結晶体領域が混在する中層。

(3) 明瞭な結晶粒界を有する柱状結晶の集合体である内層。

いずれの層も ***c*** 軸が殻表面に対して垂直に配向するアラゴナイト結晶から成り、ACC の存在は確認されなかった。

５年以内に雑誌等で刊行予定のため、非公開とする。

Fig. 2. 受精後 18 時間試料の TEM 観察結果。(a) SEM による観察結果。黒枠は FIB で断面試料を作製した部位。(b) (a)の黒枠から作製した試料の断面 TEM 像。(c) (b)の白円部から得た電子回折パターン。(d) 平面試料の TEM 像。 (e) (d)の領域から得た電子回折パターン。(f) 平面試料の高分解能像。

その他の三種(海水生巻貝、淡水生二枚貝、淡水生巻貝)の構造を観察して比較したところ、全体的な構造は類似しているものの、巻貝綱と二枚貝綱との間で、主に中層の構造に違いがみられた。二枚貝綱の二種では中層は比較的粒状なのに対し、巻貝綱の二種では殻表面に平行に近い方向への伸長がみられた。ただし、いずれの種においても ***c*** 軸が殻表面に垂直に配向するアラゴナイト結晶から成り、ACC は確認されなかった。オカダンゴムシにおける ACC や Appendix の合成 ACC が TEM で観察できていることから、貝類幼生においてのみ ACC が FIB 等のビームダメージによって結晶化することは考えにくく、貝類幼生において ACC は存在しないと考えられる。

Preface

Biominerals are inorganic materials which are formed by organisms at the inside or outside of their organic bodies. It is suggested that organic substances contribute significantly to the forming process of biominerals. Accordingly, biominerals often have various unique aspects which are not taken by abiotic processes, even if the materials themselves are the same. Calcium carbonate ($CaCO_3$) is well known as one of the major biominerals. Two anhydrated polymorphs, calcite and aragonite, and amorphous calcium carbonate (ACC) are common as $CaCO_3$ biominerals. Recently, the role of ACC as a precursor phase of crystalline $CaCO_3$ has been proposed. Hence, three modes of formation processes are proposed for the biomineralization of $CaCO_3$; (1) $CaCO_3$ crystals precipitate directly from a supersaturated fluid, (2) ACC precipitates from a supersaturated fluid as a precursor then transformed to crystalline forms, and (3) ACC precipitates from a supersaturated fluid but does not transform to crystals by some factors.

Many previous studies dealing with biotic ACC concentrated only the identification of ACC and, for instance, the structural difference of crystalline forms between the modes (1) and (2) was not described to date. Besides, in some organism, it is suggested that ACC transforms not to calcite but to aragonite, the metastable phase of $CaCO_3$. Hence, for the thesis, I selected investigation of the structural aspects of biotic ACC and crystalline calcium carbonates transformed from ACC, in order to advance the understanding of biomineralization related to ACC.

In Chapter 1, I have thoroughly reviewed previous studies dealing with ACC, irrespective of biotic or synthetic ones, to understand comprehensively the structures and properties of ACC for my experiments and discussion in this thesis.

As the investigations in the thesis, I have first selected terrestrial isopod, *Armadillidium vulgare*, in order to elucidate the formation processes and structural characteristics of crystalline $CaCO_3$ (calcite) transformed from ACC. *A. vulgare* is thought to have three modes of the formation processes of calcite as mentioned above. This is the content of Chapter 2.

Next, larval molluscan shells of the pearl oyster, *Pinctada fucata,* and other three species have been investigated to elucidate the shell microstructure and possibility of the existence of ACC during their formation. The shells were mainly investigated using transmission electron microscopy (TEM) with the specimens fabricated with the focused-ion-beam (FIB) technique. A three-layered structure has been identified in the larval shell of *P. fucata*, and their microstrucrures were elucidated comprehensively. Although the analysis of the shell structure was not so complete as that for *P. fucata*, I have investigated the larval shells of three other species selected from seawater Gastropoda, freshwater Bivalvia, and freshwater Gastropoda. These results have been described in Chapter 3.

Finally, during the period in my doctoral course, I investigated the effect of magnesium addition on the structure and properties of synthetic ACC. In particular, the crystalline phases transformed from ACC are strongly dependent on the content of Mg in ACC, when the ACC is crystallized in a humid condition. Although obtained results are not linked tightly to the other investigations dealing with biotic ACC, they have considerable relevance to the main conclusion of this thesis. Hence, I have attached this study as “Appendix” at the last part of the thesis.

Table of contents

Chapter 1

Background of the thesis; amorphous calcium carbonate (ACC) in biomineralization

1-1. Biominerals and Biomineralization

Biominerals are inorganic materials at the inner or outer region of organisms, formed by the organisms. Actually, biominerals are common in a variety of organisms, and play various important roles for their activities such as locomotion, protection, storage and sensing. The mineral species of biominerals which have such various and important roles are also diverse. Probably they were selected to meet the functions of biominerals and/or environments in the history of life. For example, vertebrates form hydroxyapatite ($Ca_5(PO_4)_3(OH)$) in bone and teeth, mollusks form calcium carbonate minerals ($CaCO_3$) in shells, and diatoms form amorphous silica (SiO_2). In spite of a number of previous researches so far, there are still many unsolved problems with respect to biominerals and biomineralization. For instance, it was suggested that organic matters in biominerals, although their amounts are very small, play important roles for the formation of biominerals in various organisms (*e.g.* Addadi and Weiner, 1997; Kayano *et al.* 2011), and this is the reason why biominerals possess unique structures and textures, and have usable properties.

1-2. Polymorphs of Calcium Carbonates

Calcium carbonate ($CaCO_3$) is one of the most popular biominerals. $CaCO_3$ has three anhydrous (calcite, aragonite and vaterite) and two hydrated (monohydrocalcite and ikite) crystalline phases at the ambient temperature and pressure (Clarkson *et al.*, 1992). Beside them, amorphous calcium carbonate (ACC) can be formed. Generally ACC is hydrated. Calcite and aragonite are major phases for calcium carbonate biominerals because of their superior thermodynamic stability compared to other crystalline forms and ACC. For example, sea urchin, crustacean and a part of seashells form calcite shells,

and other seashells and corals form aragonite shells. Such strict polymorph selection of calcium carbonate by organisms is often called “calcite-aragonite problem”, and its mechanism is still not clear.

1-3. Properties of ACC

ACC is hydrated $CaCO_3$ with variable water content. Kojima *et al.* (1993) and Lam *et al.* (2007) reported its formula as $CaCO_3 \cdot 1.5H_2O$. ACC transforms to a crystalline phase, generally to calcite, rapidly (in minutes to hours) if it is suspended in aqueous solution (Rodríguez-Blanco *et al.*, 2011). ACC has distinct thermal stability and solubility compared with anhydrate crystalline phases. Kojima *et al.* (1993) and Koga *et al.* (1998) reported that the transition from ACC to calcite occurs around 350 °C, by analyzing synthetic ACC using TG-DTA.

Solubility of ACC is much higher than crystalline $CaCO_3$, especially aragonite and calcite (*e.g.* Brečević and Nielsen, 1989; Gal *et al.*, 1996). Gal et al. (1996) reported the solubility products for the various forms of calcium carbonate.

From Gal et al. (1996), it is calculated that ACC dissolves about 122 times more than calcite, and about 87 times more than aragonite. The results by Brečević and Nielsen (1989) are nearly the same as those.

1-4. Synthesis of ACC

Several synthetic conditions were reported for the formation of ACC using $CaCl_2$ and Na_2CO_3. For example, Ogino *et al.* (1987) and Rodríguez-Blanco *et al.* (2008) synthesized ACC by mixing 10 mM $CaCl_2$ and 10 mM Na_2CO_3 at a temperature less than 1 $^{\circ}$C. Koga *et al.* (1998) mixed 100 mM $CaCl_2$ and 100 mM Na_2CO_3 with 0 - 2.0 mM NaOH. Gal *et al.* (2010) synthesized ACC using pre-cooled 100 mM $CaCl_2$ and

100 mM Na_2CO_3. Kojima *et al.* (2012) made ACC particles by mixing 800 mM $CaCl_2$ and 800 mM Na_2CO_3 under 2 MHz ultrasonic conditions. ACC formed by this method was reported to have a composition of $CaCO_3 \cdot 0.5H_2O$. Table 1 shows examples of the conditions for ACC syntheses. In any cases, synthesis of ACC requires a low temperature and/or extremely-supersaturated solution with respect to calcium carbonate.

Table 1. Examples of ACC synthesis methods. pcT: pre-cooled temperature, rT: reaction temperature, RT: room temperature.

	$CaCl_2$ concentration	Na_2CO_3 concentration	pcT (°C)	rT (°C)	note
Ogino *et al.* (1987)	10 mM	10 mM	1	1	
Koga *et al.* (1998)	100 mM	100 mM with NaOH 0-2 M	RT	5	
Gal *et al.* (2010)	100 mM	100 mM	0-4	RT	2 ml reaction volume
Kojima *et al.* (2012)	800 mM	800 mM	RT	RT	with 20 vol.% methanol, 2.4 MHz supersonic
Bots *et al.* (2012)	1 M	1 M	RT	RT	with rapidly mixing

1-5. Morphology of ACC

Generally ACC adopts aggregates of fine particulates, independent on the synthetic methods. The particle size of ACC is dependent on the concentrations of solutions. The particle size depending on the concentration of $CaCl_2$ with equimolar dimethyl carbonate (DMC) and NaOH was investigated by Gorna *et al.* (2008). For example, when 20 mM $CaCl_2$ with DMC and 20 mM NaOH were mixed, the average particle size was 790 nm. When $CaCl_2$ concentration increased to 60 mM, the average particle size decreased to 490 nm. When both $CaCl_2$ and NaOH concentrations were 100 mM, the particle size became 400 nm, the smallest in the experiments.

1-6. Structures of ACC

Because ACC is amorphous, the information of its structure is rather limited, compared to crystalline counterparts. Recently, two types of ACC have been suggested, "calcitic" ACC and "vateritic" ACC by Gebauer *et al.* (2008). They investigated the amount of free ion products of ACC synthesized with various pH conditions, and suggested that ACC can be separated into two types. Up to pH = 9.50, the free ion products are ~3.1×10^{-8} M^2, and pH = 9.75 ~ 10.00, the free ion products are ~3.8×10^{-8} M^2. The former is termed ACC-I, and the latter ACC-II. Gebauer *et al.* (2010) analyzed these ACC using NMR and EXAFS and indicated that ACC-I and ACC-II are the precursor phases of vaterite and calcite, respectively. They show schematic classical model and novel model from their works. In the classical model, clusters are not considered during pre-nucleation. In constant, the novel model (Gebauer *et al.*, 2008, 2010) considers the stable clusters from ionic solutions. They mentioned that the processes between nucleation stages are not clear in the novel model. In the post-nucleation stage, the novel model suggests that the thermodynamics and kinetic controls are not concerned to crystalline polymorphs; if the amorphous phase is ACC-I or ACC-II, the crystal becomes calcite or vaterite, respectively.

Bots *et al.* (2012) analyzed ACC crystallization at a rapid time scale (the order of seconds), using small- and wide-angle X-ray scattering (SAXS/WAXS). Three stages in ACC crystallization to vaterite are suggested. First, hydrated and disordered ACC is formed and it rapidly changes into more ordered, dehydrated ACC. Second, ACC dissolves and crystallizes into vaterite. The third stage is controlled by "Ostwald ripening" of the vaterite particles. After that, the vaterite particles change into calcite particles by phase transition with dissolution and re-precipitation processes.

1-7. Experiments to stabilize ACC

As described above, ACC is unstable in aqueous solution. Hence, it is considered that ACC is hard to keep in organisms. A number of laboratory experiments were conducted to find the method to stabilize ACC. For example, Sawada (1997) suggested that macro molecules of phosphate stabilize ACC strongly. Bentov *et al.* (2010) suggested that two single phosphoamino acids, phosphoserine and phosphothreonine, work to stabilize ACC, although the other two phosphoamino acids, phosphorylated serine and phosphotyrosine do not contribute to the stabilization of ACC. Stable ACC was also formed by Maruyama *et al.* (2011) by mixing calcium aspartate solution with methanol, and the suspension was maintained at 50 °C for 24 hours after filtering. The suspention was formed by bubbling CO_2 to supply carbonate ions. They suggested that small molecules, aspartic acid stabilized ACC.

About the stabilization of ACC, two inhibition processes were proposed so far; the inhibition of dissolution of ACC and inhibition of nucleation of crystalline phases. Becker *et al.* (1974) investigated amorphous calcium phosphate (ACP), and suggested that ATP (adenosine triphosphate) stabilizes ACP by inhibition of nucleation. Some macromolecules rich in GlX (glutamine and glutamine acid), Glysine and Serine are suggested to work as a poison for the nucleation of crystalline $CaCO_3$ phases like ACP and ATP (Aizenberg *et al.* 1996). However, the detail of the mechanism is not clear. Kellermeier *et al.* (2010) indicated that ACC stays stably under silica-rich environments with alkaline solutions. From TEM observation, the size of ACC became smaller when the silica concentration was higher, and the silica formed shells around ACC particles. In their proposed model, ACC particles form pH-gradients around their surfaces by dissociation of bicarbonate ions, and silica species accumulate around them polymerize

and become a skin around the ACC particles. The ACC particles are bonded to each other with the silica skin. Calcite crystals are formed from ACC with the dissolution-precipitation process up to 1000 ppm of silica concentrations. If the concentration is over 1000 ppm, the ACC cannot dissociate and crystallize.

The particle-size dependence of stability of ACC by poly-aspartic acid was investigated in Nudelman *et al.* (2010). When the particles up to 100 nm, it leads to stabilization of ACC, and larger and uncoated particles by poly aspartic acid are changed into crystalline $CaCO_3$. Thus, in this report, they discussed that ACC particles are stabilized when something (in this case, poly aspartic acid) coats them. Some studies controlled the crystallization of ACC by the addition of organic matrices, from the view point of biomimetics. Bassett *et al.* (2012) is one of them which added fibrous organic matrices into ACC to consider its effect on the crystallization. They investigated the influence of biopolymer gels for $CaCO_3$ mineralization. If there are collagen hydrogels abundantly (0.2 to 14.1 wt%), 18 wt% of $CaCO_3$ remains as ACC.

1-8. ACC in organisms

Although its occurrence is far less than those of calcite and aragonite, ACC is definitely formed as biominerals in nature. As mentioned above, insides of organisms or environments where they live are generally in a wet condition and ACC must be unstable and transforms to a crystalline form. Moreover, in laboratories, a low temperature and/or extremely-supersaturated solution are required to synthesize ACC, which seems not realistic in organisms. Hence, some mechanisms should exit for the “stabilization” of ACC, also in biomineralization. Several studies suggested that some kinds of materials are used in organism to form ACC and/or prevent the crystallization

of ACC; small phospho-organic molecules (Sato *et al.*, 2011), phosphoproteins (Bentov *et al.*, 2010), and magnesium Asp-rich compounds (Tao *et al.*, 2009).

As an example, the gastrolith of crayfish is made of ACC and some organic matrices (Hikida, 2002, Master thesis). Crayfish forms gastrolith to preserve Ca^{2+} during the molting cycle, and after molting, the gastrolith is dissolved probably by acidic body fluid to use Ca^{2+} for the new exocuticle. In this case, because of its high solubility, adoption of ACC is reasonable. Moreover, a very large surface area of ACC owing to its low density, particulate structure is usable for rapid dissolution to make a new skeleton. However, as inorganic ACC transforms easily to crystalline phases in water-rich conditions, there must be some mechanism to keep ACC in gastrolith for a certain period. Sato *et al.* (2011) reported that phosphoenolpyruvate ($C_3H_5O_6P$; PEP) and 3-phosphoglycerate ($C_3H_7O_7P$; 3PG), which are glycolytic intermediates, work as ACC former/stabilizer as well as phosphoric acid in the gastrolith.

1-9. ACC as a precursor phase of crystalline forms

With respect to the formation pathway of crystalline calcium carbonates, it was considered previously that calcite and aragonite crystals precipitate directly from supersaturated fluid in biomineralization (Calvert and Mann, 1988). However, several recent studies suggested that in some organisms ACC precipitates initially, as a precursor phase of $CaCO_3$ crystals (*e.g.* Addadi *et al.*, 2003; Levi-Kalisman *et al.*, 2002; Politi *et al.*, 2008). For example, Politi *et al.* (2004) observed the reshaping region of sea urchin spicule, and advocated that ACC is formed there as a precursor phase of calcite. Gilis *et al.* (2011) suggested that calcite of sponge spicule is transformed from ACC precursor phase. In crustaceans, it is thought that ACC is almost certain to exist in

exocuticle. Dillaman *et al.* (2005) investigated the exocuticle of blue crab, and suggested that ACC exists as a precursor phase of calcite. In terrestrial isopods such as pill bugs, the intermolt cuticles consist of calcite in the outer layer, and ACC exists beneath this layer (Hild *et al.*, 2008). Neues *et al.* (2011) observed the change of the cuticles of terrestrial isopods during the molt-cycle, and suggested that a part of the cuticles consists of ACC as a precursor phase, as well as "stabilized" ACC.

Recently, several research groups claim that larval shells of mollusks contain ACC as a precursor phase. Previously, it was the accepted view that the all molluscan larval shells consist of only aragonite, regardless whether adult shells are made of calcite or aragonite (*e.g.* Taylor *et al.*, 1969; Waller, 1981; Watabe, 1988; Castilho *et al.*, 1989; Medaković *et al.*, 1989). However, from the years around 2000, some papers suggested the existence of ACC as a precursor phase of aragonite (*e.g.* Hasse *et al.*, 2000; Weiss *et al.*, 2002; Marxen *et al.*, 2003). Although this new idea is becoming accepted, Kudo *et al.* (2010) reported that the larval shell of oyster consists of only aragonite and ACC was not found, from the observation by transmission electron microscopy (TEM), with the sample preparation by a focused ion beam (FIB) instrument. Hence, the issue whether molluscan larval shells contain ACC or not has not been solved yet. If mollusks form ACC as a precursor phase in their larval shells, they may be seriously affected by the environmental change predicted in future. Orr *et al.* (2005) reared a kind of pteropod, *Clio pyramidata* in acidic seawater which is predicted at the year around 2050 to 2100. They reported that the shell of *C. pyramidata*, which is made of aragonite, showed notable dissolution during only two days rearing. As described above, ACC dissolves much more than aragonite. If the molluscan larvae form ACC as a precursor phase, they will not be able to form the shells in this century. Accordingly, existence/nonexistence

of ACC in the molluscan larval shells is an urgent issue to be concluded.

1-10. Purpose of this thesis

Under such understanding and unsolved problems with respect to biogenic ACC, I have been interested in the following issues.

1) As mentioned above, it is certain that ACC is formed initially as a precursor phase and transformed to a crystalline form (calcite) in crustaceans. Does such calcite express any characteristic mineralogical or crystallographic features such as grain size distribution, preferred crystal orientation, defect density, etc. which are often well regulated in biominerals?
2) Kudo *et al.* (2010) first reported detailed mineralogical characterization of the larval shell of oyster using TEM and FIB, and did not find ACC in the several stages of the larval shell. However, it is the result of only one species. Before discussing the existence of ACC, it seems important to observe other molluscan larval shells, to find their common and/or uncommon microstructures, as a descriptive study.

From these interests and questions, I first selected the investigation of the microstructure of the cuticle of a pill bug, *Armadillidum vulgare*, as the representative of ACC-bearing crustaceans, for my thesis research. This is described in Chapter 2 of the thesis, as “Structural analysis of *A. vulgare* cuticle”. Second, I adopted the structure analyses of several larval shells of mollusks, as another thesis research. The result is described in Chapter 3, as “Structural analysis of larval shells”. In the chapter, I described in detail the results for the larval shell of the pearl oyster, *Pinctada fucata*, because of the importance of this species for the pearl industry and related many

previous works for the species. Moreover, results for other four species, including seawater/freshwater snails and freshwater bivalves, are described. In the chapter, beside these structural descriptions, I refer the possibility of existence of ACC in these shells. Finally I summarize my whole researches at the end of the thesis, considering the contribution of this thesis for the understanding of biogenic ACC.

Chapter 2

Structural analyses of *A. vulgare* cuticle

2-1. Introduction

2-1-1. Pill bug and its molt cycles

Pill bug, a kind of arthropod, is a collective term for organisms which curl up to guard against external irritation. In Japan, three genera of pill bugs, *Armadillidium*, *Tylos*, and *Vinezillo* (Aoki, 1991) are living. They are omnivorous, but feed fallen leaves ordinarily. Isopods grow up by molting cuticle or exoskeleton, and they have unique characteristics in the molt cycle. They molt first the posterior half and after within one day, molt the anterior half of the shell. *Porcellio scaber*, a kind of terrestrial isopod, basically molts about every 5 to 6 weeks (Zidar *et al.*, 1998; Ziegler *et al.*, 2005). The molting cycle is divided into four stages; inter-molt stage (the normal stage between molting), premolt stage (just before molting), intramolt stage (during molting), and post-molt stage (just after molting) (Ziegler and Merz, 1999; Ziegler *et al.*, 2005, Becker *et al.*, 2003). Isopods first transport Ca^{2+} and HCO_3^- ions from the old posterior cuticle to anterior sternite (a platy hard tissue formed at the ventral region) across the posterior epithelium and into the hemolymph (collective term for body fluid of crustaceans), and storage those ions as ACC at the premolt stage. During intramolt (after posterior molting), Ca^{2+} and HCO_3^- ions stored at anterior cuticle and sternite are transported to the new posterior cuticle across the hemolymph, and forms new calcified cuticle (Ziegler *et al.*, 2002; Becker *et al*., 2003). Although they can resorb only about 20 % of all Ca^{2+} ions through the hemolymph, the rest of Ca^{2+} ions is acquired by ingestion of exuvia (Ziegler *et al.*, 2007).

2-1-2. Previous analyses of shell structures and its formation processes

In crustaceans, the structures, components, and elements distribution in the cuticle are

extremely variable among species and habitat environments (Hild *et al*. 2009). About the components in the cuticles of terrestrial isopods, Becker *et al.* (2005) estimated them using TG (Thermo-Gravimetry), AAS (Atomic Absorption Spectroscopy), and XRD (X-ray diffractometry) in the cuticles in *P. scaber* and *A. vulgare*. They suggested that the cuticle consisted from 12 wt% Mg-calcite, 59 wt% ACC, 11 wt% HAP (hydroxyapatite) / ACP (amorphous calcium phosphate) and 13 wt% organic matrices in dry condition. In *P. scaber*, ACC (38 wt%) is less than *A. vulgare*, and organic matrices (14 wt%) more than *A. vulgare*.

Raabe *et al.* (2005, 2006) analyzed the shell structure of an American lobster, *Homarus americanus*. They suggested that there are three calcified layers, epicuticle, exocuticle, and endocuticle, and one uncalcified layer, membranous layer. The epithelial cells exist under the membranous layer. They also suggested that exocuticle and endocuticle contains considerable amounts of organic matrices, mainly composed of chitin fibers, with a twisted plywood structure. This is a structure which consists of helicoidal stacks of α-chitin–protein planes that are gradually rotated about their normal axis. As the layer goes from the endocuticle to the membranous layer, the thickness of the sub layer becomes thinner gradually (3 μm in the top of endocuticle, 0.3 μm in the end of membranous layer). As shown later, this organic structure is also found in isopods.

Pore canals also exist in the terrestrial isopod cuticle. They probably work as pathways of some materials between the epidermal cells under membranous layer and cuticle reciprocally (Nagasawa, 2011). Some researchers observed these canals mainly using SEM and STEM (Scanning Transmission Electron Microscopy), and suggested that the pore canals were observed from the proximal exocuticle to the whole

endocuticle in the decalcified cross-sectional samples. From comparison between calcified and decalcified sample, pore canals are filled with organic fibers and $CaCO_3$. The organic fibers are aligned along the pore canals (*e.g.* Seidl *et al.*, 2011; Seidl and Ziegler, 2012).

Hild *et al*. (2008) investigated the inter-molt stage cuticle of *A. vulgare* using SEM. The cuticle consists of epicuticle, exocuticle, endocuticle and membranous layer. In Raabe *et al.* (2005, 2006), epicuticle means the outer smooth layer, but many reports indicate epicuticle as the outermost organic membrane (*e.g.* Hild *et al.*, 2008; Nagasawa, 2011). In this thesis, I call the outermost membrane epicuticle. Exocuticle is composed of two layers: distal layer and transition zone (*e.g.* Hild *et al.*, 2008; Seidl *et al.*, 2011). The transition zone was suggested to have a sub structure with blocky appearance. It is thought that this layer contains chitin and protein (Romano *et al.*, 2007).

Using Raman spectroscopy, Hild *et al.* (2008) investigated the cuticles of *P. scaber* and *A. vulgare* in the inter-molt stage, and suggested that calcite exists only in exocuticle and endocuticle is made of ACC. $CaCO_3$ does not exist in the membranous layer but only organic components. From single spectrum and line scan data, both exocuticle and endocuticle contain chitin fibrils.

Tao *et al.* (2009) analyzed the molt cycle of *A. vulgare* using SEM, TEM, XRD, Fourier-Transform Infrared spectrometry (FT-IR), Thermo Gravimetry Analyzer (TGA), Raman spectroscopy. At the early intra-molt stage, the new exocuticle has many spherical particles of 500 nm in diameter (stage 2 in Tao et al., 2009). Both selected-area electron diffraction (SAED) pattern and FT-IR confirmed that these particles are amorphous (stage 2). However, weak calcite peaks in XRD in this stage suggest that the cuticle begins to crystallize into calcite (stage 2). In stage 3, calcite

transformed from ACC is abundant. Finally no amorphous phase is detected (stage 4). This result indicates that the exocuticle crystallizes completely in stage 4. In stage 5, ACC is detected again by XRD.

Neues *et al*. (2011) analyzed the cuticle during eight different stages of the molting cycle of *P. scaber* mainly using micro Raman spectroscopy to determine the mineral phase distribution and the composition. After 1 hour from the posterior molt, the new posterior cuticle forms calcite of only 200-300 nm thick from the surface and about 4 μm calcified layer. After 1-2 days from the posterior molt, the surface layer consisting of calcite increases, and the layer made of ACC also increases. They estimated the total amount of $CaCO_3$ (computed by AAS data), Mg-calcite (Rietveld analysis), and the amount of ACC which was computed as the difference between the contents of $CaCO_3$ and crystalline Mg-calcite. From these results, it is suggested that ACC transforms to calcite in molting cycle.

2-1-3. Purpose of this study

As described in several previous works, both calcite and ACC exist in *A. vulgare* cuticle and a portion of ACC transforms into calcite. It is likely that calcite in the distal layer is formed directly from a supersaturated body fluid, and calcite in the transition zone is transformed from ACC as a precursor of calcite. Generally, previous studies characterized the cuticle of isopods using XRD, SEM and Raman spectroscopy, and analyses using TEM which is superior to reveal the fine mineralogical and crystallographic structures were seldom. As mentioned in the previous chapter, one of my interests is to find characteristics of calcite transformed from ACC precursor and this purpose should be attained by analyzing the exo- and endocuticles in various molt

stages by TEM. Of course, I will to use other analytical techniques such as XRD, SEM with electron back-scatter diffraction (EBSD) and X-ray chemical analysis, etc., for more comprehensive understanding of the mineralogical features of calcium carbonates in the cuticles.

2-2. Materials and Methods

2-2-1. Materials

Living *Armadillidium vulgare* were sampled in Nagareyama city, Chiba prefecture and bred at room temperature. Before using for experiments, the organisms were fixed by 100 % ethanol (EtOH; Wako Pure Chemical). Intermolt stage samples were dried directly when they were used for experiments. Because the cuticle was so soft, the molting samples were freeze-dried before experiments. The freeze-dry method is described in 2-2-2.

2-2-2. Sample preparations

1. Freeze-dry

The freeze-dry method was used for soft cuticles using t-buthanol as described below;

i. Replace the fixation solution from 100 % EtOH to 50 % EtOH + 50 % t-buthanol (stored for 30 minutes)
ii. Replace the solution to 25 % EtOH + 75 % t-buthanol (stored for 30 minutes)
iii. Replace the solution to 100 % t-buthanol (stored for 30 minutes at 30 °C)
iv. Changes the solution to new 100 % t-buthanol, and freeze at 4 °C (stored for 30 minutes)
v. Dry by evacuation using a rotary pump

2. XRD

Two types of samples were prepared for XRD; non-destructive sample and powdered sample. For the non-destructive sample, peeled dorsal cuticles were pasted on a glass

slide using double-stick tape. Dried dorsal cuticles were powdered with an agate motor and pestle. The XRD measurement was performed using Rigaku Ultima^{+} diffractometer with graphite-monochromated CuKα radiation and RINT 2000 analytical system. The sampling interval and scan speed were 0.02^{o} and 5^{o}/min, respectively.

3. Polished sample preparations

The intermolt cuticles were embedded in epoxy resin (Epocure; BUEHLER), cut by a diamond wheel saw (ISOMET; BUEHLER), then the surface was polished using corundum (C1000, C3000, C6000; Maruto), diamond paste (DP-paste 1μm; BUEHLER), and colloidal silica (MasterMet2; BUEHLER) in this order.

4. Broken-sectional sample preparations

The cuticles were cut in sagittal directions using a razor blade, and the soft body was removed from the cuticles. The cuticles were fixed onto a resin slice of 0.1 ~ 0.5 mm with epoxy resin. Intermolt and early, middle and late stages of molt samples were prepared by this method.

Some cuticles were broken along the sagittal directions, and decalcified by 1N hydrochloric acid (HCl; Wako Pure Chemical) for one week. Then they were fixed onto resin stage. Other samples were bleached by an undiluted solution of sodium hypochlorite solution (NaClO; Wako Pure Chemical) for several duration periods.

5. Coating for SEM experiments and FIB processing

For normal SEM observation, the samples were coated with platinum-palladium (Pt-Pd) of 5 nm thick using a Hitachi E-1030 sputtering coater. For SEM-EBSD

(Electron Back-Scatter Diffraction) mapping, the samples were coated with amorphous carbon of about 4 to 5 nm thick by vacuum evaporation (SC-701C; Sanyu Denshi). For TEM observation, thin film specimens were prepared using a focused ion beam (FIB) instrument (FB-2100; Hitachi). The samples for FIB were coated previously with Pt-Pd (5 nm) and amorphous carbon (about 15 nm) successively. After the coating, samples were processed using a gallium ion beam. The accelerate voltage was 30 kV for initial trimming, digging and thinning, and 10 kV for the final thinning process to remove the damage layer. The samples were covered with tungsten deposit to prevent the sample surface from the beam damage. The details of the FIB technique can be found in Kudo *et al.* (2010).

6. SEM and TEM

All SEM observations and SEM-Energy Dispersive X-ray spectrometry (EDS) analyses were performed using Hitachi S-4500. JEOL JEM 5600 LV was used for SEM-EBSD mapping. The samples were observed via secondary electron imaging with an accelerate voltage of 2 kV, 5 kV, or 15 kV. For more detailed observation and to investigate the crystallographic aspects, TEM (JEM-2010; JEOL) was used. The accelerating voltage was 200 kV. To analyze chemical compositions in the cuticles, TEM-Energy Dispersive X-ray spectroscopy (EDS, JED-2200; JEOL) was used. The intermolt cuticle was also analyzed using Scanning Transmission Electron Microscopy (STEM: JEM-2010F; JEOL) - Electron Energy-Loss Spectrometry (EELS) technique. The accelerating voltage was also 200 kV.

2-3. Results

2-3-1. Intermolt stage

1. XRD analyses

All sharp peaks in the diffraction patterns from both the powdered and non-destructive samples were attributed to calcite. Several broad peaks at the low-angle region were considered to be from chitin peaks (Sun *et al.*, 2006) (Fig. 2-1a). The peak positions of the calcite reflections were very close to theoretical ones for pure calcite, implying that the calcite in the cuticle of *A. vulgare* is not magnesian (Mg-) calcite, or that the amount of magnesium in calcite is very small. This result is not in agreement with the report by Becker *et al.* (2005). The intensity distribution of the peaks in the XRD pattern from the powdered sample is very similar to the theoretical one. For non-destructive sample, however, the pattern shows some weaker peaks than the theoretical ones, like 018 or $10\underline{10}$ (Fig. 2-1b). The angles of several reflections (reciprocal lattice vectors) from the ***c***-axis are shown in Table 2-1. The directions of the weaker peaks in the non-destructive sample are closer to the ***c***-axis than the other peaks. This result suggests that the ***c***-axes of calcite in the intermolt stage tend to orient parallel to the cuticle surface.

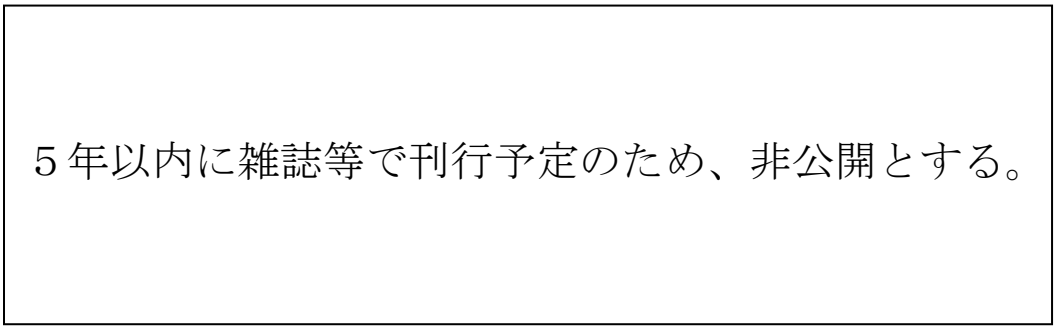

Fig. 2-1. Comparison of the XRD patterns from non-destructive and powdered samples, and the theoretical one. (a) XRD patterns from 5^{o} to 70^{o}. The green rectangle indicates the area shown in (b). (b) Magnified patterns from 45^{o} to 67^{o}. 018, 10$\underline{10}$, 119 and 00$\underline{12}$ peaks from the non-destructive sample are weaker those from the powder sample and theoretical ones.

Table 2-1. The calculated angles between the reciprocal lattice vectors and ***c***-axis for calcite.

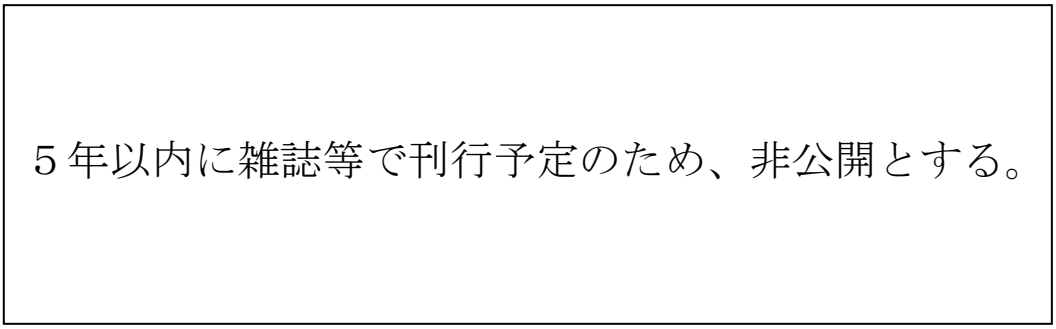

2. SEM-EBSD mapping

To investigate the crystal size and orientation of calcite on the surface of the cuticle or in the distal layer, SEM-EBSD mapping was conducted (Fig. 2-2). The cuticle was breached by undiluted solution of NaClO for one day to remove the epicuticle, and sticked on the resin stage. The crystal orientation could not be determined at many points, especially in upper area of the SEM image (Fig. 2-2a-c), probably due to the asperity and curvy surface. Nevertheless, the size of individual crystals can be roughly estimated to be about 20 × 20 μm to 50 × 100 μm, from the areas with the same crystal orientation. The NaClO-treated surface of the cuticle is devided about 20 × 20 μm areas by zigzagged lines (Fig. 2-2f). It is suggested that these lines observed by SEM are crystal boundaries. In Fig. 2-2e, distribution of the ***c***-axis appears to form an arch, suggesting that calcite plates in the distal layer have uni-axis preferred orientation with <*hk*0> which rise up by *ca.* 40˚ from the surface, with its projection on the surface parallel to the anterior direction.

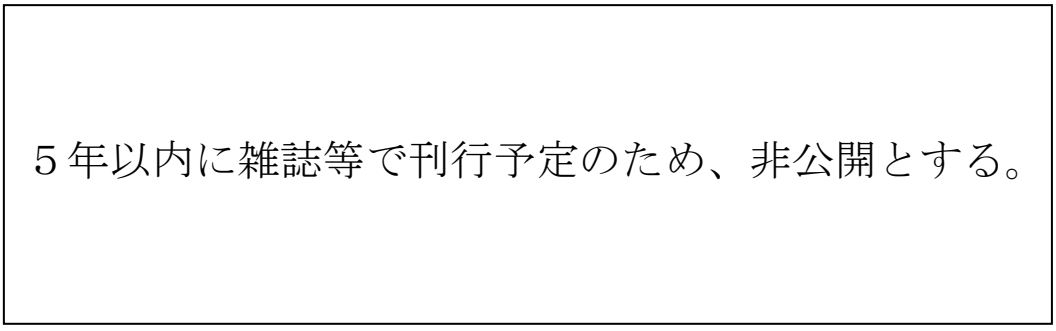

Fig. 2-2. SEM-EBSD mapping of the distal layer. (a) Mapping image, showing the crystal orientations parallel to the X0 direction in (e). (b) Mapping image, showing the crystal orientations parallel to the Y0 direction in (e). (c) Mapping image, showing the crystal orientations parallel to the Z0 direction in (e). (d) Color legend for the mapping image in (a) to (c). (e) The ***c***-axes orientations in the stereographic projection. (f) SEM image of NaClO-treated surface.

3. SEM/TEM observations

To observe the cuticle structure, its polished cross-section was observed by SEM (Fig. 2-3). As mentioned above, the cuticle can be divided into four layers; epicuticle (the outermost organic sheet), exocuticle, endocuticle, and membranous layer. Furthermore, the exocuticle is divided into the distal layer and transition zone (Fig. 2-3a, b). Transition zone and endocuticle (Fig. 2-3c) contain some fibrous structures. In this thesis, the transition zone is divided into upper transition zone and lower transition zone from the result of TEM observation as described below, and the schematic image is shown in Fig. 2-3d.

A cross-sectional TEM sample (from distal layer to endocuticle: about 10 μm depth from epicuticle to endocuticle) was prepared by the FIB technique (Figs. 2-4a and 2-5a). The distal layer consists of platy calcite crystals with 500 nm in thickness (Fig. 2-4b). Fresnel contrast which is likely to be organic matter in biominerals (Gries *et al.*, 2009; Okumura *et al.*, 2010) is rarely observed in this layer, especially in the lower half of the layer. In upper transition zone, Fresnel contrast is observed like a fibrous texture (Fig. 2-4b). Although the texture is largely different between these two layers, the crystal orientation is identical (Fig. 2-4c, d, e). The organic fibers are dense and fine in the lower transition zone than the upper transition zone. In the lower transition zone, the crystal orientation is different, and the crystals are far smaller than those of the distal layer and upper transition zone (Fig. 2-5b). Around the boundary between lower transition zone and endocuticle, both crystals and ACC exist (Fig. 2-5c, g, h). Endocuticle is filled with ACC and dense organic fibers (Fig. 2-5d, i). All fibrous Fresnel contrasts in upper/lower transition zone and endocuticle are well explained with the twisted plywood structure, partly showing the fibers parallel to the electron beam,

and the other showing the fibers perpendicular to the beam.

Next, a thin-film TEM specimen of the lower transition zone (about 7 μm depth from the outer surface), with the film parallel to the cuticle, was prepared from the cross-sectional polished sample to find the relationship between the crystal orientation of calcite crystals and that of organic fibers (Fig. 2-6). A low-magnified image shows that the fibers form an arch structure (Fig. 2-6a). This is probably corresponding to the structure of chitin-protein observed by SEM in Raabe *et al.* (2006). Many fibrous organic matrices are observed in the magnified images (Fig. 2-6b, c). From the SAED patterns from the areas with various fiber orientations, it was found that the ***c***-axes are oriented parallel to the fibers. As observed in the bright-field images (*e.g.* Fig. 2-6d), the crystal size of calcite in this zone is very small (10 to 20 nm). Occasionally larger crystals which show single-crystalline SAED pattern are observed (Fig. 2-6h, i). But their ***c***-axis is aligned along the same direction as surroundings.

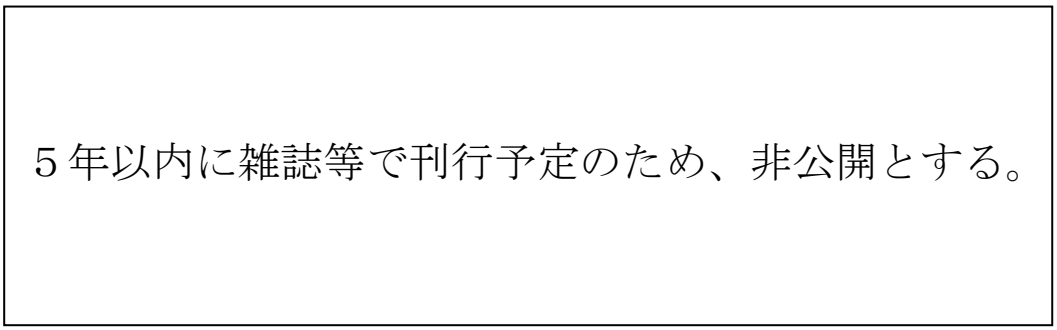

Fig. 2-3. SEM observation of intermolt cuticle. (a) Low-magnified image. (b) Magnified image of the surface region. (c) Magnified image of endocuticle. (d) Schematic image of intermolt cuticle. The black line inside of the image indicates organic matters. Dl: distal layer, UTz: upper transition zone, LTz; lower transition zone, En: endocuticle, Ml: membranous layer.

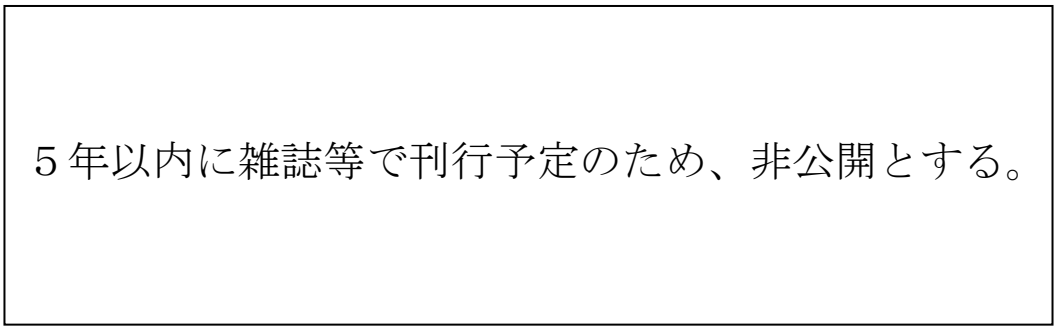

Fig. 2-4. Cross-sectional TEM images of intermolt cuticle. Dl: distal layer, UTz: upper transition zone, LTz: lower transition zone, En: endocuticle. (a) The whole picture of FIB sample. B is the area where the magnified image (b) was taken. (b) Magnified image of distal layer and transition zone (B in a). The Fresnel contrast is mainly shown in upper transition zone. (c) The image with high contrast. D in distal layer corresponds to the SAED pattern (d). E in upper transition zone corresponds to the SAED pattern (e). (d) SAED pattern of D in (c). (d) SAED pattern of E in (c). (f) Stereographic projection of (d, e) (northern hemisphere). A red point and arrowed line shows the *c*-direction.

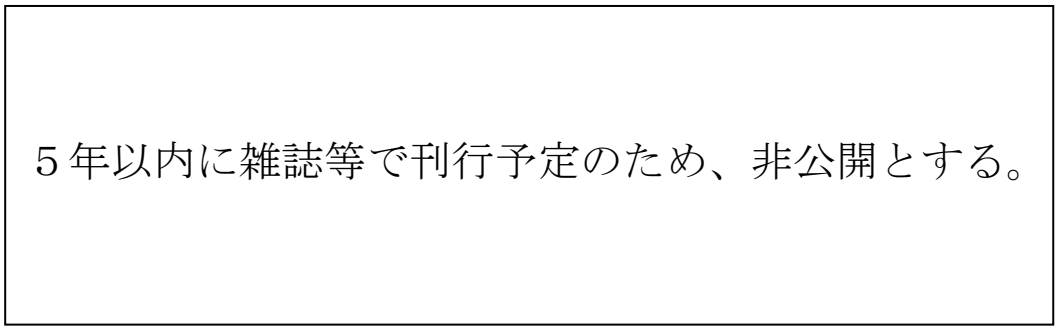

Fig. 2-5. Cross-sectional TEM images of intermolt cuticle. Dl: distal layer, UTz: upper transition zone, LTz: lower transition zone, En: endocuticle. (a) The whole picture of FIB sample (the same image as Fig. 2-4a). B to D are the areas where the magnified images (b) to (d) were taken. (b) Magnified image of lower transition zone (B in a). (c) Magnified image of the boundary between lower transition zone and endocuticle (C in a). (d) Magnified image of endocuticle (D in a). The SAED pattern (e) to (i) are correspond to E to I, shown in (b) to (d).

５年以内に雑誌等で刊行予定のため、非公開とする。

Fig. 2-6. TEM observation of lower-transition zone. (a) Appearance of the TEM sample. (b) Magnified image of B in (a). (c) SAED pattern of C in (b). (d) Magnified image of D in (a). (e) SAED pattern of E in (d). (f) Magnified image of F in (a). (g) SAED pattern of G in (f). (h) Magnified image of H in (a). (i) SAED pattern of I in (h).

4. STEM-EELS analyses

To confirm that the fibrous Fresnel contrast observed in TEM (Figs. 2-4, 2-5) is organic matter, and that the amorphous material observed in TEM (Fig. 2-5) is ACC, the FIB sample was analyzed by STEM-EELS. Mansot *et al.* (2003) and Okumura *et al.* (2010) suggested that EELS spectra from calcium carbonates containing organic matter contain peaks at 284, 289, 299, 347 and 350 eV as core-loss peaks. Among them, the peak from organic matter, graphite, and amorphous carbon appears only around 284 eV, whereas the sharp peak at 289 eV is characteristic for carbonate ions. The peak around 299 eV has a broad appearance and also from carbonate ions. The peaks at 347 and 350 eV are from calcium. The EELS spectrum from the distal layer without the Fresnel contrast (Fig. 2-7c) shows four peaks around 290.4 eV, 301.2 eV, 349.2 eV, and 352.8 eV. Though the absolute energy positions are slightly shifted (which is often the case for EELS), the former two peaks are attributed to carbonate ion and the latter two to calcium. On the other hand, the area with the Fresnel contrast near the surface of the distal layer (Fig. 2-7a, notice that the image is Z-contrast by HAADF-STEM imaging and organic matter in calcite is imaged as dark contrast) generates a peak around 285 eV (Fig. 2-7b) in addition to the four peaks shown in Fig. 2-7c, indicating that the dark contrast corresponds to organic matter, probably epicuticle. Simiarly, the other layers were analyzed by STEM-EELS. Although the intensity was weak, the peak around 285 eV was detected from fibrous dark contrasts in HAADF-STEM images (Figs. 2-8 to 2-9), which correspond to fibrous bright Fresnel contrast in Figs. 2-4 to 6, indicating that the all fibrous contrasts correspond to organic matrices. Although the endocuticle does not show crystalline SAED pattern (Fig. 2-5i), Ca $L_{2,3}$ peaks and those for carbonate ions were intensely detected (Fig. 2-10b), suggesting that the endocuticle

consists of ACC.

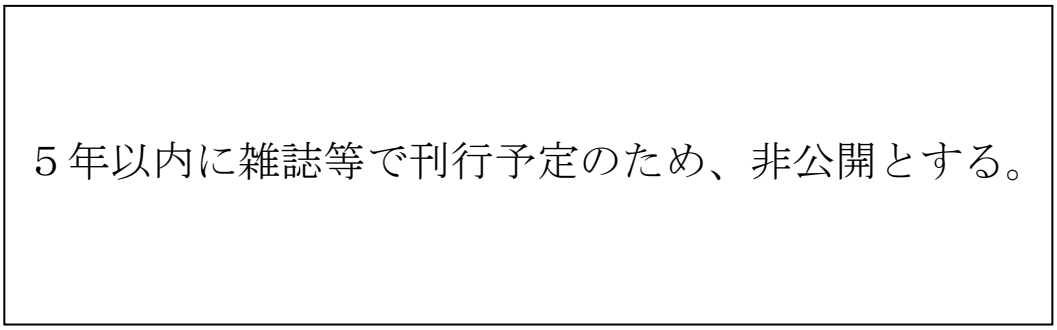

Fig. 2-7. EELS analyses of distal layer. (a) HAADF-STEM image of distal layer. (b) EELS spectrum from the area B in (a). (c) EELS spectrum from the area C in (a). 1: Ca L_3, 2: Ca L_2, 3: C-O (1σ→σ*), 4: C=O (1σ→π*), 5: C=C (1σ→π*)

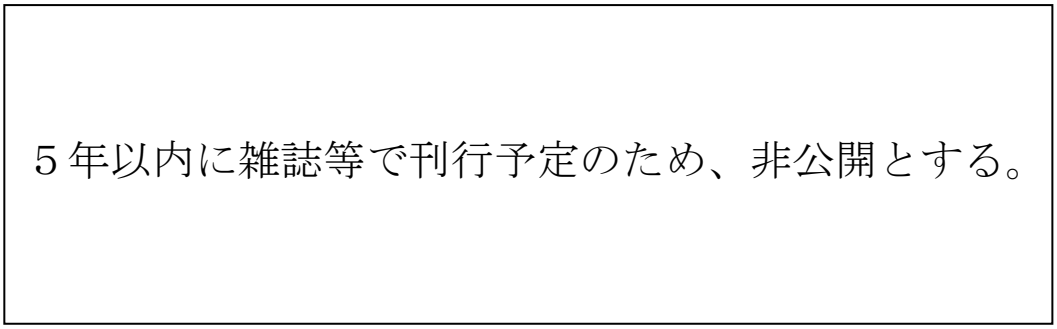

Fig. 2-8. EELS analyses of upper transition zone. (a) HAADF-STEM image of upper transition zone (parallel fibers). (b) EELS spectrum from the area B in (a). (c) HAADF-STEM image of upper transition zone (normal fibers). (d) EELS spectrum from the area D in (c).

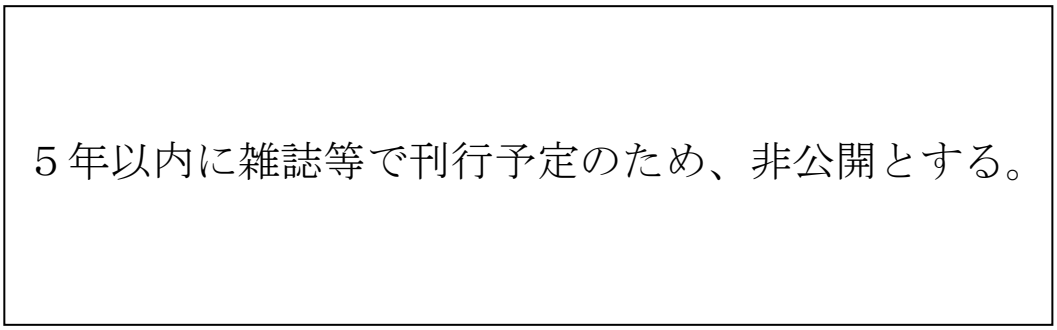

Fig. 2-9. EELS analyses of lower transition zone. (a) HAADF-STEM image of lower transition zone (parallel fibers). (b) EELS spectrum from the area B in (a). (c) HAADF-STEM image of lower transition zone (normal fibers). (d) EELS spectrum from the area D in (c).

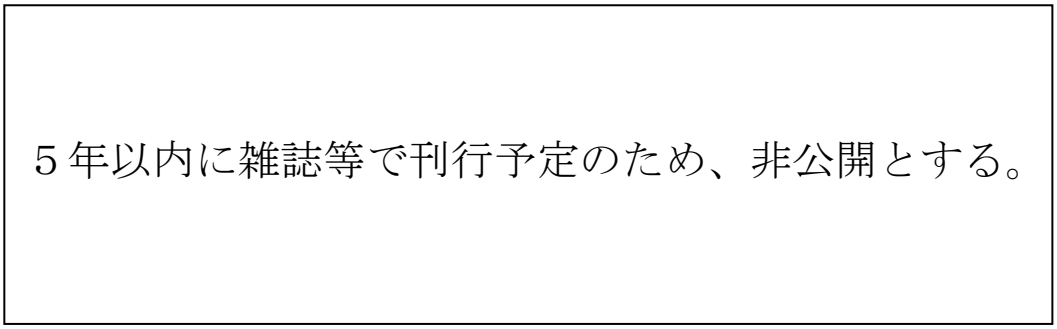

Fig. 2-10. EELS analyses of endocuticle. (a) TEM image of endocuticle. (b) EELS spectrum from the area B in (a).

5. SEM-EDS and TEM-EDS analyses

SEM-EDS and TEM-EDS standardless quantitative analyses were applied to the intermolt cuticle (Figs. 2-11, 2-12). Both P/Ca and Mg/Ca ratio tend to increase from the outer to the inner layer. Phosphorus exists much higher than magnesium in the entire cuticle. All layers were analyzed for three times in SEM-EDS, and averaged data are shown in Table 2-2. Table 2-3 shows the results which are calculated from TEM-EDS.

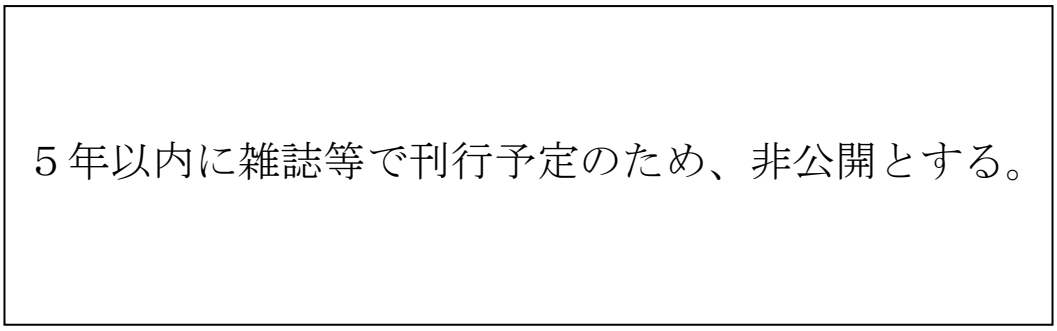

Fig. 2-11. The results of SEM-EDS analyses. (a) SEM image (the same image as in Fig. 2-3). (b-e) SEM-EDS spectrum. (b) to (e) correspond to B to E in (a) respectively. B in (a) indicates distal and upper transition zone. C in (a) indicates the lower transition zone. D and E in (a) indicates the upper and lower endocuticle.

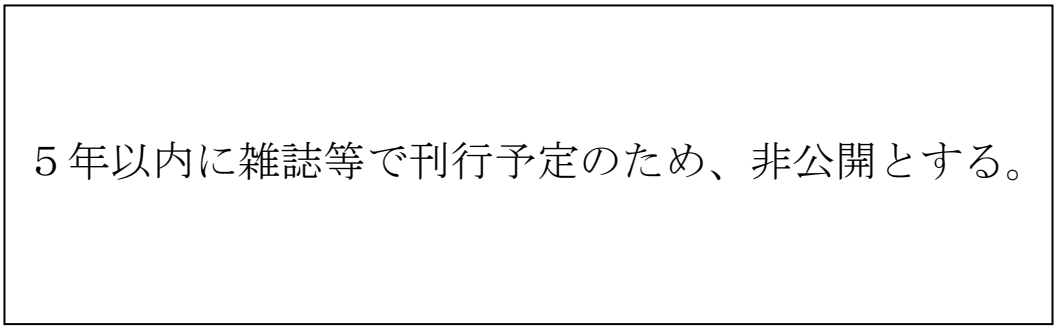

Fig. 2-12. The results of TEM-EDS analyses. Cu and Ga are contamination by FIB sample preparation system.

Table 2-2. P/Ca and Mg/Ca ratio (at%) in intermolt cuticle from SEM-EDS spectrum. upper transition zone; B in Fig. 2-11, lower transition zone; C in Fig. 2-11, upper endocuticle; D in Fig. 2-11, lower endocuticle; E in Fig. 2-11.

５年以内に雑誌等で刊行予定のため、非公開とする。

Table 2-3. P/Ca and Mg/Ca ratio (at%) in intermolt cuticle from TEM-EDS spectrum. All of the results are calculated from Fig. 2-12.

５年以内に雑誌等で刊行予定のため、非公開とする。

2-3-2. Cuticle in the intramolt stage

The microstructure of the new posterior cuticle in the intramolt stage was investigated using TEM and EDS. A platy region of *ca.* 300 nm in thickness is observed in the outermost, and spherular materials with hundreds nm in diameter are observed in the void under the platy region (Fig. 2-13a, b). No diffraction spots are found in the SAED pattern from these areas, indicating that the material is not crystallized (Fig. 2-13c, d). TEM-EDS analyses show that calcium is abundant in the platy region and spherules (Fig. 2-13b, c). Hence, they are considered ACC. The area under the spherules contains no calcium, indicating organic matters (Fig. 2-13g, h).

In other samples, fibrous structures are observed under the amorphous platy region (Fig. 2-14b). SAED patterns also do not show any diffraction spots (Fig. 2-14c, d, f). Although calcium is detected from all analyzed layers, the outermost platy region contains significantly-high concentration of calcium (Fig. 2-15c, d, e, f). Considering the location and thickness of the platy region, this region is considered to be the pre-stage of the distal layer, which consists of monolithic calcite plates in the intermolt stage. Hence, the present result suggests that the distal layer is also ACC originally and crystallized to calcite after molting.

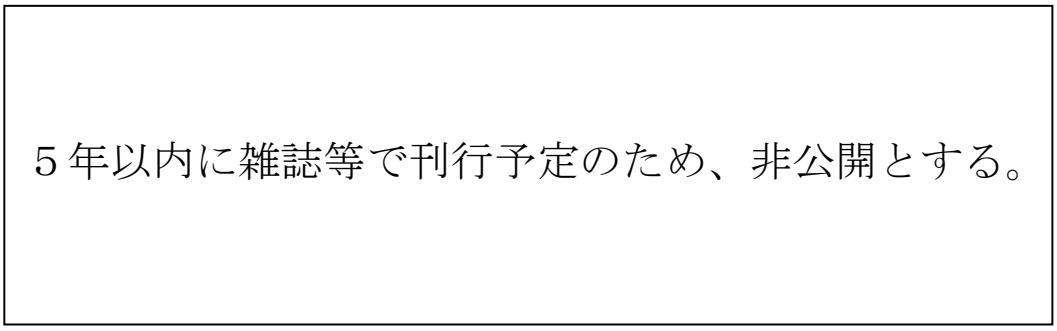

Fig. 2-13. TEM observation of the cross-section of the new cuticle in the intramolt stage. (a) Low-magnified TEM image. Black arrows indicate spherular materials. (b) Magnified image of B in (a). (c) SAED pattern from C in (b). (d) TEM-EDS spectrum from C in (b). (e) SAED pattern from E in (b). (f) TEM-EDS spectrum from E in (b). (g) SAED pattern from G in (b). (h) TEM-EDS spectrum from G in (b). W and Cu are contamination from tungsten coating and sample stage, respectively.

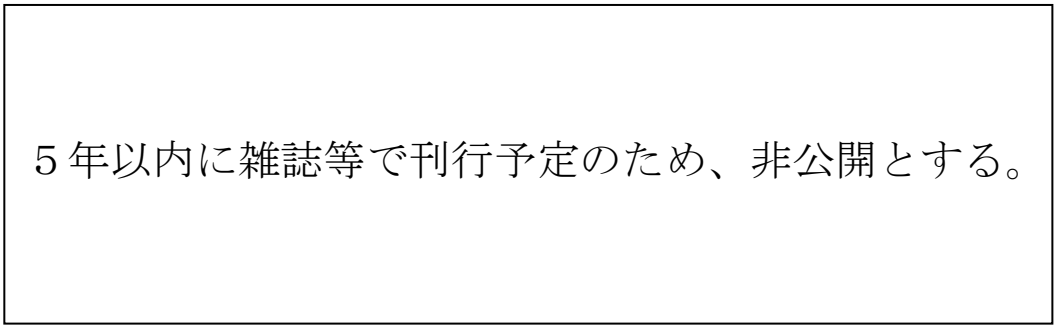

Fig. 2-14. TEM images from another cuticle specimen in the intramolt stage. (a) Low-magnified TEM image. (b) Magnified image of B in (a). (c) SAED pattern from C in (b). (d) SAED pattern from D in (b). (e) Magnified image of E in (a). (f) SAED pattern from F in (e).

５年以内に雑誌等で刊行予定のため、非公開とする。

Fig. 2-15. TEM-EDS spectrum from the specimen in Fig. 2-14. (a) Magnified TEM image of B in Fig. 2-14 (a). (b) Magnified TEM image of E in Fig. 2-14 (a). (c) TEM-EDS spectrum from C in (a). (d) TEM-EDS spectrum from D in (a). (e) TEM-EDS spectrum from E in (a). (f) TEM-EDS spectrum from F in (b). W and Cu is contamination from tungsten coating and sample stage, respectively.

2-4. Discussion

The present study is the first full-scale investigation of the biomineralization in terrestrial isopod using TEM and related techniques. Accordingly, a number of new results have been obtained with respect to the microstructures of the calcified cuticles and insights for their formation mechanism, which can never be approached using other analytical methods such as XRD, SEM and Raman spectroscopy. The main results and possible formation pathway for each layer are described in the following.

Distal layer

This layer is the outmost calcite layer about 500 nm thick. This thickness is well regulated from SEM and TEM observation, implying that the crystal was formed in a confined space preformed by the organism. Hild *et al.* (2008) reported that the layer consists of small calcite particles from SEM images but this is not correct. My EBSD and TEM analyses indicated that the calcite crystals are mono-crystalline with a platy morphology of several tens micrometers laterally. Probably Hild *et al.* (2008) considered only the surface asperity observed by SEM. It is rather surprising that the crystal has a very high aspect ratio (~100) between the lateral width and thickness. Another interesting feature is the distinct preferred orientation of these calcite plates, as determined by EBSD. The directions of the ***c***-axes are distributed along a great circle in the stereo map, indicating a uni-axial preferred orientation with some <*hk*0> direction as the preferred axis. Furthermore, this preferred axis rises up by *ca.* 40˚ from the surface. For instance, the ***c***-axis is the preferred axis commonly for calcite and it is normal to the shell surface in molluscan shells. In case of aragonite in the shells, its ***c***-axis is also typical as the preferred axis. The ***c***-axes of both calcite and aragonite are perpendicular to the triangles of CO_3^{2-} ion in their crystal structures and the growth rate along the

c-axis is generally the fastest for calcite and aragonite. In this regard, the crystal orientation of calcite in the distal layer of *A. vulgare* is very unique. Recently Seidl *et al.* (2012) investigated the crystal orientation in the distal layer of *A. valgare* also using SEM-EBSD and obtained almost the same result as mine. It is interesting that they also analyzed *P. Scaber* and found that the crystal orientation of calcite in the distal layer of *P. Scaber* is completely different; the ***c***-axis is normal to the cuticle surface just like the prismatic layer of bivalves. Hence, the formation scheme of calcite in the distal layer may be different between the two genera.

The result of Raman spectroscopy by Neues *et al.* (2011) suggested that the distal layer is already crystalline after one hour from the molt, when the transition zone beneath the distal layer has not been crystallized yet. This result may suggest that calcite in the distal layer formed directly from solution. However, my TEM observation of the new cuticle at the middle stage of the intra-molt period indicated that this layer is also ACC originally (Fig. 2-13). If this is true, the calcite crystals in the distal layer acquired their platy morphology with a high aspect ratio and distinct crystal orientation during the transformation of ACC. It is evident that in order to obtain such a high aspect ratio, the density and location of the nuclei of calcite must be strictly controlled. Furthermore, probably some template material is necessary to realize the distinct crystal orientation. Of course it is impossible at present to explain the origin of these distinct features and more detailed, time-resolved analyses is expected as future works.

Transition zone

The result by Neues *et al.* (2011) indicated undoubtedly that ACC initially deposited here transformed to calcite after molting in organism. The driving force for the transition is probably desiccation of the new cuticles (dehydration of ACC) after

exposure to the environment, as ACC becomes unstable and transforms to calcite by dehydration. TEM analysis in this study revealed two different crystallization mechanisms; “epitaxial crystallization” using platy calcite in the distal layer as the “substrate” in the upper transition zone, and “organic matrices mediated crystallization” around the lower transition zone. Evidently in the former crystallization the crystal orientation of transformed calcite completely inherits that of platy calcite in the distal layer (Fig. 2-4). Moreover, the spot shape in the diffraction pattern is sufficiently sharp (Fig. 2-4e), indicating mono-crystalline feature of the calcite crystal. It is suspected that such high crystallinity or epitaxial growth can be attained by dissolution of ACC and precipitation of calcite via interstitial body fluid. On the other hand, the crystal size of most calcite in the lower transition zone is extremely small (~ 10 nm) and their ***c***-axis is oriented parallel to the chitin-protein fibers. Hence these fibers must induce the crystallization of attached ACC, probably by some template effect. Because the amount of chitin-protein fibers is considerably high in the lower transition zone, the nucleation sites at the interface between the fibers and ACC are dense, which results in the aggregates of minute calcite crystals. However, as the fibers are aligned parallel to the cuticle, a preferred crystal orientation that the ***c***-axis tends to be parallel to the cuticle is attained, as indicated by XRD and electron diffraction analysis.

Inhibitor of crystallization

TEM and STEM-EELS analyses indicated that the endocuticle consists of mainly ACC and organic matrices at any molting stages. This result is consistent with that obtained from Raman spectroscopy (Hild *et al.*, 2008; Neues *et al.*, 2011). Compared to the transition zone, the endocuticle may not be desiccated owing to the depth from the surface or richer body fluid. Beside this speculation, the amount of some substance

which acts as the inhibitor of crystallization may be different between the transition zone and endocuticle. TEM-EDS analyses indicate considerable amount of phosphorus and small amount of magnesium in the transition zone and endocuticle, and they are definitely more in the endocuticle than transition zone. The content of magnesium is about 3.0 to 4.5 at% in endocuticle. Tao *et al.* (2009) suggested that more than 8.3 ± 0.5 at% of magnesium is necessary to be effective for the stabilization of ACC without aspartic acid (Asp). In case of the coexistence of Asp, more magnesium ions are necessary to stabilize ACC. Hence, this magnesium concentration is not enough to work as the stabilizer of ACC or inhibitor of crystallization. On the contrary, a number of previous works reported that phosphate ions or phosphor compounds work for ACC stabilization. Sato *et al.* (2011) reported that phosphoenolpyruvate ($C_3H_5O_6P$; PEP) and 3-phosphoglycerate ($C_3H_7O_7P$; 3PG) which are glycolytic intermediates work as ACC stabilizer as well as phosphoric acid in the gastrolith of a freshwater crayfish, *Procambarus clarkii*. In the present study, I have only analyzed the content of phosphorus and its chemical or molecular species has not been determined. However, such phosphrous compounds may be common in crustacean including crayfish, blue crab and isopods, in which ACC have been commonly reported. Sato *et al.* (2011) showed that P/Ca atomic ratio in the cuticle of *P. clarkii* is about 0.041. The P/Ca ratio in the endocuticle of *A. vulgare* is 0.112 to 0.132, considerably higher than that in the gastrolith of *P. clarkii*. Thus, it is expected that phosphorus compounds stabilizes ACC sufficiently in the endocuticle.

Finally, the schematic model for calcification of the cuticle in *A. vulgare*, derived from the results of the present study and previous works is illustrated in Fig. 2-16, although some speculations are included in the model. First, epicuticle is formed

between the endocuticle and membranous layer (Fig. 2-16a, Nagasawa, 2011). Second, ACC precipitates beneath the epicuticle from the supersaturated body fluid secreted by the soft body (Fig. 2-16b). ACC in the region of 0.5 μm thick beneath the epicuticle is crystallized into calcite, to form the distal layer (Fig. 2-16c). After that, the crystallization from the surface starts epitaxially with the distal layer as “substrate”, in the upper transition zone, as well as the crystallization of ACC along the organic fibers in the lower transition area (Fig. 2-16d). Finally, both crystallizations are completed in the transition zone (Fig. 2-16e). Crystallization of ACC does not occur or considerably delayed owing to a high concentration of the phosphorus inhibitor.

５年以内に雑誌等で刊行予定のため、非公開とする。

Fig. 2-16. Schematic model of calcification of the new cuticle of *A. vulgare*, proposed from the present study. (a) Pre-molt stage; only organic matrices exist. (b) ACC deposits under the epicuticle. (c) ACC deposits continuously and ACC at the distal layer is crystallized to form platy calcite crystals. (d) ACC in the transition zone starts crystallized, epitaxially from the surface side and along the organic fibers inside the zone. (e) Crystallization of ACC is completed in the transition zone. Figure legends; Ep: epicuticle, Dl: distal layer, UTz: upper transition zone, LTz: lower transition zone. En: endocuticle. Ml: Membranous layer.

2-5. Conclusions

In this chapter, microstructure in the cuticles of a terrestrial isopod *A. vulgare* was investigated to understand their biomineralization process. This is probably the first study to analyze calcite crystals transformed from ACC mainly using TEM, by which their mineralogical and crystallographic characteristics have been elucidated. My conclusion is that two crystallization processes, epitaxial crystallization with the pre-existing calcite plates and crystallization mediated by organic matrices (chin-protein fibers), occur in the transition zone of the cuticles. The crystal size and crystal orientation are completely different between the two processes. Especially very fine calcite crystals (~ 10 nm) with their ***c***-axis aligned parallel to the organic fibers are distinct, if compared to other calcite biominerals. This interesting feature (the small crystal size) may be attained through the crystallization with the existence of phosphorous compounds, which act as the ACC stabilizer. The distinct preferred crystal orientation of calcite in the distal (outermost) layer is also exciting finding in this study and recent report by Seidl *et al.* (2012). I found that the calcite in this layer is originally ACC from the observation in the new cuticles in the intramolt stage. However, the calcite in the layer has a monolithic crystalline feature and almost phosphorous free. Hence, the initial ACC may not have contained phosphorous compounds or the compounds were excluded during the crystallization.

In summary, the mineralogical character of calcite crystallized from ACC is not simple, and can possess various microstructures in biomineralization, depending on its crystallization processes.

Chapter 3

Structure analyses of molluscan larval shells

3-1. Introduction

3-1-1. Larval shells of mollusks

Molluscan shells are one of the most major biominerals with various, often well-regulated and elaborate microstructures. The shells consist of calcite and aragonite, and the formation of these microstructures is thought to be controlled by organic matrices, such as shell matrix proteins and chitin (*e.g.* Addadi and Weiner, 1997; Addadi *et al.*, 2006). The mechanisms to form these microstructures have been attracting researchers in various fields such as geology, biology, chemistry and material engineering. Especially, molecular biologists are interested in the shell matrix proteins. They identified various matrix proteins and discussed their functions (*e.g.* Marin and Luquet, 2004, Miyamoto *et al.*, 1996; Samata *et al.*, 1999, Suzuki *et al.*, 2007). On the other hand, shell microstructures have been investigated in detail from the mineralogical and crystallographic view points to understand the biogenic contributions to the structures (*e.g.* Kudo *et al.*, 2010; Jacob *et al.*, 2011). However, comprehensive elucidation of the recipes to fabricate shell microstructures such as nacreous, cross-lamellar and prismatic structures through organic-inorganic interactions has not been completed yet.

Although many studies for molluscan adult shells have been conducted as described above, limited studies have been reported about their larval shells. Compared to the adult shells with diverse microstructures depending on the classes or species of mollusks, it has been found that the structures of molluscan larval shells are not differentiated and resemble each other. Stenzel (1964) firstly measured XRD for two species, *Crassostrea virginica* and *Mercenaria mercenaria* and found that the larval shells are made of aragonite only, although the adult shells are made of aragonite and

calcite. Similar results have been reported for other larval molluscan shells, and the idea that the larval shells are made from only aragonite became accepted by most researchers (*e.g.* Taylor *et al.*, 1969; Kobayashi, 1980; Waller, 1981; Watabe, 1988; Castilho *et al.*, 1989). Not only the mineral components but also the development and shell structures were reported. Kniprath (1980, 1981) showed that an ectodermal cell called "shell field" forms the "shell gland" in the earliest stage of shell formation in *Ostrea edulis*. Waller (1981) observed the larvae of the European oyster, *O. edulis* using SEM and described the development of the larval shell as follows.

The shell formation starts from the middle to late trochophore stage (around 15 hours after fertilization). The first shell formed from the shell gland is called prodissoconch-I, and the larvae become the D-shaped stage which corresponds to the beginning to the middle of veliger stage (few days after fertilization). After forming prodissoconch-I shell, prodissoconch-II shell is formed during the middle to the end of veliger stage (about 2 weeks after fertilization). At this time, the umbonal area becomes more and more swollen, and called umbo stage. The larval shell consists of three layers in umbo stage. They are termed the outer prismatic layer, granular homogeneous layer, and the inner prismatic layer. The outer and inner prismatic layers show similar textures in SEM. The granular homogeneous later is also called the globular homogeneous layer by, for example, Weiss *et al.* (2002).

Mouěza *et al.* (2006) observed the embryo of a bivalve, *Chione cancellata* during fertilization and the first shell formation. The larval shell formation started from two shell fields, and the two lobes are formed at around 12 hours after fertilization in this species. Until 24 hours after fertilization, the larval shell has already covered the whole embryo. These developments of the shell were explained by a schematic model. At T_0

(fertilization) + 4 h, the shell field contains both shell and ligament secretory cells. The apical pole of the ligament-secretory cells (T2 cells) is covered by the periostracum-secretory cells (T1 cells). At T_0 + 6 h, the proliferation of the T1 cells is similar to the process described for epithelial stem cells. The new shell-secretory cells (T3 cells) do not elaborate periostracum material. Up to T_0 + 12 h, the expansion of the shell field is only due to the proliferation of the daughter T3 cells. Until T_0 + 12 h, the T2 cells reach the surface of the shell-field epithelium, set apart the T1 cells (B and C in Fig. 3-3), and create the two valves of the bivalve shell. The hinge field becomes obvious. At T_0 + 24 h, the T3 cells elaborate a secondary organic layer which encloses calcified crystals. T2 cells are now secreting the ligament material.

Fujimura *et al.* (1995) investigated the development of larvae of *P. fucuta* and suggested that it is almost the same as those of *C. cancellata* and *O. edulis*. Kobayashi (1980, 1981) analyzed the D-stage larvae (veliger stage) and juvenile shell (the shell after settlement) structures and the crystal polymorphs. He showed that the larval shell of D-stage consists of only aragonite using XRD, and the shell structures are far from that of the adult shell.

Mao Che *et al.* (2001) observed the shell development of *Pinctada margaritifera* in detail, and suggested that the prodissoconch-I consists of short parallel-organized prisms, and the prodissoconch-Ⅱ has long parallel prisms perpendicular to the shell surface. This report is the first that observed the shell at a fixed time interval. They also suggested that the shell consists of aragonite. Larval shells of freshwater bivalve, *Anodonta cygnea* was observed by SEM (Castilho *et al.*, 1989). In this study, only monolayered larval shell with a prismatic structure was observed (Castilho *et al.*, 1989). Although the structure is similar to that of *Ostrea edulis* reported by Waller (1981),

there are many pore canals in the shell.

On the contrary, a number of recent papers reported that ACC forms in larval shells of mollusks as a precursor phase of aragonite. Eggs of the freshwater snail, *Biomphalaria grabrata* were analyzed using XRD and FT-IR, and it was suggested that it consists of amorphous material (Hasse *et al.*, 2000). After that, *B. grabrata* was analyzed using elecrton spectroscopic imaging (ESI) and high-resolution synchrotron XRD, and it was suggested that embryos until 60 hours age and egg masses until 72 hours age are completely amorphous (Marxen *et al.*, 2003).

Weiss *et al.* (2002) analyzed *Mercenaria mercenaria* and *Crassostrea gigas* larval shells 3 to 13 days after fertilization, using the Raman spectroscopy, separating prodissoconch-I, transition layer, prodissoconch-Ⅱ, and the edge of the shell. If the peak height ratio of 205 cm^{-1}/1087 cm^{-1} is calculated, the ratios for the earlier samples tend to be lower than those for the later samples in *M. mercenaria*. As a result, the larval shells were suggested to contain ACC as a precursor phase of aragonite. The larval shell consists of three layers, and the central granular layer was suggested to be ACC, by SEM observation of the cross-section of the larval shell 3 days after fertilization.

Larval shells of the abalone, *Haliotis tuberculata*, were observed by SEM, and the shell constituent analyzed by FT-IR (Auzoux-Bordenave *et al.*, 2010). As a result, the larval shell consists of three layers similarly to seawater bivalves; the outer prismatic layer, granular layer, and inner prismatic layer. The outer prismatic layer and granular layer are well-defined in 2 months old juvenile shell, although those layers are not well-defined at 10 days old shell. The outer prismatic layer was suggested to be formed from ACC primarily as a precursor phase of aragonite. This suggestion is rather different from that by Weiss *et al.* (2002).

On the other hand, Kudo *et al.* (2010) analyzed the larval shell of the oyster, *Crassostrea nippona*, using mainly FIB-TEM. Probably this was the first to investigate larval shells using TEM, by preparing the cross-sectional thin specimen of the shell using a focused-ion-beam (FIB) instrument. They showed that the earliest stage of the shell is aragonite monolayer with a dense multiple {110} twins. The second layer which was formed beneath the first layer after 72 hrs from fertilization has a granular texture formed with aragonite. Thus, the amorphous precursor phase which was suggested to exist in larval shells has not been found by FIB-TEM observation, at least in this species. However, there is possibility that radiation damage of FIB technique (increase of temperature up to ~100 °C and ion implantation to the shell) induced the crystallization of ACC, or that the existence/nonexistence of ACC varies among species.

3-1-2. Purpose of this study

As mentioned above, it was suggested previously that the larval shells of mollusks are all made of aragonite, a crystalline phase of calcium carbonates, mainly from the results of X-ray diffraction (XRD). However, recent spectroscopic techniques such as micro-Raman or FT-IR spectroscopy were applied to the analysis of the larval shells, which resulted in a new suggestion that the larval shells partly contain ACC at least during a certain period, as a precursor of aragonite. Because XRD is not sensitive to the detection of ACC, it seems probable that the previous works using XRD did not notice the existence of ACC. However, ACC can be easily discriminated from crystalline phases by TEM, using electron diffraction (halo rings vs. sharp spots or Debye-Scherrer rings) or bright-field imaging (the contrast for crystals is orientation-dependent but that for ACC is monotonous and unchanged by specimen tilting). Hence, the result by Kudo

et al. (2010) seems in disagreement with the suggestion of ACC. One may insist that FIB sample preparation induced the crystallization of ACC as an artifact. However, 1) the same FIB process actually preserved ACC in the cuticles of the pill bug, as described in Chapter 2 in this thesis. Hikida (2002, Master thesis) also observed ACC in gastrolith of cray-fish "as it is" in TEM, in spite of the sample preparation by argon ion-milling. 2) If ACC was crystallized by the FIB process, why it was transformed to aragonite, not calcite? As described in Appendix, synthetic ACC always transforms to calcite by heating. Accordingly, the claim that the original ACC in larval shells transformed to aragonite during the FIB sample preparation seems not strong. Another idea to explain the disagreement is that the existence/nonexistence of ACC in larval shells actually depends on species.

Beside the argument for the possibility of ACC in the molluscan larval shells, investigation of the microstructure of the larval shells of various species and discussion for their similarities or diversities should be also important. As shown in Kudo *et al.* (2010), TEM analysis of the shells gives a plenty of information for their microsotructures which cannot be obtained by other analytical techniques. Hence, I have decided to observe molluscan larval shells of several species available, using the similar FIB-TEM method to Kudo *et al.* (2010). Through this descriptive study, I will also discuss the possibility of the existence of ACC in larval shells.

3-1-3. Molluscan species investigated

In this chapter, four species of mollusks whose larvae are available have been selected. There are two major differences among them; water and reproduction system. Some major aspects of each mollusk are described as follows.

Pinctada fucata

P. fucata is a species belonging to Pterioida, Pteriomorphia, Bivalvia. This seashell was formerly called '*Pinctada fucata*', but it is sometimes called '*Pinctada martensii*' in recent years (*e.g.*, Okutani, 2000). It lives in rock reef of the subtropical to temperate zone, from intertidal zone to 20 m depth. To fertilize, the eggs spawned in seawater are fertilized with released sperm *in vitro*. After fertilization, they have planktonic habitats at the larval stage, but after metamorphosis, they become sedentary. Adult *P. fucata* forms a shell with two layers (Wada 1956, 1957); the prismatic layer formed outside and the nacreous layer inside.

Nipponacmea fuscoviridis

N. fuscoviridis is one of the limpets. The limpets are thought to be one of the most primitive gastropods (Deguchi, 2007), belonging to Patellogastropoda, Eogastropoda, Gastropoda. Sasaki and Okutani (1993) investigated the differences of adult shell microstructures, and erected the genus *Nipponacmea* to include eight limpet species that were allocated to the genus *Notoacmea*. *N. fuscoviridis* lives at intertidal zone of the area from south of Hokkaido to Okinawa. To fertilize, the eggs spawned in seawater are fertilized with released sperm *in vitro*, as used for *P. fucata*. After fertilization, they have planktonic habitats at the larval stage, but after metamorphosis, they become infaunal habitats. The shell of limpets consists of 4 to 6 layers. *N. fuscoviridis* has 5 layers; M-1 (the innermost layer; radial crossed-lamellar structure), M (myostracum), M+1 (concentric crossed-lamellar structure), M+2 (prismatic structure with minor irregular spherulitic prismatic structure), M+3 (the outermost layer; irregular spherulitic prismatic structure type-A) (Sasaki and Fuchigami, 2005).

Biompharalia glabrata

B. blabrata is a freshwater snail, belonging to Orthogastropoda, Heterobranchia. Because it is a host of the blood fluke, *Schistosoma mansoni*, this species has been studied well with respect to the soft body and shell matrix proteins (*e.g.* Zhang and Coultas, 2011; Saur *et al.*, 2012). It lives mainly in Central and South American continents. The main fertilization is cross-fertilization, and they rarely self-fertilize. The embryos grow in gel-like egg cupsules until juvenile. The adult shell consists of two-layered crossed lamellar structure (Marxen and Becker, 1997).

Corbicula sandai

C. sandai is one of the endemic species living in Lake Biwa, belonging to Veneroida, Heterodonta, Bivalvia. It lives at a sandy bottom the lake of about 10 m depth. To fertilize, the eggs spawned into seawater are fertilized with released sperm *in vitro*, like *P. fucata*. They do not have planktonic habitats. The larvae are covered by egg membrane until D-shaped larvae, and they become infernal habitats just after hatching (Hayashi, 1972). Although the shell microstructure has not been observed for this species, that of a closely-related species has been often observed. The adult shell of *Corbicula fluminea* consists of not only aragonite (acicular aggregates with their elongation parallel to the growth direction, randomly oriented barrel-shaped aggregates) but also vaterite (lamellar, columner) (Frenzel and Harper, 2011). Taylor *et al.* (1973) and Kobayashi and Takayasu (1995) observed the other closely-related species and suggested that the whole shell is consisted of aragonite with two lamellar structures. These characteristics are compiled into Table 3-1.

Table 3-1. Information of the species used for this chapter.

Species	class	subclass	procreation	sea/fresh	dioicus/ambisexual
P. fucata	Bivalvia	Pteriomorphia	external	seawater	dioicus
N. fuscoviridis	Gastropoda	Eogastropoda	external	seawater	dioicus
C. sandai	Bivalvia	Heterodonta	external	freshwater	dioicus
B. glabrata	Gastropoda	Orthogastropoda	oviparity	freshwater	ambisexual

3-2. Methods

3-2-1. Sampling

Larvae of *Pinctada fucata* were artificially fertilized and collected at Mie Prefecture Fisheries Institute, Mie, Japan. Larvae which were artificially fertilized in Minami-cho, Kaifu-county, Tokushima prefecture, were also used for a part of the experiments. The Mie sample was artificially fertilized three times; the end of May, 2008, the beginning of June, 2009, and from April to May, 2012. The samples in 2008 were collected until 9 weeks after fertilization, and those in 2009 and 2012 were all collected until 48 hours after fertilization. The sample of Tokushima prefecture was collected in 2006. In the Mie 2008 sample, matured seashells fertilized and kept in the institute for three years after fertilization were used (five individuals for male and female each). The shells were opened and the testes and the ovaries were extracted. First, the ovaries were injured by a razor, wrapped in gauze and washed in six 2*l*-tanks, which were filled with sea water and 750 μ*l* of 0.75 mM ammonia. The reason to add ammonia is to give an impulse for activation to inactive eggs. The eggs were left for an hour to give enough impulse, and the sperm which is prepared by the same method in one 2*l*-tank was divided into six and added into the each egg tanks. In sample collected at the year 2008, the water in the egg tanks was filtered and the larvae were cultivated in three 25*l*-tanks. The water temperature was 25 °C. The samples were collected 0, 6, 12, 18, 24, 36, 48 hours after fertilization and 1 to 6 and 9 weeks after fertilization from these tanks. Hereafter, I call the samples, for example, 6 hours after fertilization just “6 hours sample” in this study. After 48 hours, the larvae of three tanks were put together into one tank. To prevent the seawater decay, the seawater was changed occasionally. In sample collected at the year 2009, the larvae were cultivated in thirty 2*l*-beakers after filtered. The water

temperatures were kept at 20 °C, 25 °C, 30 °C, for 10 beakers each. The seawater was changed 12 hours after fertilization, and the larvae were collected 48 hours after fertilization. In samples collected at the year 2012, the seawater was also changed at 12 hours, and the all larvae were collected at 48 hours. All samples were preserved 100 % EtOH or 4 % paraformaldehyde. These sampling methods followed Suzuki (2008; Doctor thesis) with minor changes.

N. fuscoviridis larvae used in this study were fertilized in similar methods with minor changes. With respect to *N. fuscoviridis*, the adult shells were sampled in Shimoda, Shizuoka prefecture, and fertilization was performed in the laboratory. The larvae were collected at 24 hours and 48 hours after fertilization. They were fixed by 4 % paraformaldehyde and displaced to 100 % EtOH afterward.

C. sandai larvae were collected at Shiga Prefectural Fisheries Experiment Station. The larvae already formed prodissoconch-I shell (about 24 to 48 hours).

B. glabrata samples which lived at the wall of water tank were collected. Because the eggs were collected from spontaneous oviposition, the exact time from fertilization is unclear, but it may be 3 to 4 days (juvenile shell) after egg-deposition. 100 % EtOH was used for sample fixation, and the juvenile samples were picked up from gel-like egg capsules.

3-2-2. Sample preparations

The polishing and broken-sectional sample preparation methods and freeze-drying method were almost the same as those used in Chapter 2.

3-2-3. Analysis instruments

SEM (S-4500) and TEM (JEM-2010) with FIB sample preparation system (FB-2100) were mainly used for the observation, as described in Chapter 2 (see 2-2-2, 5, 6). In

addition, to observe organic matrices in aragonite, scanning transmission electron microscopy (STEM; JEM-2010F, JEOL) – high angle annular dark field (HAADF) technique was used. The accelerate voltage was 200 kV.

3-3. Results

3-3-1. Larval shell structure of *Pinctada fucata*

1. Observation by polarized microscopy

0 to 36 hours samples were observed using polarized microscopy (Figs. 3-1, 3-2). 0 to 12 hours samples did not show birefringence (Fig. 3-1b, d, f). The birefringent layer first appeared in the 18 hours sample (Fig. 3-2b). The layer already covered all embryos. According to this result, the shell started to form between 12 hours to 18 hours after fertilization. This result is consistent with Fujimura *et al.* (1995).

The embryo has a nearly spherical shape at 0 hour sample and the cleavage has not started yet (Fig. 3-1a). The primary polar body was released in a part of the embryos. At 6 hours sample, the embryo became the morula (Fig. 3-1c). Although the embryos showed an almost spherical shape, a part of the embryo was invaginated and became a distorted sphere in a portion of the embryo. At 12 hours sample, shells were still not observed (Fig. 3-1e, f). In most part of the embryo, the body invaginated in a portion of the body. In the larval shell formation, the dorsal epithelium tissue is thought to become a region where the shell forms, called the shell field, by the epithelium tissue emboly (Kniprath, 1980). That is to say, the shell was thought to be formed from the emboly region that was observed in 6 hours and 12 hours samples.

The shell covered the whole embryo at 18 hours sample (Fig. 3-2a, b). Cross-shaped quenching was observed in the samples later than 18 hours (Fig. 3-2a to f). Thus, the ***c***-axis was thought to be normal to the shell surface. The size of the shells was 50 to 60 μm.

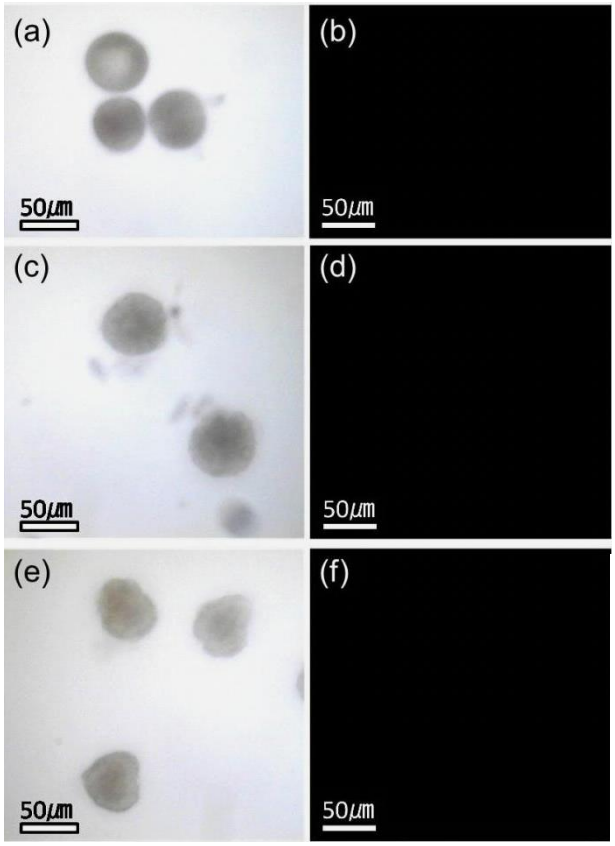

Fig. 3-1. Observation using polarized microscopy. (a, c, e) parallel-polar light, (b, d, f) cross-polar light. (a, b) 0 hour sample. (c, d) 6 hours sample. (e, f) 12 hours sample.

著作権が論文の発行元に帰属するため、非公開。

「Microstructures of the larval shell of a pearl oyster, *Pinctada fucata*, investigated by FIB-TEM technique」

American Mineralogist 誌　96 巻　1020～1027 頁　2011 年

Fig. 3-2. Observation using polarized microscopy. (a, c, e) parallel-polar light, (b, d, f) cross-polar light. (a, b) 18 hours after fertilization. (c, d) 24 hours after fertilization. (e, f) 36 hours after fertilization.

2. SEM and TEM observations of calcified larvae

18 hours sample

The D-stage larvae, or the first formed shell at 18 hours to 48 hours, were observed using SEM and TEM. For 18 hours sample, the larvae collected at Mie, 2008 were used. From SEM observation of the 18 hours sample, a thin shell which has no growth lines covers the whole embryo, and a rough region was observed around 10 to 20 μm from the center of the hinge (Fig. 3-3a). From the lack of the growth lines, all of the shell is considered prodissoconch-I. A radial pattern is observed from the umbo area, and this was also observed at 24 hours to 48 hours samples. These structures were reported in Waller (1981) and it is thought that the earliest shell was formed from this region. Observation from the dorsal side indicated that the curvature of the right and left valves are different from each other (Fig. 3-3b).

To observe the larval shell structure in detail, cross-sectional and plane-view TEM observations were conducuted. The same regions in prodissoconch-I shell after 18 and 48 hours were cut for the cross-sectional observation.

In the 18 hours shell, prismatic contrast was observed in the cross-sectional shell (Fig. 3-4b). The electron diffraction pattern (Fig. 3-4c) indicated that the mineral phase is aragonite and the ***c***-axis is normal to the shell surface. The thickness is about 0.3 μm. To obtain more detailed information, a plane-view sample was also fabricated (Fig. 3-4d). From the bright-field image (Fig. 3-4d) and the pseudo-hexagonal electron diffraction pattern (Fig. 3-4e) the prismatic contrast which was observed in the cross-sectional sample was proved to be related to dense multiple {110} twins. On the other hand, contrast indicating grain boundaries were rarely observed. Thus, the prismatic contrast shown in cross-sectional observation does not correspond to a “prismatic” structure. The

magnified plane-view image shows the boundaries of the twins (Fig. 3-4f). It is well known that aragonite crystals contain {110} twins frequently (Suzuki *et al.*, 2012).

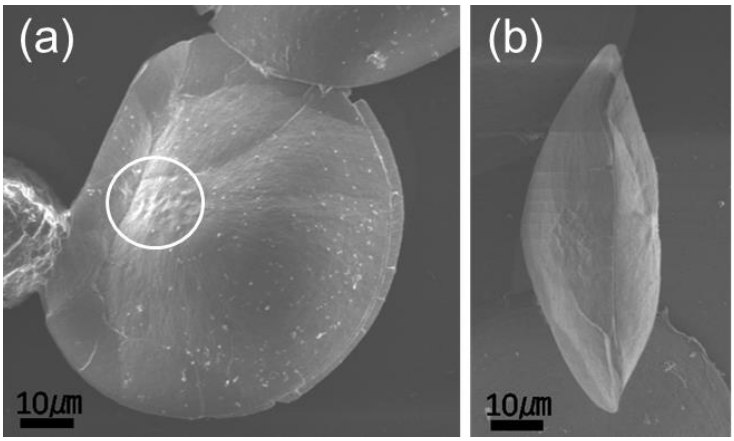

Fig. 3-3. SEM images of the 18 hours sample. (a) Lateral view of the sample. The white circle shows the rough surface. (b) The image of the dorsal side.

Fig. 3-4. TEM images of the 18 hour shell (Mie (2008) sample). (a) SEM image of the 18 hours shell. Rectangle is the region cut by FIB. (b) Cross-sectional TEM image of the rectangle region in (a). (c) Electron diffraction pattern from the circle in (b). (d) Plane-view image. (e) Electron diffraction pattern from (d). (f) Magnified plane-view image.

48 hours sample

From the cross-sectional observation, a new layer with globular structure has been formed under the outer prismatic layer observed in 18 hours sample (Fig. 3-5b). The thickness of the outer prismatic layer and the globular layer is about 0.5 μm, respectively. The globular layer is also made of aragonite, and its ***c***-axis is normal to the shell surface, as in the outer prismatic layer (Fig. 3-5c). The plane-view images and corresponding SAED patterns indicate two types of microstructures in the globular layer (Fig. 3-5d, e, f). One of them forms a pseudo-hexagonal diffraction pattern similar to the outer prismatic layer (Fig. 3-5e), and another forms concentric Debye-Scherrer rings, indicating the area containing dense {110} twins and that with a polycrystalline feature in which the ***a***- and ***b***-axis are randomly oriented, respectively.

On the other hand, it was found that the larval shell of 48 hours, sampled in Mie in 2008, formed calcite as the second layer, instead of aragonite (Fig. 3-5a, c). The outer layer is made of aragonite like the other sample, but its thickness is only 0.1 to 0.2 μm. As shown in the figure, the calcite crystals constituting the second layer are considerably large. Their ***c***-axis is normal to the shell surface. To investigate the origin of this polymorph switching, I collected samples again in 2009 at Mie Fisheries Institute. I suspected the water temperature as the origin and cultivated the larvae at three temperatures (20 °C, 25 °C and 30 °C) until 48 hours, because Su *et al.* (2004) reported using adult *Strombus gigas* that the shell contained a small amount of calcite at a low temperature. These temperatures were selected, considering the temperature for the samples collected in 2008. The samples were collected in the middle of June. The sampled larvae were analyzed by XRD. However, all three samples showed only aragonite, regardless of the water temperature (Fig. 3-7).

著作権が論文の発行元に帰属するため、非公開。

「Microstructures of the larval shell of a pearl oyster, *Pinctada fucata*, investigated by FIB-TEM technique」

American Mineralogist 誌　96 巻　1020～1027 頁　2011 年

Fig. 3-5. TEM analyses of 48 hours shell, sampled in Mie, 2009. (a) SEM image of 48 hours shell. Rectangle is the region cut by FIB. (b) Cross-sectional TEM image at the rectangle in (a). OPL: outer prismatic layer, GL: globular layer. (c) Electron diffraction pattern from the circle in (b). (d) Plane-view image. (e) Electron diffraction pattern from the black circle in (d). (f) Electron diffraction pattern from the white circle in (d).

著作権が論文の発行元に帰属するため、非公開。

「Microstructures of the larval shell of a pearl oyster, *Pinctada fucata*, investigated by FIB-TEM technique」

American Mineralogist 誌　96 巻　1020～1027 頁　2011 年

Fig. 3-6. (a) Cross-sectional TEM image of 48 hours shell, sampled in Mie, 2008. (b) Electron diffraction pattern from the outer prismatic layer (circle "B" in (a)). (c) Electron diffraction pattern from the circle "C" in (a). The diffraction pattern in (b) is explained with aragonite whereas that in (c) with calcite.

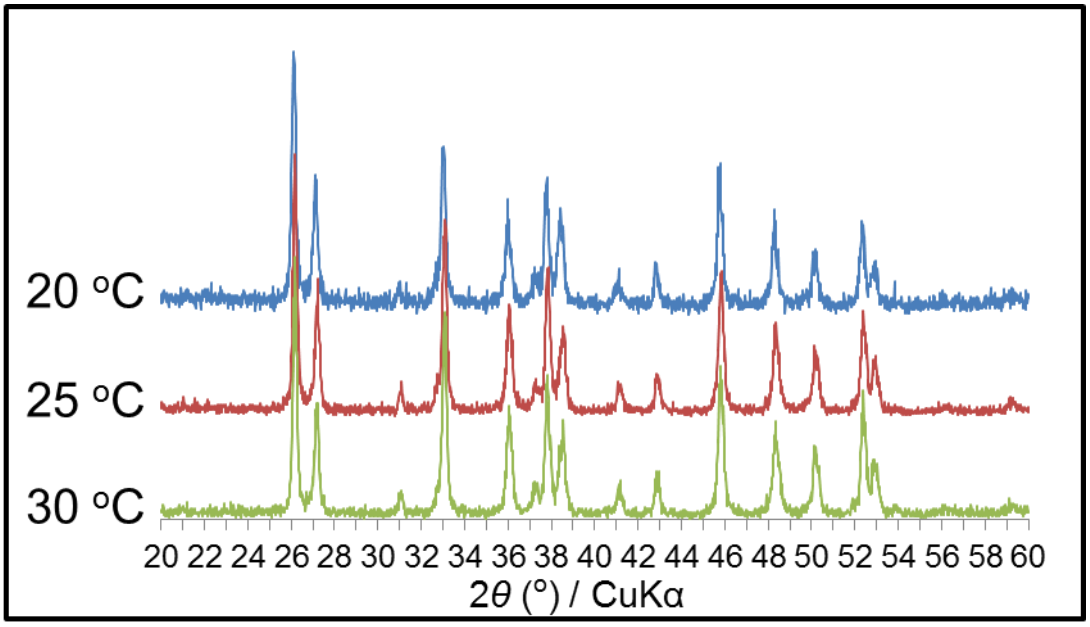

Fig. 3-7. Powder XRD patterns of 48 hours larvae, corrected in Mie, 2009. The larvae were cultivated at 20 °C, 25 °C and 30 °C. All peaks are assigned to aragonite.

3 weeks sample

The 3 weeks shell is in the stage just before settlement. The specimens for TEM analyses were cut from the umbonal (black rectangle in Fig. 3-8a) and the prodissoconch-II areas (white rectangle) using FIB.

In the umbonal area, the shell has been changed into three-layered structure (Fig. 3-8b, c). The outer and middle layers are the same ones as those observed in 48 hours sample, but the thickness of the middle globular layer has been increased to 2 to 3 μm. The inner layer, which was not observed in the younger samples, has a prism-like contrast and has a texture similar to the outer layer. The thickness is 1.5 to 2 μm. Electron diffraction patterns indicate that the constituting mineral is aragonite, with the ***c***-axis oriented normal to the shell surface (Fig. 3-8d).

Figs. 3-8e and f show the images for the prodissoconch-II area. In this area, the outer prismatic layer is not observed, and the globular layer is thicker than that in the umbonal area. This layer shows oblique diffraction contrast in the bright-field image (Fig. 3-8f).

Although the cross-sectional TEM contrast of the inner prismatic layer is similar to that of the outer prismatic layer, the plane-view TEM image of the inner prismatic layer (Fig. 3-8g) shows different characteristics. The image shows the cross-section of prisms of 100 - 300 nm in diameter, with sharply-defined grain boundaries. The {110} twins are observed inside the prisms. Thus, it is suggested that this layer which has prismatic contrast really consist of prisms tightly arranged normal to the shell surface.

著作権が論文の発行元に帰属するため、非公開。

「Microstructures of the larval shell of a pearl oyster, *Pinctada fucata*, investigated by FIB-TEM technique」

American Mineralogist 誌　96 巻　1020～1027 頁　2011 年

Fig. 3-8. (a) SEM image of the 3 week shell. Two-headed white arrow I indicates prodissoconch-I, and arrow II indicates prodissoconch-II. The area between prodissoconch-I and prodissoconch-II is the transition area. (b) SEM image of the fractured surface of prodissoconch-I. (c) Cross-sectional TEM image of prodissoconch-I. The TEM specimen was taken from the black rectangle in (a). OPL: outer prismatic layer; GL: granular homogeneous layer; IPL: inner prismatic layer. (d) SAED pattern from the circle in (c). (e) SEM image of the fractured surface of prodissoconch-II. (f) Cross-sectional TEM image of prodissoconch-II. The TEM specimen was taken from the white rectangle in (a). (g) Plane-view image of the inner prismatic layer in prodissoconch-I.

3. STEM-HAADF observations

The cross-sections of 48 hours prodissoconch-I shell and 3 weeks prodissoconch-II shell were also observed using STEM-HAADF to image organic matter inside the crystals and consider the contribution of the organic matter to the formation of the shell microstructures (Fig. 3-9). In outer prismatic layer, the dark spots which are considered to correspond to organic materials are very few (Fig. 3-9a). Only the vicinity of the outer surface (~100 nm) of the outer prismatic layer contains dark spots. The dark spots were densely observed in the globular layer (Fig. 3-9b). Finally the inner prismatic layer showed almost no dark spots (Fig. 3-9c).

Fig. 3-9. STEM-HAADF images of 48 hours shell (a) and 3weeks prodissoconch-II shell (b, c). OPL: outer prismatic layer, GL: globular homogeneous layer, IPL: inner prismatic layer.

3-3-2. Larval shell structures of the other species

1. *Nipponacmea fuscoviridis* (Seawater, Gastropoda)

24 hours and 48 hours larvae of *N. fuscoviridis* were observed in SEM (Figs. 3-10, 3-11). From the outer appearance, the shell surface has aconcentric texture (Fig. 3-10a). Observation of broken-section of 24 hours shell indicates a two-layered structure with the outer prismatic layer and inner layer. It also shows that the inner layer has elongated granules nearly parallel to the shell surface (Fig. 3-10c). 48 hours shell also shows the concentric texture on its surface (Fig. 3-11a). Observation at the broken-section indicates that the shell consists of three layers; the thin outer prismatic layer, middle platy layer with grains elongated nearly parallel to the shell surface, and thick inner prismatic layer (Fig. 3-11c).

Fig. 3-12 shows TEM images of 48 hours shell. The shell has at least two layers (Fig. 3-12a); the outer layer (Fig. 3-12d) and the granular layer (Fig. 3-12e, f). Both layers consist of aragonite with the ***c***-axis oriented normal to the shell surface (Fig. 3-12b, c). The shell structure is similar to that of the *P. fucata* 48hours larvae, but the appearance of the middle (granular) layer is considerably different between them. The granular layer of *N. fuscoviridis* is less dense than that of *P. fucata*. Interspace between aragonite grains is probably filled with organic matter, as suggested from TEM-EDS analysis (Fig. 3-13). Although the direction of the ***c***-axis in the middle granular layer is normal to the shell surface, the crystals looks elongated parallel to the shell surface as seen in SEM observation (Figs. 3-10, 3-11).

In another TEM specimen, the shell clearly consists of three layers (Fig. 3-14a). The voids filled with the organic matrices are less common than the shell in Fig. 3-12. Instead, many small organic matrices are observed in under-focused images (Fig. 3-14b).

At the boundary between globular and inner prismatic layers, platy crystals are found as the base of the inner prismatic layer (Fig. 3-14c). From SEM and other TEM observations, the aragonite crystals in the globular layer tend to elongate parallel to the shell surface. Thus, it is thought that the platy crystal is a part of globular layer. In the inner prismatic layer, prism-like contrast is observed. However, the prisms are not monolithic single crystals (Fig. 3-14d). In addition, one 48 hours shell completely consists of calcite (Fig. 3-15b). Calcite crystals are much larger than normal aragonite crystals. The ***c***-axis of calcite is normal to the shell surface (Fig. 3-15c). Similar phenomenon was observed in 48h *P. fucata* larvae (Fig. 3-6).

５年以内に雑誌等で刊行予定のため、非公開とする。

Fig. 3-10. SEM images of 24 hours *N. fuscoviridis* shell. (a) The outer appearance. (b) Broken-sectional observation. (c) Magnified image of C in (b).

５年以内に雑誌等で刊行予定のため、非公開とする。

Fig. 3-11. SEM images of 48hours larvae of *N. fuscoviridis*. (a) The outer appearance. (b) Broken-sectional observation. (c) Magnified image of C in (b). OPL: outer prismatic layer, GL: globular layer, IPL: inner prismatic layer.

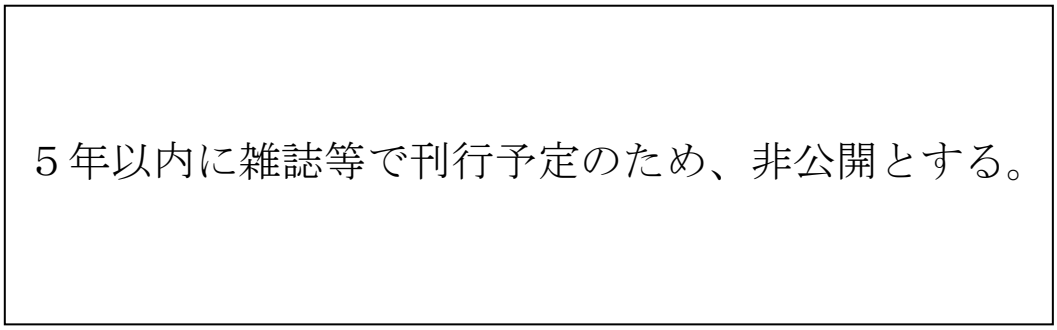

Fig. 3-12. TEM images of *N. fuscoviridis* 48 hours larvae. (a) Low-magnified image. (b) SAED pattern from B in (a) (left) and its zone axis map (left). (c) SAED pattern from C in (a) (left) and its zone axis map (right). (d) Magnified image of the outer layer. (e) Magnified image of the middle of the sample. (f) Magnified image of the inside of the sample.

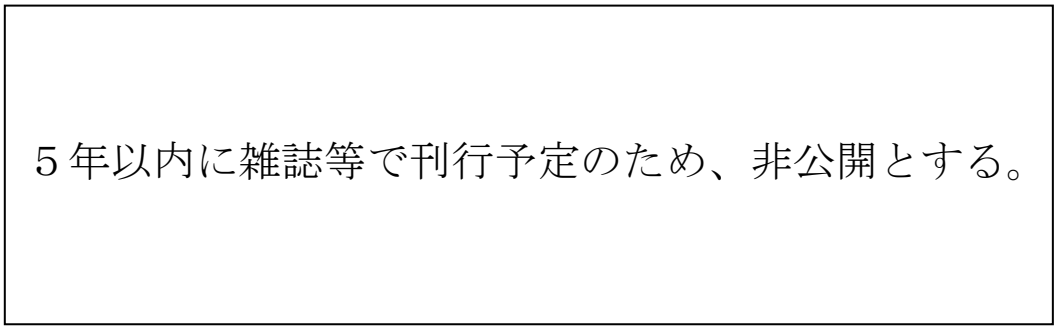

Fig. 3-13. Low-magnified TEM image and TEM-EDS spectra. (a) TEM image. (b) TEM-EDS spectrum from B in (a), the void between aragonite crystals. (c) TEM-EDS spectrum from C in (a), the aragonite crystal.

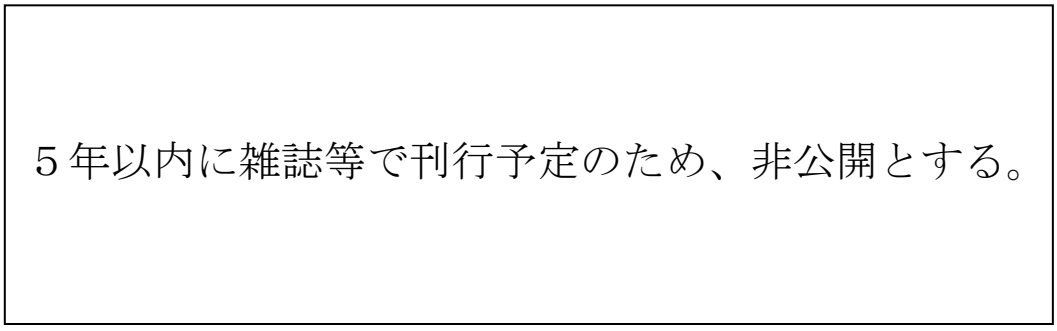

Fig. 3-14. TEM images of 48hours *N. fuscoviridis* shell. (a) Low-magnified image. OPL: outer prismatic layer, GL: globular layer, IPL: inner prismatic layer. (b) Defocused magnified image of globular layer. Many white spots are observed inside the crystals. (c) Magnified image between globular and inner prismatic layer. (d) Magnified image of the inner prismatic layer.

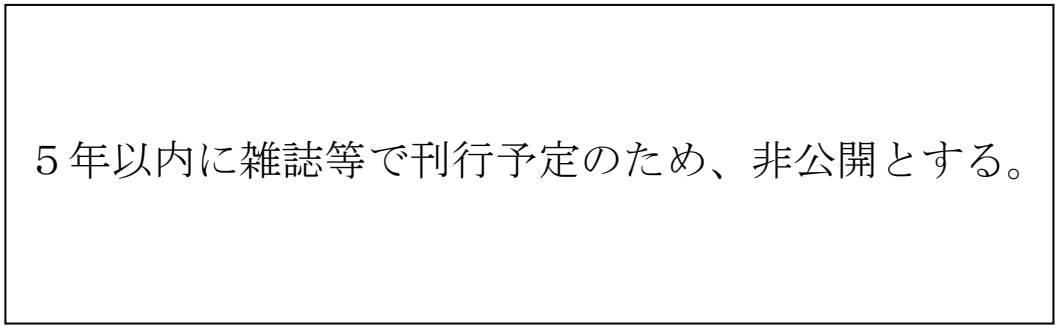

Fig. 3-15. TEM observation of another 48 hours shell of *N. fuscoviridis*. (a) Low-magnified image. OPL: outer prismatic layer, GL: globular layer. (b) Magnified image of globular layer. (c) SAED pattern (upper) and its zone axis map (lower). The ***c***-axis is oriented to the normal of the shell surface.

2. *Corbicula sandai* (Freshwater, Bivalvia)

With respect to *C. sandai*, I investigated the shell of D-shaped larvae (Fig. 3-16a). Although actual time from the fertilization is not clear, it seems 24 to 48 hours if compared with *P. fucuta*, because prodissoconch-I and transition area are observed. From observation of the broken-section, it looks that the shell consists of two layers, the outer prismatic layer and the globular layer (Fig. 3-16b). The density of the shell is similar to *P. fucuta*, higher than *N. fuscoviridis* (Figs. 3-10 – 3-14). TEM observation also indicates two layers with thin periostracum (Fig. 3-16c). The SAED patterns revealed that these layers are made of aragonite, and the ***c***-axis is normal to the shell. In addition, homogeneous area exists in a part of the outer surface. This area may correspond to the shell gland. The organic matrices mainly exist in the homogeneous area and the globular layer.

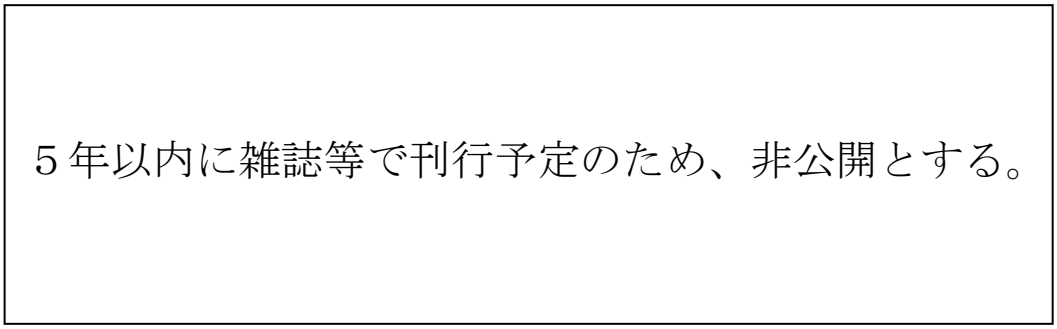

Fig. 3-16. SEM and TEM observations of *C. sandai* larvae. (a) The outer appearance. It seems to form prodissoconch-I and transition area. The short white line indicates the area where TEM sample was prepared. (b) Broken-sectional SEM image. OPL: outer prismatic layer, GL: globular layer. (c) Cross-sectional TEM image. P: periostracum. (d) SAED pattern of D in (c). (e) SAED pattern of E in (c). (f) Magnified image of the outer area. HA: homogeneous area.

3. *Biomphalaria glabrata* (Freshwater, Gastropoda)

The freshwater snail, *B. glabrata* was observed using SEM and TEM. The juvenile were freeze-dried before sample observation. In SEM observation, the shell shows three layered structure, outer prismatic layer, globular layer, and inner prismatic layer (Fig. 3-17c, d). Periostracum is thick, and the crystals forming globular layer elongate almost parallel to the shell surface, such as in the globular layer of *N. fuscoviridis*. The outer prismatic layer has smoother texture than the inner prismatic layer (Fig. 3-17c).

From TEM observation, periostracum and four shell layers were observed. In the outermost area, there is periostracum with the thickness of around 100 nm. The outer prismatic layer exits under the periostracum. In this layer, the contrast shows platy texture (Fig. 3-18c, e). The thickness of this layer is about 100 nm, much thinner than the other samples. The globular layer has a unique aspect. This layer shows rough crossed-lamellar contrast (Fig. 3-18e). The crystal density is less than the other layers, like *N. fuscoviridis*. The inner prismatic layer shows prism-like contrast, as shown in the other species. The crossed-lamellar layer is formed under the inner prismatic layer. It is thought that this crossed-lamellar layer is equivalent to adult shell. From the contrast, the axes direction of the crystals are continuing from the outer prismatic to the crossed-lamellar layer.

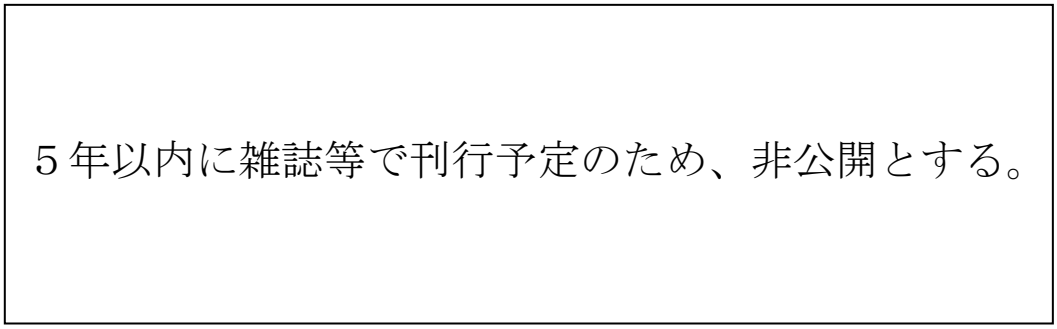

Fig. 3-17. SEM images of the juvenile shell of *B. glabrata*. (a) The outer appearance of the shell. (b) Broken sample. (c) Broken-sectional observation of C in (b). P: periostracum, OPL: outer prismatic layer, GL: globular layer, IPL: inner prismatic layer. (d) Magnified image.

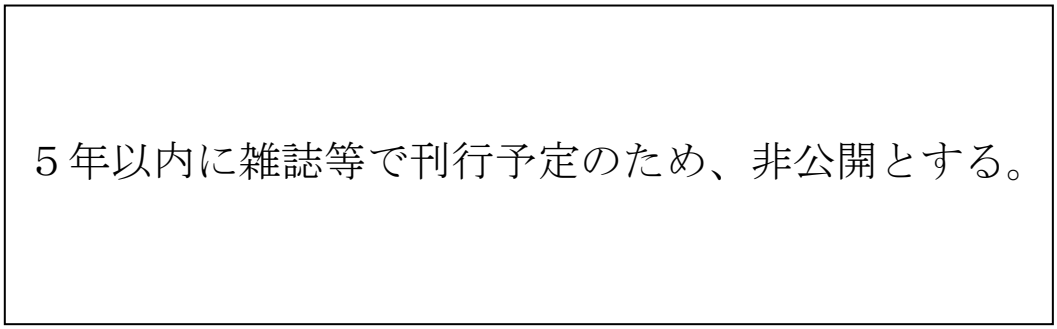

Fig. 3-18. TEM images of the juvenile shell of *B. glabrata*. (a) The outer appearance of the shell (the same image of Fig. 3-17b). Short white line indicates the place where the FIB sample prepared. (b) Low-magnified image. (c) Magnified image of the outer surface area. P: periostracum, OPL: outer prismatic layer, GL: globular layer. (d) SAED pattern from D in (c). (e) Magnified image. IPL: inner prismatic layer, CL: crossed-lamellar layer. (f) SAED pattern from F in (e).

3-4. Discussion

In this chapter, larval shell structures of several molluscan species were observed. In particular, the shell microstructure of *P. fucata* was investigated in detail. Accordingly, discussion from the results for *P. fucuta* is first described with the much debated issue of existence/nonexistence of ACC, and that for other species follows next.

1. Shell structure of *P. fucata*

Previously, the larval shells of bivalves were proposed to have three different textured layers (Carriker and Palmer, 1979; Waller, 1981; Weiss *et al.*, 2002). However, crystallography of each layer was not well investigated in these works. In this study, I have made detailed analyses with respect to the crystallographic aspect in the larval shell of *P. fucata* using the FIB-TEM technique. The first shell formed 18 hours after fertilization is an aragonite layer with the ***c***-axis perpendicular to the surface and dense polycyclic {110} twins, which is similar to that reported for a larval oyster in Kudo *et al.* (2010). Grain boundaries other than the {110} twins were not observed in the plane-view specimen of a few micrometers. This is probably related to that the shell formation proceeds by expanding laterally to cover the embryo, starting from a specific site (the shell gland). The high density of the {110} twins may be the result of fast lateral growth of the layer, which is preferable to isolate quickly the embryo from the outer environment. In 48 hours cell, a new layer, which was called a “granular homogeneous layer” or “globular homogeneous layer” in the previous works (Waller, 1981; Weiss *et al.*, 2002), is formed, inside the outer layer. These granules have uniaxial (the ***c***-axis) orientation preference and the orientation of the other axes are not strictly controlled. Finally, the inner prismatic layer is formed on the granular homogeneous layer as the third and innermost layer. However, plane-view TEM images revealed that

the outer and inner “prismatic” layers have considerably different textures, although the contrasts appeared in the cross-sectional bright-field TEM image are similar (Fig. 3-8c). The inner prismatic layer is composed of really “prismatic” grains with irregular grain boundaries (Fig. 3-8g).

There is no interlayer material such as a continuous organic sheet between these layers with different textures. Moreover, some adjacent granules and prisms show the same contrast in the bright-field TEM images, indicating crystallographic continuity across the boundaries (Fig. 3-8f). Hence a question is how the organism creates the multilayer structure with different textures in the larval shell. A possible explanation is that when the shell grows from the outermost layer inwards, their growth is interfered or partly disconnected by organic substance secreted during a certain period from the embryo, which results in the formation of the granular homogeneous layer at the center of the shell. Recently Gries *et al.* (2009) observed the spherules with dark contrast in the aragonite crystals of nacre using HAADF-STEM imaging. They also identified the spherules to be organic substance using electron energy loss spectroscopy (EELS). As shown in Fig. 3-9, such dark-contrasted spherules were selectively observed in the granular homogeneous layer, implying that organic substance or molecules are abundant only in this layer. The amount of the organic molecules may select the layer structure to be “granular” or “prismatic”.

As mentioned above, Weiss *et al.* (2002) investigated microstructure of the larval shells of the marine bivalves, *Mercenaria mercenaria* and *Crassostrea gigas*, using SEM, Raman and infrared spectroscopy, etc. They suggested that ACC is the dominant phase in the larval shells, which subsequently transforms to aragonite during shell growth. This conclusion was mainly derived from Raman spectroscopy and SEM

observation of fractured surfaces of the shell after water-etching. These results seem contradictory to those in the present study using FIB-TEM, in which no evidence has been found in TEM for the existence of ACC. One may suspect that the FIB sample preparation might induce the transformation of ACC to crystalline aragonite. FIB is a vacuum process in which water molecules may be released from ACC and also Ga-beam radiation raises the specimen temperature to some extent, close to 100°C. However, it is also true that ACC did not transform to a crystalline phase by our FIB process, as shown in Chapter 1. Synthesized ACC prepared using FIB process was also observed as amorphous phase in TEM (Suzuki *et al.*, 2006). Another point to be discussed is whether the microstructure of the larval shell found in the present study can be formed from ACC during FIB-TEM process. For instance, the initial prismatic layer (Fig. 3-4) where the ***c***-axis of aragonite is completely regulated and the layer has a single-crystalline nature in a wide range, although the {110} twins are dense. The granular layer has an ACC-like surface morphology (Fig. 3-8b, e) but the constituting aragonite still possesses the oriented ***c***-axis. Such crystallographic property seems difficult to form via ACC. It could be suspected that such regulation of the crystal axis during the crystallization of ACC in FIB-TEM process is attained with seed crystals coexisting with ACC. Actually the mixture of aragonite and ACC in the granular layer is proposed in Weiss *et al.* (2002). However, if the seed crystals were formed before ACC precipitation, it seems that the organism has no necessity to precipitate ACC afterwards, which can be synthesized in laboratory only with far-equilibrium condition.

2. Larval shell structures of the other species

In addition, the larval shells of *N. fuscoviridis, C. sandai* and *B. glabrata* were investigated to understand the similarity and differences among molluscan species.

Although most of the previous studies are for Pteriomorphia species (*e.g.* Waller *et al.*, 1981; Mao Che *et al.*, 2001), almost all mollusks seem to form a three-layered structure consisting of aragonite in their larval shell. As exceptions, A thick layer formed with calcite was found in an individual of *N. fuscoviridis* and *P. fucata* sampled in Mie, 2008. Such variation may have been caused by mutation of homologous gene between *P. fucata* and *N. fuscoviridis*. The microstructures of these three layers are also common in some respects; the outer and inner layers have prismatic textures and the middle layer between them shows a globular or granular texture. However, the detail of the middle globular layer is different between Bivalvia and Gastropoda. The constituting aragonite crystals in the globular layer have a rather isotropic shape in the two bivalves, *P. fucata* and *C. sandai*. This aspect may be common for bivalves, if considering the results in previous studies as well as the present one (*e.g. Pinctada margaritifera*, Mao Che *et al.*, 2001; *Mercenaria mercenaria*, Weiss *et al.*, 2002; *Crassostrea nippona*, *Kudo et al.*, 2010). In contrast, two gastropods (*N. fuscoviridis* and *B. glabrata*) form the globular layer in which the aragonite crystals are elongated laterally or in parallel to the shell surface. In spite of such difference, the ***c***-axis of aragonite is oriented normal to the shell surface in all layers and species. In addition, although Marxen and Becker (1997) suggested that the adult shell of *B. glabrata* forms crossed-lamellar structure, the larval crossed-lamellar structure is a little different. Kobayashi and Akai (1994) suggested the adult lamellar structure consists of three orders, but the larval lamellar seems not to have the first order unit. Table 3-2 summarize the shell structures of larvae. The common ancestor between bivalves and gastropods may have formed three-layered structure with outer and inner prismatic layer with their ***c***-axes normal to the shell surface.

Table 3-2. Summary of the larval shell structures. 1; Waller (1981), 2; Castilho *et al.* (1989), 3; Mao Che *et al.* (2001), 4; Weiss *et al.* (2002), 5; Auzoux-Bordenave *et al.* (2010) and 6; Kudo *et al.* (2010). OPL; the outer prismatic layer, GL; the globular layer, IPL; the inner prismatic layer.

References	species	water	class	OPL	GL	IPL
This thesis	*Pinctada fucata*	sea	Bivalvia	prism	granule	prism
This thesis	*Nippoacmea fuscoviridis*	sea	Gastropoda	prism	elongated	prism
This thesis	*Corbicula sandai*	fresh	Bivalvia	prism	granule	?
This thesis	*Biompharalia glabrata*	fresh	Gastropoda	prism	elongated	prism
1	*Ostrea edulis*	sea	Bivalvia	prism	granule	prism
2	*Anodonta cygnea*	fresh	Bivalvia	prism	granule	?
3	*Pinctada margaritifera*	sea	Bivalvia	prism	granule	?
4	*Crassostrea gigas*	sea	Bivalvia	prism	granule	prism
4	*Meretrix meretrix*	sea	Bivalvia	prism	granule	prism
5	*Haliotis tuberculata*	sea	Gastropoda	prism	elongated	prism
6	*Crassostrea nippona*	sea	Bivalvia	prism	granule	?

Additionally, the microstructure of the middle globular layer can be applied to classification of mollusks. Recently, some studies suggested a new genetic relationship (Kocot *et al.*, 2011; Smith *et al.*, 2011; Telford and Budd, 2011). The new phylogenic tree suggested that Gastropoda, Bivalvia and Cephalopoda are close, and Monoplacophora and Cephalopoda forms sister group. The reports shows similar phylogenic tree, but the relationship between Gastropoda, Bivalvia and Cephalopoda is still not unclear (Fig. 3-19).

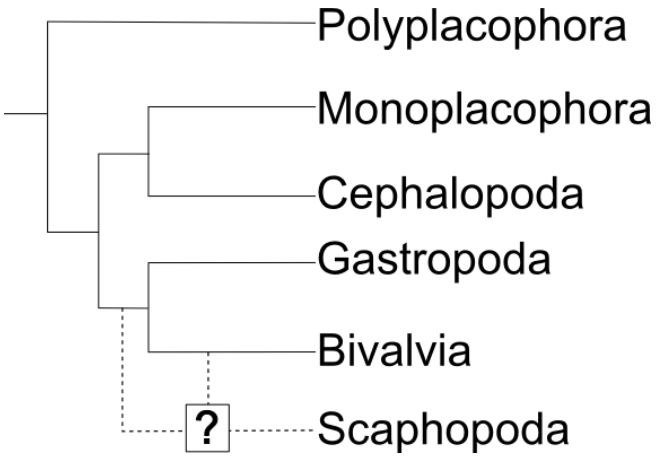

Fig. 3-19. New phylogenic tree of molluscs. The genetic relationship was derived from Kocot *et al.* (2011), Smith *et al.* (2011), Telford and Budd (2011).

In this thesis, it was observed that the general structures of the larval shell are common between Bivalvia and Gastropoda. Thus, the relationship is possible to make clear by observing the larval shell microstructure of Scaphopoda. In addition, if the larval shells of the other classes are investigated, the structural commonality can be traced back to the first shell formation and may indicate that the structure of the larval shell is almost common in all classes.

3-5. Conclusions

All species investigated in this study form the three-layered structure as their larval shell. All the three layers consist of aragonite whose ***c***-axis is oriented normal to the shell surface. It is likely that this feature is common for all molluscan larvae. In contrast, the structure of the middle layer is different between bivalves and gastropods. Bivalves form a dense aggregate of fine aragonite granules, but gastropods form aragonite grains elongated parallel to the shell surface interspaced with organic matrices. In *P. fucata*, the outer prismatic layer consists of wide and thin aragonite plates containing dense {110} twins and few grain boundaries. The inner prismatic layer is made of prismatic crystals of aragonite. The outer and inner prismatic layers have few organic matrices although the middle globular layer contains a considerable amount of organic matrices. It is suggested that the amounts of these organic matrices differentiate the prismatic and globular layers.

My detailed TEM observations in this study have not found any ACC-like inorganic materials in the larval shells. As mentioned above, it is suspected that FIB sample preparation, in which the specimen is heated to ~ 100 °C in vacuum, may have induced the crystallization of ACC. However, as shown in Chapter 1 and Appendix of this thesis, ACC in the cuticle of the terrestrial isopod and synthetic ACC were preserved as "amorphous" after the FIB process. Moreover, it is expected ACC transforms to calcite by heating (see Appendix). During the observation, aragonite was the only crystalline calcium carbonate phase in the larval shells except large calcite crystals in the bivalves, which seems to be formed by mutation. Accordingly, it is suggested at present that ACC does not exist in the molluscan larval shells.

Chapter 4

Conclusions of the thesis

This thesis has aimed at the further understanding of biomineralization related to ACC. For this purpose, I have adopted two kinds of samples. One is the terrestrial isopod, *A. vulgare*, and another is larval shells of several molluscan species. The reasons to select them are different from each other. The former was selected mainly to reveal the structural characteristic of crystalline calcium carbonate (calcite) transformed from ACC. The purpose to investigate the molluscan larval shells was to elucidate the existence or nonexistence of ACC as a precursor of aragonite. Besides, the latter study must be important as crystallographic descriptions of molluscan larval shells using TEM, which were seldom reported in previous works.

Previous studies reported that the cuticle of *A. vulgare* at the intermolt stage consists of three calcified layers and one uncalcified layer; distal layer (calcite), transition zone (calcite), endocuticle (ACC), and membranous layer (uncalcified). The present study has revealed that calcite in the transition zone is crystallized from ACC and the calcite crystals have distinct features with respect to their crystal size and orientation; the crystals in the upper transition zone have the identical orientations to those of calcite in the distal layer, whereas the lower transition zone consists of nano-crystalline calcites with their ***c***-axes parallel to the organic fibers. Hence, calcite crystals in the upper transition zone are suggested to be formed by epitaxial growth, taking over the crystal orientation from the distal layer. In contrast, crystallization is regulated by organic fibers in the lower transition zone.

Next, larval molluscan shell of the pearl oyster, *Pinctada fucata*, has been investigated at several stages after fertilization to elucidate the shell microstructure and possibility of the existence of ACC during their formations. The shells were investigated mainly using TEM with the specimens fabricated using the focused-ion-beam (FIB)

technique. A three-layered structure has been identified in the larval shell and each layer has the following characteristic structure;

(1) The outer prismatic layer contains dense multiple {110} twins and few grain boundaries.

(2) The middle globular layer is actually the mixture of the areas with multiple {110} twins and with a polycrystalline feature. However, the ***c***-axes of the aragonite crystals are oriented normal to the surface, regardless of such structural difference.

(3) The inner prismatic layer consists of "prismatic crystals" with distinct grain boundaries.

Although the analysis of the shell structure was not as complete as that for *P. fucata*, I have investigated the larval shells of other three species selected from seawater Gastropoda, freshwater bivalve, and freshwater Gastropoda. All of them have a three-layered structure, all of which consist of aragonite whose ***c***-axes are oriented normal to the shell surface. Hence, it was revealed that the basic design of the larval shell is very close among these species, or in bivalve and Gastropoda. During these analyses, I did not find ACC or any structures which suggest the existence of ACC as a precursor phase in the larval shells of *P. fucata* and other species. Considering the results in Chapter 2 and characterization of synthetic ACC (Appendix), the transformation of ACC to aragonite by the FIB sample preparation process seems unlikely.

Because ACC has not been reported in nature except biominerals, this material is regarded as the specific one only prepared by biomineralization. The result in Chapter 1 indicates that the calcite transformed from ACC can have various crystallographic features, depending on the substrates or templates. This is an important finding, as a successful result in this thesis.

In this thesis, I suggest from TEM investigation that ACC is not formed in molluscan larval shells, as an opposition to several recent studies referred in this thesis. As mentioned before, this argument is very important, if the future environmental change and high solubility of ACC are considered. Hence, it is desired that the involved researchers will continue working to present conclusive result for this issue.

Acknowledgements

First, Prof. Toshihiro Kogure gave me a chance for this study, and he gave me many useful advices from beginning to end. I express sincere gratitude meaning here. Prof. Hiroyuki Kagi operated some analysis instruments, and gave me many useful advices as a chief examinar. I am deeply grateful to his helps. Prof. Takashi Murakami, Prof. Kazuyoshi Endo and Prof. Takenori Sasaki gave me many advices as an associate examinar. Prof. Takashi Murakami usually gave me some advices at SES seminar, and Prof. Kazuyoshi Endo and Prof. Takenori Sasaki provided some larvae samples. I am deeply grateful to their helps. Prof. Hiromichi Nagasawa, department of the agricultural and life sciences of Univ. Tokyo, occasionally gave me some important advices. Prof. Yohei Suzuki gave me useful and kind advices at SES seminar. Dr. Hideo Aoki, a researcher of Mie Fisheries Institute, provided me many *P. fucata* larvae, one of the core samples of this study. He also gave me some important advices about sampling. Prof. Hiroshi Wada and Dr. Yoshihisa Kurita, department of life and environment sciences of Univ. Tsukuba, provided me *N. fuscoviridis* larvae. Dr. Daisuke Ishizaki and Dr. Masataka Hatano provided me *C. sandai* larvae. Dr. Kazuko Saruwatari, Jun Kameda, Michio Suzuki, Katsuaki Watanabe provided me many directions not only about experimental methods but also experimental lines. Mr. Koji Ichimura taught me directions to use analyses instruments, such as SEM and XRD. Ms. Eiko Fujii taught me about the use of methods of FIB sample preparation system. Finally, graduate / graduated students who belong to SES seminar and classmates helped me in various ways. I would like to express my deep gratitude to these people.

References

Addadi, L., Joester, D., Nudelman, F., Weiner, S.: Mollusk shell formation: a source of new concepts for understanding biomineralization processes. *Chemistry-A European Journal*, **12**, 980-987, 2006

Addadi, L., Raz, S., Weiner, S.: Taking advantage of disorder: amorphous calcium carbonate and its roles in biomineralization. *Advanced Materials*, **15**, 959-970, 2003

Addadi, L. and Weiner, S.: Biomineraliation: a pavement of pearl. *Nature*, **389**, 912-915, 1997

Aizenberg, J., Lambert, G., Addadi, L., Weiner, S.: Stabilization of amorphous calcium carbonate by specialized macromolecules in biological and synthetic precipitates. *Advanced Materials*, **8**, 222-226, 1996

Aoki, J. (Ed.): Pictorial keys to soil animals of Japan. *Tokai university press*, 1991 (In Japanese with English abstract)

Auzox-Bordenave, S., Badou, A., Gaume, B., Berland, S., Helléouet, M. N., Milet, C., Huchette, S.: Ultrastructure, chemistry and mineralogy of the growing shell of the European abalone *Haliotis tuberculata*. *Journal of Structural Biology*, **171**, 277-290, 2010

Bassett, D. C., Marelli, B., Nazhat, S. N., Barralet, J. E.: Stabilization of amorphous calcium carbonate with nanofibrillar biopolymers. *Advanced Functional Materials*, **22**, 3460-3469, 2012

Becker, A., Bismayer, U., Epple, M., Fabritius, H., Hasse, B., Shi, J., Ziegler, A.: Structural characterisation of X-ray amorphous calcium carbonate (ACC) in sternal deposits of the crustacea *Porcellio scaber*. *Journal of the Chemical Society, Dalton transactions*, **4**, 551-555, 2003

Becker, G. L., Chen, C., Greenwalt, J. W., Lehninger, A. L.: Calcium phosphate granules in the hepatopancreas of the blue crab *Callinectes sapidus*. *Journal of Cell Biology*, **61**, 316-326, 1974

Becker, A., Ziegler, A., Epple, M.: The mineral phase in the cuticles of two species of Crustacea consists of magnesium calcite, amorphous calcium carbonate, and amorphous calcium phosphate. *Journal of the Chemical Society, Dalton transactions*, **10**, 1824-1820, 2005

Bentov, S., Weil, S., Glazer, L., Sagi, A., Berman, A.: Stabilization of amorphous calcium carbonate by phosphate rich organic matrix proteins and by single phosphoamino acids. *Journal of Structural Biology*, **171**, 207-215, 2010

Bots, P., Benning, L. G., Rodriguez-Blanco, J. D., Roncal-Herrero, T., Shaw, S.: Mexhanistic insights into the crystallization of amorphous calcium carbonate (ACC). *Crystal Growth & Design*, **12**, 3806-3814, 2012

Brečević, L. and Nielsen, A. E.: Solubility of amorphous calcium carbonate. *Journal of Crystal Growth*, **98**, 504-510, 1989

Calvert, P. and Mann, S.: Review: synthetic and biological composites formed by *in situ* precipitation. *Journal of Materials Science*, **23**, 3801-3815, 1988

Carriker, M., R. and Palmer, R. E.: Ultrastructural morphogenesis of prodissoconch and early dissoconch valves of the oyster *Crassostrea virginica*. *College of Marine Studies, University of Delaware*, 1979

Castilho, F., Machado, J., Reis, M. L., Sá, C.: Ultrastructural study of the embryonic and larval shell of *Anodonta cygnea*. *Canadian Journal of Zoology*, **67**, 1659-1664, 1989

Clarkson, J. R., Price, T. J., Adams, C. J.: Role of metastable phases in the spontaneous

precipitation of calcium carbonate. *Journal of the Chemical Society, Faraday transactions*, **88**, 243-249, 1992

Deguchi, R.: Developmental processes in marine limpets and the use for biology education. *Bulletin of Miyagi University of Education*, **42**, 72-80, 2007 (In Japanese with English abstract)

Dillaman, R., Hequembourg, S., Gay, M.: Early pattern of calcification in the dorsal carapace of the blue crab, *Callinectes sapidus*. *Journal of Morphology*, **263**, 356-374, 2005

Frenzel, M. and Harper, E. M.: Micro-structure and chemical composition of vateritic deformities occurring in the bivalve *Corbicula fluminea* (Müller, 1774). *Journal of Structural biology*, **174**, 321-332, 2011

Fujimura, T., Wada, K., Iwaki, T.: Development and morphology of the Pearl Oyster larvae, *Pinctada fucata*. *VENUS; the Japanese Journal of Malacology*, **54**, 25-48, 1995 (In Japanese with English abstract)

Gal, J. Y., Bollinger, J. C., Tolosa, H., Gache, N.: Calcium carbonate solubility: a reappraisal of scale formation and inhibition. *Talanta*, **43**, 1497-1509, 1996

Gal, A., Weiner, S., Addadi, L.: The stabilizing effect of silicate on biogenic and synthetic amorphous calcium carbonate. *Journal of American Chemical Society*, **132**, 13208-13211, 2010

Gebauer, D., Gunawidjaja, P. N., Ko, J. Y. P., Bacsik, Z., Aziz, B., Liu, L., Hu, Y., Bergström, L., Tai, C. W., Sham, T. K., Edén, M., Hedin, N.: Proto-calcite and proto-vaterite in amorphous calcium carbonates. *Angewandte Chemie Internal Edition*, **49**, 8889-8891, 2010

Gebauer, D., Völkel, A., Cölfen, H.: Stable prenucleation calcium carbonate clusters.

Science, **322**, 1819-1822, 2008

Gilis, M., Grauby, O., Willenz, P., Dubois, P., Legras, L., Heresanu, V., Baronnet, A.: Multi-scale mineralogical characterization of the hypercalcified sponge *Petrobiona massiliana* (Calcarea, Calcaronea). *Journal of Structural Biology*, **176**, 315-329, 2011

Gorna, K., Hund, M., Vučak, M., Gröhn, F., Wegner, G.: Amorphous calcium carbonate in form of spherical nanosized particles and its application as fillers for polymers. *Materials Science and Engineering A*, **477**, 217-225, 2008

Gries, K., Kröger, R., Kübel, C., Schowalter, M., Fritz, M., Rosenauer, A.: Correlation of the orientation of stacked aragonite platelets in nacre and their connection via mineral bridges. *Ultramicroscopy*, **109**, 230-236, 2009

Hasse, B., Ehrenburg, H., Marxen, J. C., Becker, W., Epple, M.: Calcium carbonate modifications in the mineralized shell of the freshwater snail *Biomphalaria glabrata*. *Chemistry-A European Journal*, **6**, 3679-3685, 2000

Hayashi, K.: Ecological studies on the useful Mollusca in Lake Biwa (first part). *VENUS; the Japanese Journal of Malacology*, **31**, 9-34, 1972

Hikida, T: Investigation of the formation mechanism of amorphous calcium carbonate (ACC) in the gastrolith of crayfish, *Procambarus clarkii*. *Master thesis*, 2002

Hild, S., Marti, O., Ziegler, A.: Spatial distribution of calcite and amorphous calcium carbonate in the cuticle of the terrestrial crustaceans *Porcellio scaber* and *Armadillidium vulgare*. *Journal of Structural Biology*, **163**, 100-108, 2008

Hild, S., Neues, F., Znidarsic, N., Štrus, J., Epple, M., Marti, O., Ziegler, A.: Ultrastructure and mineral distribution in the tergal cuticle of the terrestrial isopod *Titanethes albus*. Adaptations to a karst cave biotope. *Journal of Structural Biology*,

168, 426-436, 2009

Jacob, D. E., Wirth, R., Soldati, A. L., Wehrmeister, U., Schreiber, A.: Amorphous calcium carbonate in the shells of adult Unionoida. *Journal of Structural Biology*, **173**, 241-249, 2011

Kayano, K., Saruwatari, K., Kogure, T., Shiraiwa, Y.: Effect of coccolith polysaccharides isolated from the coccolithophorid, *Emiliania huxleyi*, on calcite crystal formation in *in vitro* $CaCO_3$ crystallization. *Marine Biotechnology*, **13**, 83-92, 2011

Kellermeier, M., Meleno-García, E., Glaab, F., Klein, R., Drechsler, M., Rachel, R., García-Ruiz, J. M., Kunz, W.: Stabillization of amorphous calcium carbonate in inorganic silica-rich environments. *Journal of American Chemical Society*, **132**, 17859-17866, 2010

Kniprath, E.: Larval development of the shell and the shell gland in Mytilus (Bivalvia). *Wilhelm Roux's Archives*. **188**, 201-204, 1980

Kniprath, E.: Ontogeniy of the molluscan shell field: a review. *Zoologica Scripta*, **10**, 61-79, 1981

Kobayashi, I.: Various patterns of biomineralization and its phylogenetic significance in bivalve mollusks. In Omori, M., Watabe, N. Eds., The mechanism of biomineralization in animals and plants. *Tokai Univ. Press*, 145-155, 1980

Kobayashi, I.: Shell structure of *Pinctada fucata martensii* (DUNKER) in the larval and juvenile stages. *Earth Science*, **35**, 245-252, 1981 (in Japanese with English abstract)

Kobayashi, I. and Akai, J.: Twinned aragonite crystals found in the bivalvian crossed lamellar shell structure. *Journal of Geological Society of Japan*, **100**, 177-180, 1994

Kobayashi, I., and Takayasu, K.: Internal shell microstructure of two species of Japanese brackish-water. *LAGUNA*, **2**, 33-51, 1995 (In Japanese with English abstract)

Kocot, K. M., Cannon, J. T., Todt, C., Citarella, M. R., Kohn, A. B., Meyer, A., Santos, S. R., Schander, C., Moroz, L. L., Lieb, B., Halanych, K. M.: Phylogenomics reveals deep molluscan relationships. *Nature*, **477**, 452-456, 2011

Koga, N., Nakagoe, Y., Tanaka, H.: Crystallization of amorphous calcium carbonate. *Thermochimica Acta*, **318**, 239-244, 1998

Kojima, Y., Kanai, M., Nishimiya, N.: Synthesis of novel amorphous calcium carbonate by sono atomization for reactive mixing. *Ultrasonics Sonochemistry*, **19**, 325-329, 2012

Kojima, Y., Kawanobe, A., Yasue, T., Arai, Y.: Synthesis of amorphous calcium carbonate and its crystallization. *Journal of the Ceramic Society of Japan*, **101**, 1145-1152, 1993

Kudo, M., Kameda, J., Saruwatari, K., Ozaki, N., Okano, K., Nagasawa, H., Kogure, T.: Microtexture of larval shell of oyster, *Crassostrea nippona*: A FIB-TEM study. *Journal of Structural Biology*, 169, 1-5, 2010

Lam, R. S. K., Charnock, J. M., Lennie, A., Meldrum, F. C.: Synthesis-dependant structural variations in amorphous calcium carbonate. *CrystEngComm*, **9**, 1226-1236, 2007

Levi-Kalisman, Y., Raz, S., Weiner, S., Addadi, L., Sagi, I.: Structural differences between biogenic amorphous calcium carbonate phases using X-ray absorption spectroscopy. *Advanced Functional Materials*, **12**, 43-48, 2002

Mansot, J. L., Golabkan, V., Romana, L., Césaire, T.: Chemical and physical

characterization by EELS of strontium hexanoate reverse micelles and strontium carbonate nanophase produced during tribological experiments. *Journal of Microscopy*, **210**, 110-118, 2003

Mao Che, L., Gobulic, S., Le Campion-Alsumard, T., Payri, C.: Developmental aspects of biomineralisation in the Polynesian pearl oyster *Pinctada margaritifera var. cumingii*. *Oceanologica Acta*, **24**, S37-S49, 2001

Marin, F., Luquet, G.: Molluscan shell proteins. *Comptes Rendus Palevol*, **3**, 469-492, 2004

Maruyama, K., Yoshino, T., Kagi, T.: Synthesizing a composite material of amorphous calcium carbonate and aspartic acid. *Materials Letters*, **65**, 179-181, 2011

Marxen, J. C. and Becker, A.: The organic shell matrix of the freshwater snail *Biompharalia glabrata*. *Comparative Biochemistly and Physiology B*, **118**, 23-33, 1997

Marxen, J. G., Becker, W., Finke, D., Hasse, B., Epple, M.: Early mineralization in *Biomphalaria glabrata*: microscopic and structural results. *Journal of Molluscan Studies*, **69**, 113-121, 2003

Medaković, D., Hrs-Brenko, M., Popović, S., Gržeta, B.: X-ray diffraction study of the first larval shell of *Ostrea edulis*. *Marine Biology*, *101*, 205-209, 1989

Miyamoto, H., Miyashita, T., Okushima, M., Nakano, S., Morita, T., Matsushiro, A.: A carbonic anhydrase from the nacreous layer in oyster pearls. *Proceedings of the National Academy of Sciences*, **93**, 9657–9660, 1996

Mouěza, M., Gros, O., Frenkiel, L.: Embryonic development and shell differentiation in *Chione cancellata* (Bivalvia, Veneridae): an ultrastructural analysis. *Invertebrate Biology*, **125**, 21-33, 2006

Nagasawa, H.: Calcification/decalcification mechanisms associated with molting. In Sonobe, H. and Nagasawa, H. eds., Biology of molting and metamorphosis – Mechanism of hormonal regulation in insects and crustaceans. *Tokai University Press*, 439-454, 2011 (In Japanese)

Neues, F., Hild, S., Epple, M., Marti, O., Ziegler, A.: Amorphous and crystalline calcium carbonate distribution in the tergite cuticle of moulting *Porcellio scaber* (Isopoda, Crustacea). *Journal of Structural Biology*, 175, 10-20, 2011

Nudelman, F., Sonmezler, E., Bomans, P. H. H., de With, G., Sommerdijk, N. A. J. M.: Stabilization of amorphous calcium carbonate by controlling its particle size. *Nanoscale*, **2**, 2436-2439, 2010

Ogino, T., Suzuki, T., Sawada, K.: The formation and transformation mechanism of calcium carbonate in water. *Geochimica et Cosmochimica Acta*, **51**, 2757-2767, 1987

Okumura, T., Suzuku, M., Nagasawa, H., Kogure, T.: Characteristics of biogenic calcite in the prismatic layer of a pearl oyster, *Pinctada fucata*. *Micron*, **41**, 821-826, 2010

Okutani, T.: Marine mollusks in Japan. *Tokai Univ. Press*, 2000

Orr, J. C., Fabry, V. J., Aumont, O., Bopp, L., Doney, S. C., Feely, R. A., Gnanadesikan, A., Gruber, N., Ishida, A., Joos, F., Key, R. M., Lindsay, K., Maier-Reimer, E., Matear, R., Monfray, P., Mouchet, A., Najjar, R. G., Platter, G.-K., Rodgers, K. B., Sabine, C. L., Sarmiento, J. L., Schlitzer, R., Slater, R. D., Totterdell, I. J., Weirig, M.-F., Yamanaka, Y., Yool, A.: Anthropogenic ocean acidification over the twenty-first century and its impact on calcifying organisms. *Nature*, **437**, 681-686, 2005

Politi, Y., Arad, T., Klein, E., Weiner, S., Addadi, L.: Sea urchin spine calcite forms via a

transient amorphous calcium carbonate phase. *Science*, **306**, 1161-1164, 2004

Politi, Y., Metzler, R. A., Abrecht, M., Gilbert, B., Wilt, F. H., Sagi, I., Addadi, L., Weiner, S., Gilbert, P. U. P. A.: Transformation mechanism of amorphous calcium carbonate into calcite in the sea urchin larval spicule. *Proceedings of the National Academy of Sciences*, **105**, 17362-17366, 2008

Raabe, D., Romano, P., sachs, C., Al-Sawalmih, A., Brokmeier, H. G., Yi, S. B., Servos, G., Hartwig, H. G.: Discovery of a honeycomb structure in the twisted plywood patterns of fibrous biological nanocomposite tissue. *Journal of Crystal Growth*, **283**, 1-7, 2005

Raabe, D., Romano, P., Sachs, C., Fabritius, H., Al-Sawalmih, A., Yi, S. B., Servos, G., Hartwig, H. G.: Microstructure and crystallographic texture of the chitin–protein network in the biological composite material of the exoskeleton of the lobster *Homarus americanus*. *Materials Science and Engineering, Part A*, **421**, 143-153, 2006

Rodrigues-Blanco, J. D., Shaw, S., Benning, L. G.: How to make 'stable' ACC: protocol and preliminary structural characterization. *Mineralogical Magazine*, **72**, 283-286, 2008

Rodriguez-Blanco, J. D., Shaw, S., Benning, L. G.: The kinetics and mechanisms of amorphous calcium carbonate (ACC) crystallization to calcite, via vaterite. *Nanoscale*, **3**, 265-271, 2011

Romano, P., Fabritius, H., Raabe, D.: The exoskeleton of the lobster *Homarus americanus* as an example of a smart anisotropic biological material. *Acta Biomaterialia*, **3**, 301-309, 2007

Samata, T., Hayashi, N., Kono, M., Hasegawa, K., Horita, C., Akera, S.: A new matrix

protein family related to the nacreous layer formation of *Pinctada fucata*. *FEBS Letters*, **462**, 225-229, 1999

Sasaki, T. and Fuchigami, T.: The shell structure of the recent Patellogastropoda (Mollusca: Gastropoda). *Paleontological Research*, **9**, 143-168, 2005

Sasaki, T. and Okutani, T.: New genus *Nippoacmea* (Gastropoda, Lottiidae): a revision of Japanese limpets hitherto allocated in *Notoacmea*. *VENUS; the Japanese Journal of Malacology*, **52**, 1-40, 1993

Sato, A., Nagasaka, S., Furihata, K., Nagata, S., Arai, I., Saruwatari, K., Kogure, T., Sakuda, S., Nagasawa, H.: Glycolytic intermediates induce amorphous calcium carbonate formation in crustaceans. *Nature Chemical Biology*, **7**, 197-199, 2011

Saur, M., Moeller, V., Kapetanopoulos, K., Braumann, S., Gebauer, W., Tenzer, S., Markl, J.: Acetylcholine-binding protein in the Hemolymph of the planorbid snail *Biomphalaria glabrata* is a pentagonal dodecahedron. *PLOS one*, **7**, 1-14, 2012

Sawada, K.: The mechanisms of crystallization and transformation of calcium carbonates. *Pure and Applied Chemistry*, **69**, 921-928, 1997

Seidl, B. H. M., Huemer, K., Neues, F., Hild, S., Epple, M., Ziegler, A.: Ultrastructure and mineral distribution in the tergite cuticle of the beach isopod *Tylos europaeus Arcangeli*, 1938. *Journal of Structural Biology*, **174**, 512-526, 2011

Seidl, B. H. M., Reisecker, C., Hild, S., Griesshaber, E., Ziegler, A.: Calcite distribution and orientation in the tergite exocuticle of the isopods *Porcellio scaber* and *Armadillidium vulgare* (Oniscidea, Crustacea) – a combined FE-SEM, polarized SCμ-RSI and EBSD study, *ZEITSCHRIFT FUR KRISTALLOGRAPHIE*, **227**, 777-792, 2012

Seidl, B. H. M. and Ziegler, A.: Electron microscopic and preparative methods for the

analysis of isopod cuticle. *Zookeys*, **176**, 73-85, 2012

Smith, S. A., Wilson, N. G., Goetz, F. E., Feehery, C., Andrate, S. C. S., Rouse, G. W., Giribet, G., Dunn, C. W.: Resolving the evolutionary relationships of molluscs with phylogenomic tools. *Nature*, **480**, 364-369, 2011

Stenzel, H.B.: Oysters: composition of the larval shell. *Science*, **145**, 155–156, 1964

Su, X.W., Zhang, D.M., Heuer, A.H.: Tissue regeneration in the shell of the giant queen conch, *Strombus gigas*. *Chemical Materials*, **16**, 581-593, 2004

Sun, L., Du, Y., Yang, J., Shi, X., Li, J., Wang, X., Kennedy, J. F.: Conversion of crystal structure of the chitin to facilitate preparation of a 6-carboxychitin with moisture absorption–retention abilities. *Carbohydrate Polymers*, **66**, 168-175, 2006

Suzuki, M., Nagasawa, H.: The structure-function relationship analysis of Prismalin-14 from the prismatic layer of the Japanese pearl oyster, *Pinctada fucata*. *FEBS Journal*, **274**, 5158-5166, 2007

Suzuki, M., Nagasawa, H., Kogure, T.: Synthesis and structure of hollow calcite particles. *Crystal Growth & Design*, **6**, 2004-2006, 2006

Tao, J., Zhou, D., Zhang, Z., Xu, X., Tang, R.: Magnesium-aspartate-based crystallization switch inspired from shell molt of crustacean. *Proceedings of the National Academy of Sciences*, **106**, 22096-22101, 2009

Taylor, J.D., Kennedy, W.J., Hall, A.: The shell structure and mineralogy of the Bivalvia. Introduction: Nuculacea-Trigonacea. *Bulletin of the British Museum (Natural Histry), (D: Zoology)*, **3** (Suppl.), 1–125, 1969

Taylor, J.D., Kennedy, W.J., Hall, A.: The shell structure and mineralogy of the Bivalvia. Nuculacea-Trigonacea, Conclusions. *Bulletin of the British Museum (Natural Histry), (D: Zoology)*, **22**, 253-294, 1973

Telford, M. J. and Budd, G. E.: Invertebrate evolution: bringing order to the molluscan chaos. *Current Biology*, **21**, R964-R966, 2011

Wada, K.: Studies on the component of pearl-oyster shell (*Pinctada martensii*) by means of X-ray diffraction and differential thermal analysis. *Bulletin of National Pearl Research Laboratory*, **1**, 7-9, 1956 (In Japanese with English abstract)

Wada, K.: Electron-microscopic observations on the shell structures of pearl oyster (*Pinctada martensii*).II. Observations of the aragonite crystals on the surface of nacreous layers. *Bulletin of National Pearl Research Laboratory*, **2**, 74-85, 1957 (In Japanese with English abstract),

Waller, T.R.: Functional morphology and development of veliger larvae of the European oyster, *Ostrea edulis Linné*. *Smithsonian Contributions to Zoology*, **328**, 1–70, 1981

Watabe, N.: Shell structure: The Mollusca. *Academic Press*, 69–104 (1988)

Weiss, I. M., Tuross, N., addadi, L., Weiner, S.: Mollusc larval shell formation: amorphous calcium carbonate is a precursor phase for aragonite. *Journal of experimental zoology*, **293**, 478-491, 2002

Zhang, S. M. and Coultas, K. A.: Identification and characterization of five transcription factors that are associated with evolutionarily conserved immune signaling pathways in the schitosome-transmitting snail *Biomphalaria glabrata*. *Molecular Immunology*, **48**, 1868-1881, 2011

Zidar, P., Drobne, D., Štrus, J.: Determination of moulting stages of *Porcellio scaber* (isopoda) for routine use. *Crustaceana*, **71**, 646-654, 1998

Ziegler, A., Fabritius, H., Hagedorn, M.: Microscopical and functional aspects of calcium-transport and deposition in terrestrial isopods. *Micron*, **36**, 137-153, 2005

Ziegler, A. and Merz, E.: Membrane particle distribution in the sternal epithelia of the

terrestrial isopod *Porcellio scaber Latr.* (Crustacea, Oniscidea) during $CaCO_3$ deposit formation and resorption, a freeze-etch analysis. *Journal of Structural Biology*, **127**, 263-278, 1999

Ziegler, A., Weihrauch, D., Towle, D. W., Hagedorn, M.: Expression of Ca^{2+}-ATPase and Na^{+}/Ca^{2+}-exchanger is upregulated during epithelial Ca^{2+} transport in hypodermal cells of the isopod *Porcellio scaber*. *Cell Calcium*, **32**, 131-141, 2002

Ziegler, A., Hagedorn, M., Ahearn, G. A., Carefoot, T. H.: Calcium translocations during the moulting cycle of the semiterrestrial isopod *Ligia hawaiiensis* (Oniscidea, Crustacea). *Journal of Comparative Physiology B*, **177**, 99-108, 2007

Appendix

Crystallization process of synthetic amorphous calcium-magnesium carbonate

Abstract

In order to investigate biomineralization relevant to amorphous calcium carbonate (ACC), the characters of this material itself should be well understood. For this purpose, ACC samples containing various amounts of magnesium (amorphous calcium-magnesium carbonate: ACMC) were synthesized and their behavior to transform to crystalline forms was investigated. In a humid condition, ACMC transformed to vaterite and calcite, or Mg-calcite if the concentration of Mg was low, whereas it transformed to aragonite if the concentration was more than 27.7 at%. This result is probably explained by a higher concentration of Mg in condensed aqueous droplets, formed by incongruent dissolution of ACMC. On the other hand, ACMC transformed to only calcite or Mg-calcite by heating process, in the concentration range of Mg investigated in this study.

1. Introduction

Recently attention has been paid to the existence and role of amorphous calcium carbonate (ACC) in biomineralization, as a counterpart of crystalline forms of calcium carbonate ($CaCO_3$) (*e.g.* Addadi *et al.*, 2003; Kim *et al.*, 2005). For instance, crustaceans definitely utilize ACC as their exoskeletons and gastroliths (*e.g.* Becker *et al.*, 2003; Sato *et al.*, 2011), because they recycle Ca^{2+} in their molt cycle and probably high solubility of ACC is attractive for the quick recovery of Ca^{2+} to the new skeletons (*e.g.* Zidar *et al.*, 1998; Becker *et al.*, 2005). ACC must be also suitable for plant cystolith, which acts as storage of calcium (Gal *et al.*, 2012). Moreover, recently it is proposed that ACC is formed as a precursor of crystalline calcium carbonates, calcite and aragonite, in some organisms (*e.g.* Weiss *et al.*, 2002; Politi *et al.*, 2004; Neues *et al.*, 2011). However, not only seawater but also extrapallial fluid contains more Mg^{2+} than Ca^{2+} (*e.g.*, Ries, 2010; Heinemann *et al.*, 2012). Therefore, investigation of ACC

and its crystallization process under Mg^{2+}-rich environments seem important to understand the biomineralization involving ACC. Hence, the synthetic experiments of ACC under Mg^{2+}-rich conditions have been conducted recently. Zhang *et al.* (2012) synthesized ACC with various Mg/Ca ratios and observed the period for crystallization and its polymorphs at room temperature, using FT-IR. When Mg/Ca ratio was 0.5, ACC was crystallized into mainly aragonite with a small amount of calcite after one day from the synthesis. When Mg/Ca ratio was 2, most ACC remained amorphous after three days but was completely crystallized after eight days from the synthesis. Most of ACC changed into aragonite when the Mg/Ca ratio was 1, and when Mg/Ca ratio was 3, only monohydrocalcite was formed. They suggested that these transformations occur by the dissolution- re-precipitation processes. Long *et al.* (2011) formed Mg-calcite from polymer-stabilized ACC by adding poly-acrylicacid (PAA) and dextran sodium salt (DexS). From (104) *d*-spacing in the XRD pattern, they suggested that the amount of magnesium in Mg-calcite depends on the Mg/Ca ratio of mother solution. The transformed Mg-calcite was observed by TEM and it was found that the Mg-calcite was aggregates of nano-crystallites.

As mentioned above, the effect of Mg on the transformation of ACC to crystalline forms seems valuable to investigate, for the understanding of biomineralization relevant to ACC. However, previous studies are not so many that the understanding of this issue is not sufficient. In this study, I synthesized Mg-containing ACC and crystallized them in a humid condition or by heating, then investigated the mineralogical and crystallographic features of crystalline $CaCO_3$ formed from ACC with the existence of magnesium.

2. Materials and Methods

2-1. Synthetic methods

The synthetic method was referred to Gal *et al.* (2010) with some modifications. As the control sample, 500 µl of 100 mM $CaCl_2$ and Na_2CO_3 (Wako pure chemical) were pre-cooled at 4 °C, then the two solutions were mixed. 500 µl of 100% EtOH was added into the mixed solution to stop the reaction, and centrifuged at 5000 rpm. The precipitated ACC were washed by EtOH for three times and dried using an aspirator. Hereafter, the word “control” indicates pure ACC. For Mg-containing amorphous calcium-magnesium carbonate (ACMC) sample, 1 mM, 5 mM, 10 mM, 50 mM and 100 mM $MgCl_2$ (Wako pure chemical) was dissolved into $CaCl_2$ water solution. Hence, the Mg / Ca ratio in mixed solution is 0.01, 0.05, 0.1, 0.5 and 1. The samples after drying were kept in closed container and stored them in freezer. To induce crystallization, these ACC and ACMC samples were set in a 24-well microplate (ASONE) with ultrapure water (4 ml in each well) at 60 °C in an oven to realize almost 100% humidity condition. The samples were stored for one week at 60 °C in an oven because samples stored for 2 and 3 weeks are nearly identical to those for one week in powdered XRD analyses. Fig. 1 shows the scheme of well plate.

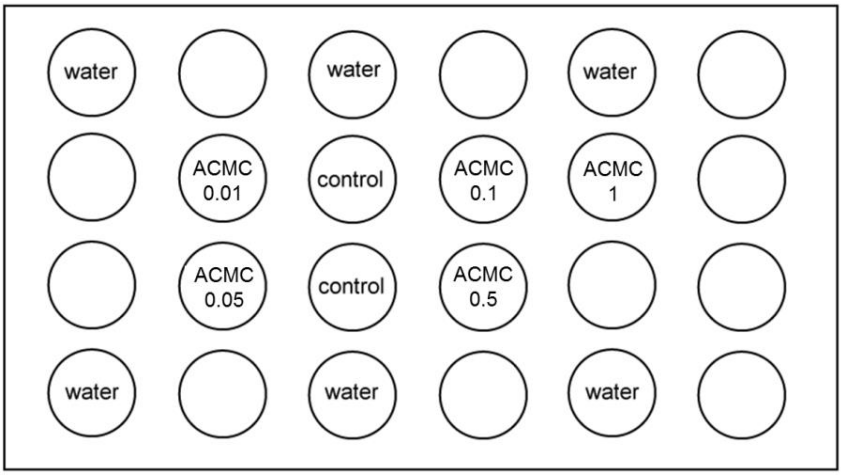

Fig. 1. Scheme of the array for ACC crystallization. 0.01 to 1 of ACMC shows the $MgCl_2/CaCl_2$ ratio in former solution.

2-2. Analyses

To confirm that the samples synthesized are ACC and to determine the polymorphs after crystallization, they were analyzed by powdered XRD (Rigaku, Ultima$^+$ diffractometer with graphite-monochromated CuKα radiation and RINT 2000 analytical system) with randomly-oriented specimens. To investigate the morphological and crystallographic features, the samples were observed by SEM (Hitachi, S-4500) and TEM (JEOL, JEM-2010). The compositions of the samples were analyzed using energy-dispersed X-ray spectrometers (EDS) equipped to the SEM and TEM. Specimens for TEM were prepared by a focused-ion-beam (FIB) instrument (Hitachi, FB-2100) or just by dispersing the samples on microgrids for TEM. Control and all ACMC samples were analyzed by TG-DTA. The heating rate is 10 °C /min. In addition, two high-Mg ACC samples (50 mM and 100 mM $MgCl_2$ in solution) were heated at 400 °C and 500 °C using TG-DTA and analyzed by XRD, to know the crystalline phases.

3. Results

3-1. Characterization of ACC

XRD analyses

First, the samples were analyzed using powdered XRD to confirm that all samples are ACC just after synthesis (Fig. 2). As a result, all samples (control and $MgCl_2/CaCl_2$ = 0.01 to 1 in solution) show the completely amorphous character. The position of the broad halo peak around $2\theta = 30^o$ are observed in all samples, which is shifted slightly (about 0.2^o to 0.3^o in 2θ) as the content of Mg in the solution increases.

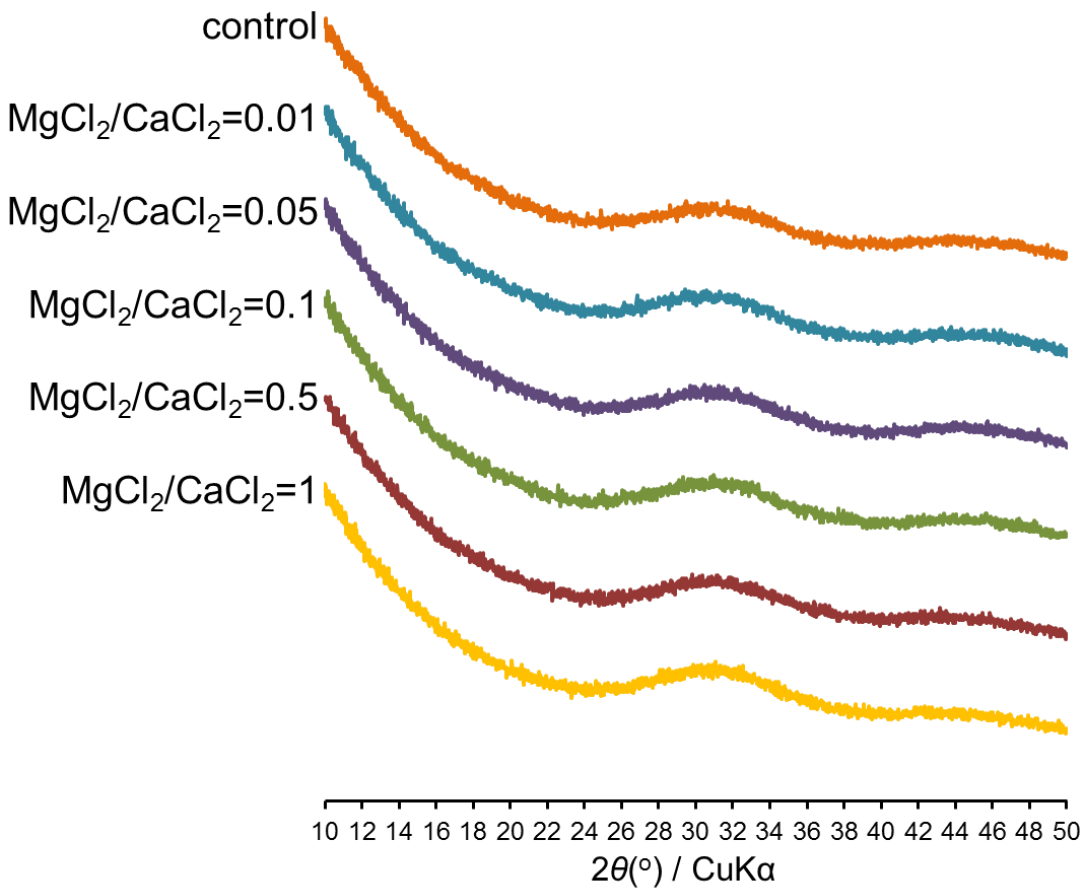

Fig. 2. XRD patterns from the ACC samples just after desiccation. The $MgCl_2/CaCl_2$ value means that in the solution from which ACC precipitated.

SEM-EDS analysis of ACMC

The control and ACMC samples were observed using SEM and their constituent elements were analyzed using SEM-EDS. The appearances of all samples are small spherules, as reported in many previous studies (Fig. 3). The spherules are 50 nm to 150 nm in diameter. The samples were pressed to tablets with flat surfaces, and analyzed quantitatively by SEM-EDS (Fig. 4). Averaged values of Mg content from ten analyzing points for each sample are shown in Table 1 and Fig. 5.

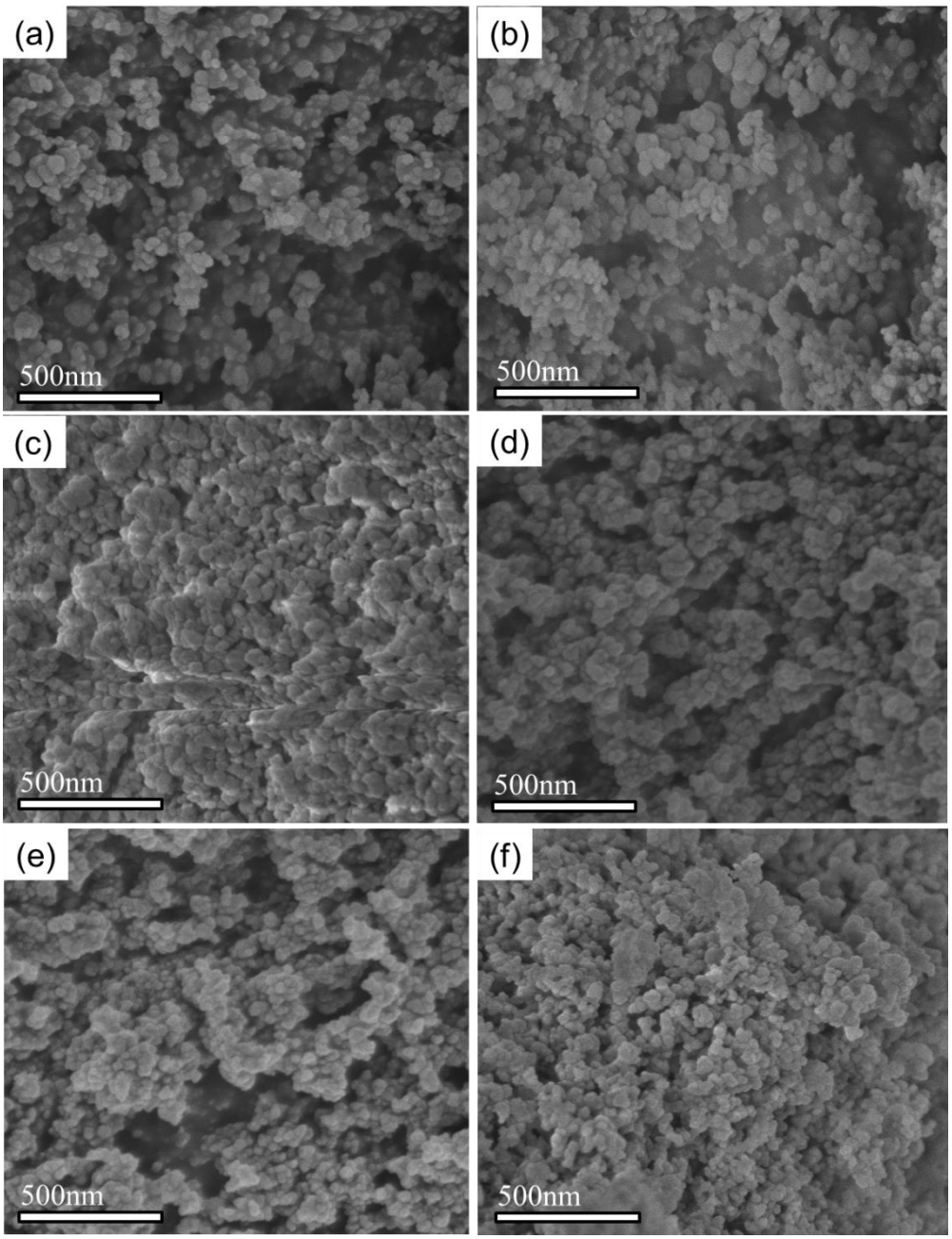

Fig. 3. SEM images of ACMC. (a) Control (b) $MgCl_2/CaCl_2$ = 0.01. (c) $MgCl_2/CaCl_2$ = 0.05. (d) $MgCl_2/CaCl_2$ = 0. 1. (e) $MgCl_2/CaCl_2$ = 0.5. (f) $MgCl_2/CaCl_2$ = 1.

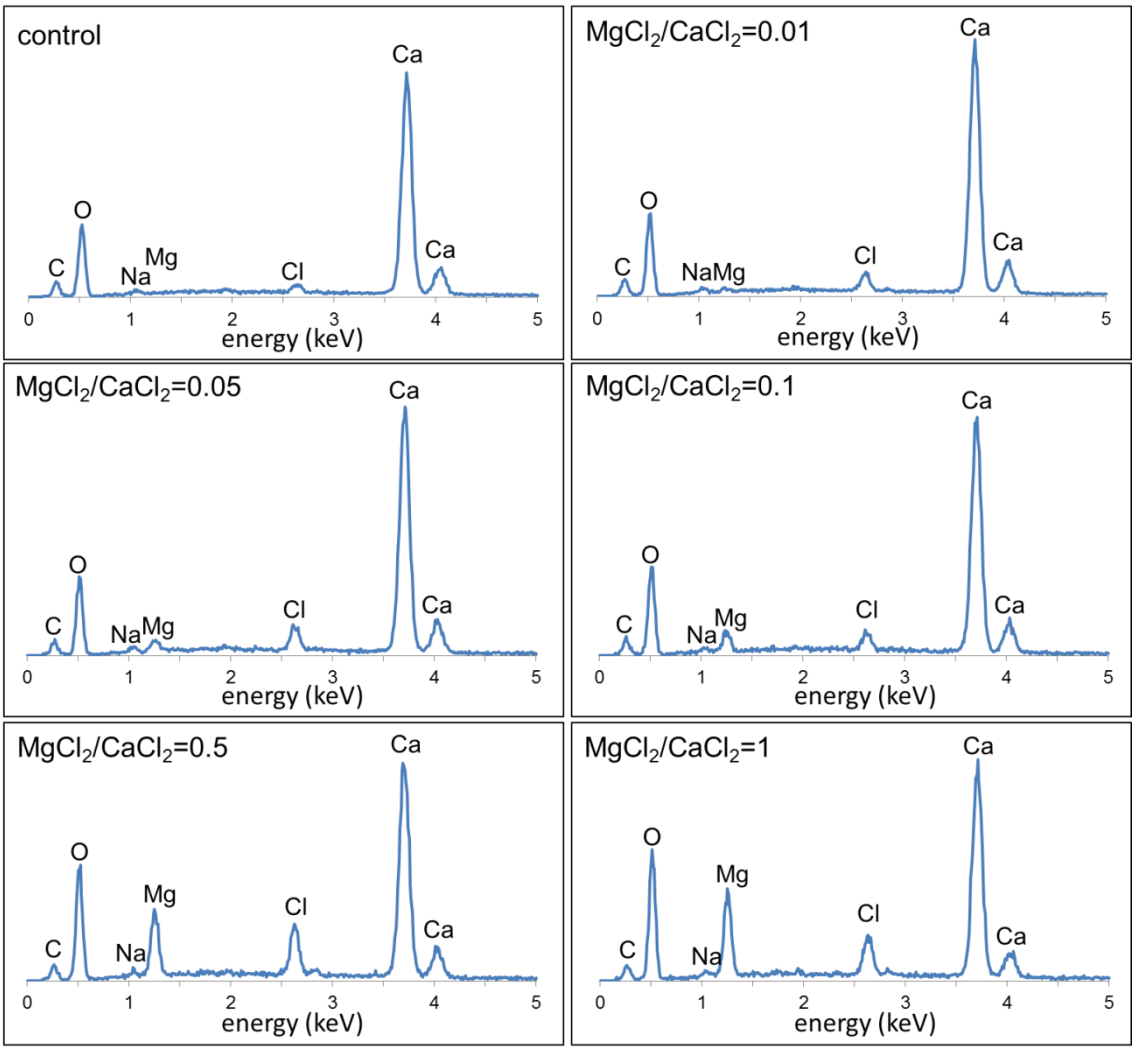

Fig. 4. SEM-EDS spectrum from ACMC. (a) ACC. (b) $MgCl_2/CaCl_2$ =0.01. (c) $MgCl_2/CaCl_2$ =0.05. (d) $MgCl_2/CaCl_2$ =0.1. (e) $MgCl_2/CaCl_2$ =0.5. (f) $MgCl_2/CaCl_2$ =1. Pt and Pd are from Pt-Pd coating.

Table 1. Mg content in ACMC from SEM-EDS quantitative analyses. SD: standard deviation.

$MgCl_2/CaCl_2$ ratio	control	0.01	0.05	0.1	0.5	1
Mg (at%)	0	1.43	6.24	12.02	27.71	37.52
SD	0	1.01	0.53	0.94	2.21	1.04

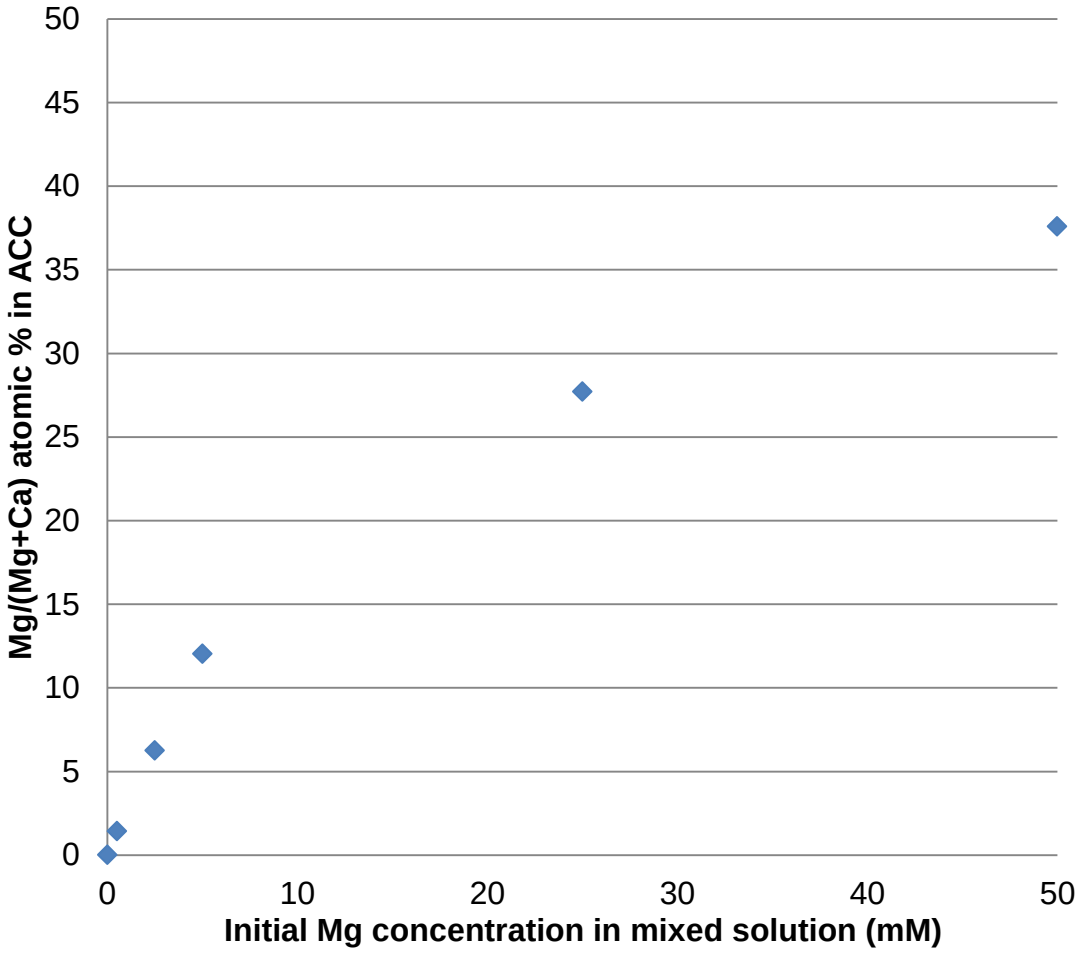

Fig. 5. Amount of Mg included in control ACC and ACMC. The data are described at Table 1.

TG-DTA analyses

The samples were analyzed using TG-DTA to investigate the crystallization temperature of ACC. First of all, control ACC crystallized at between 330 °C and 350 °C (Fig. 6a). In contrast, the ACMC samples were crystallized at a considerably higher temperature, even the sample with 1.4 at% Mg content (Fig. 6b-e). Previous studies (Kojima *et al.* 1993; Koga and Yamane, 2008) reported that Mg-free ACC crystallizes below 350 °C. The crystallization temperature is highest (385 °C to 390 °C) for ACMC samples with 6.2 at% (Fig. 6c). Mg is thought to delay the crystallization of ACC in water (Tao *et al.*, 2009) or humid conditions (Loste *et al.*, 2003). From these results, magnesium is regarded as a stabilizer of ACC in the heat treatment. In addition, Fig. 6c and d shows weight loss around ACC-crystal transition.

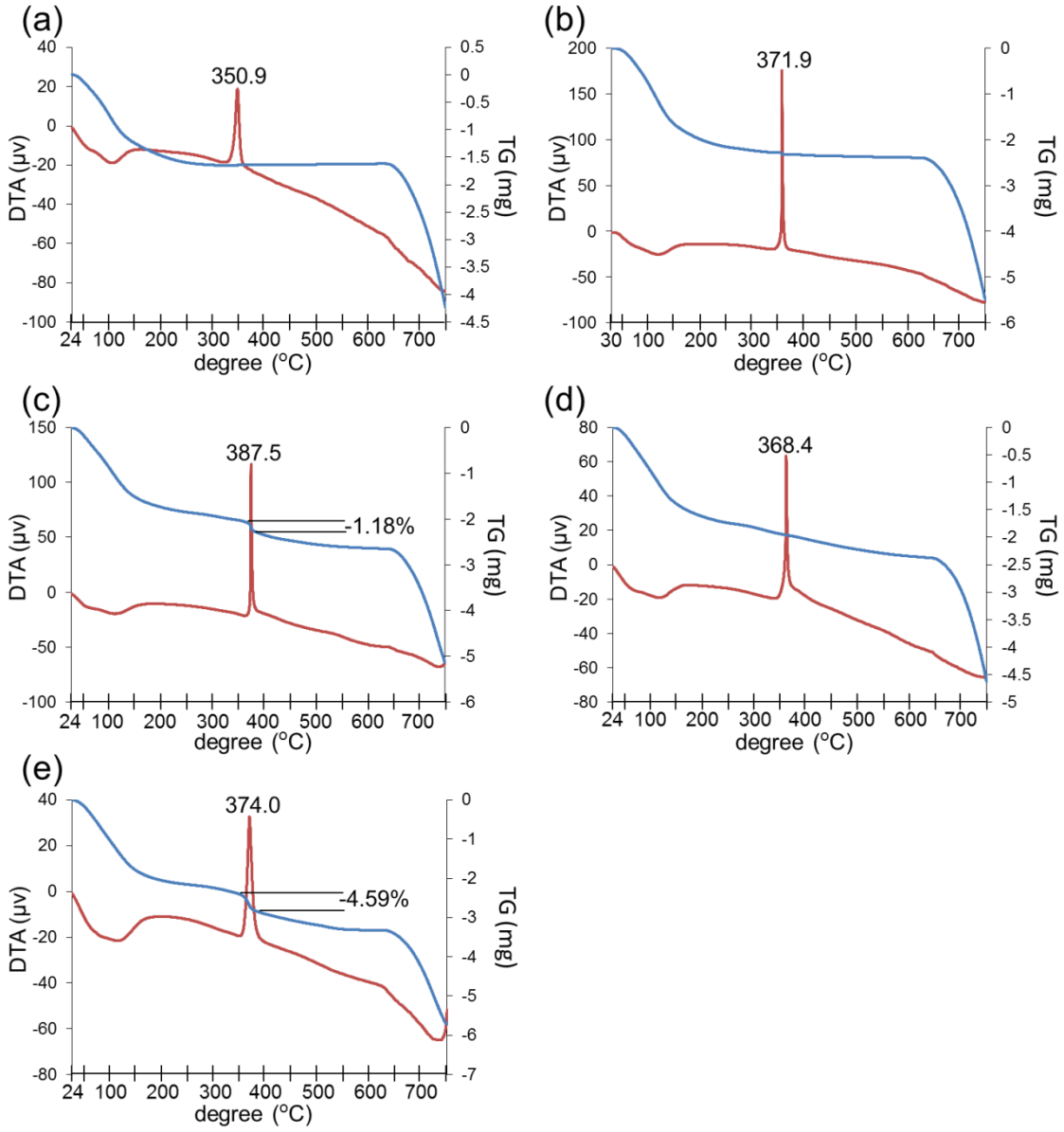

Fig. 6. TG-DTA analyses of ACC. (a) Control. (b) ACMC with 1.4 at% of Mg. (c) ACMC with 6.2 at%. (d) ACMC with 12.0 at%. (e) ACMC with 27.7 at %.

TEM observations

The control and ACMC samples with 27.7 at% were observed by TEM with the thin specimens prepared by FIB. Control ACC shows a porous or network-like aggregation of the spherules (Fig. 7). From magnified observation, most of the spherules are 30 to 50 nm, in accordant with the SEM observation (Fig. 3). From the SAED pattern, the sample was confirmed to be completely amorphous (Fig. 7d). ACMC with 27.7 at% was also observed similarly. This sample also shows a network-like aggregation of the spherules, like the control ACC (Fig. 8). The SAED pattern indicated that this sample is also amorphous.

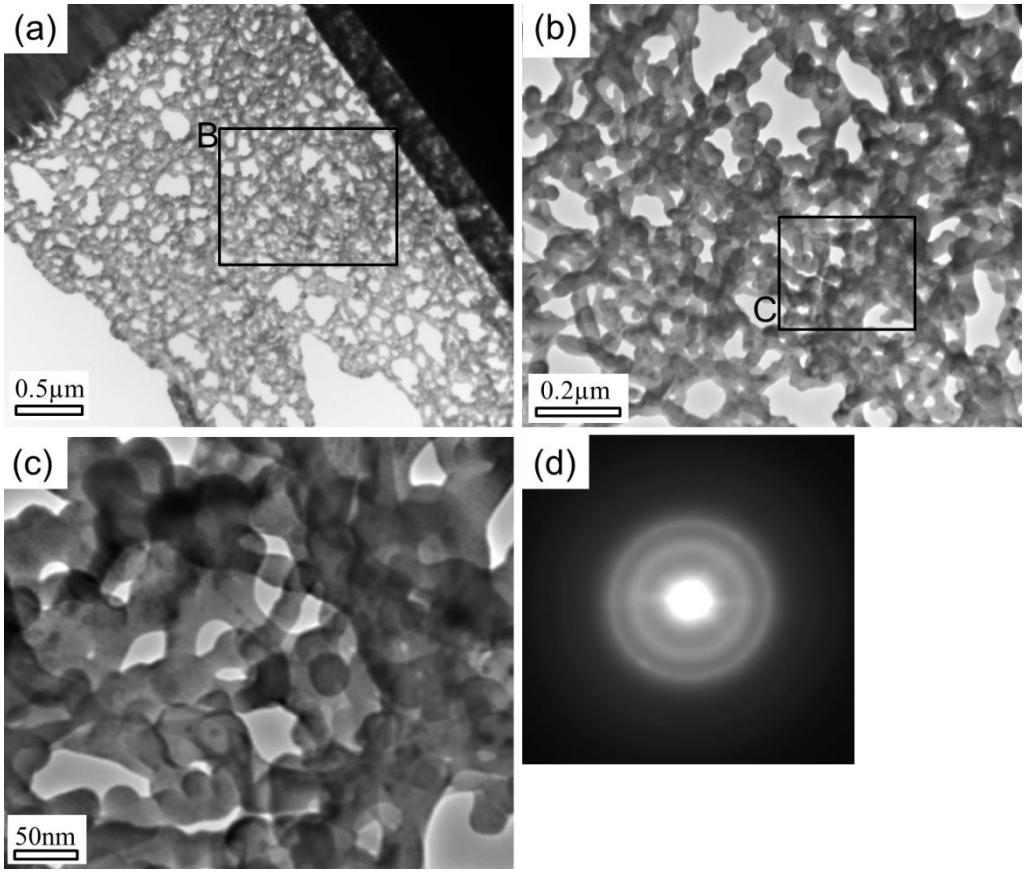

Fig. 7. TEM observation of control ACC. (a) Low-magnified image. (b) Higher-magnified image of B in (a). The spherules are aggregated as a network-like structure. (c) Magnified image of C in (b). The spherule size is around 50 nm. (d) SAED pattern from the area (c).

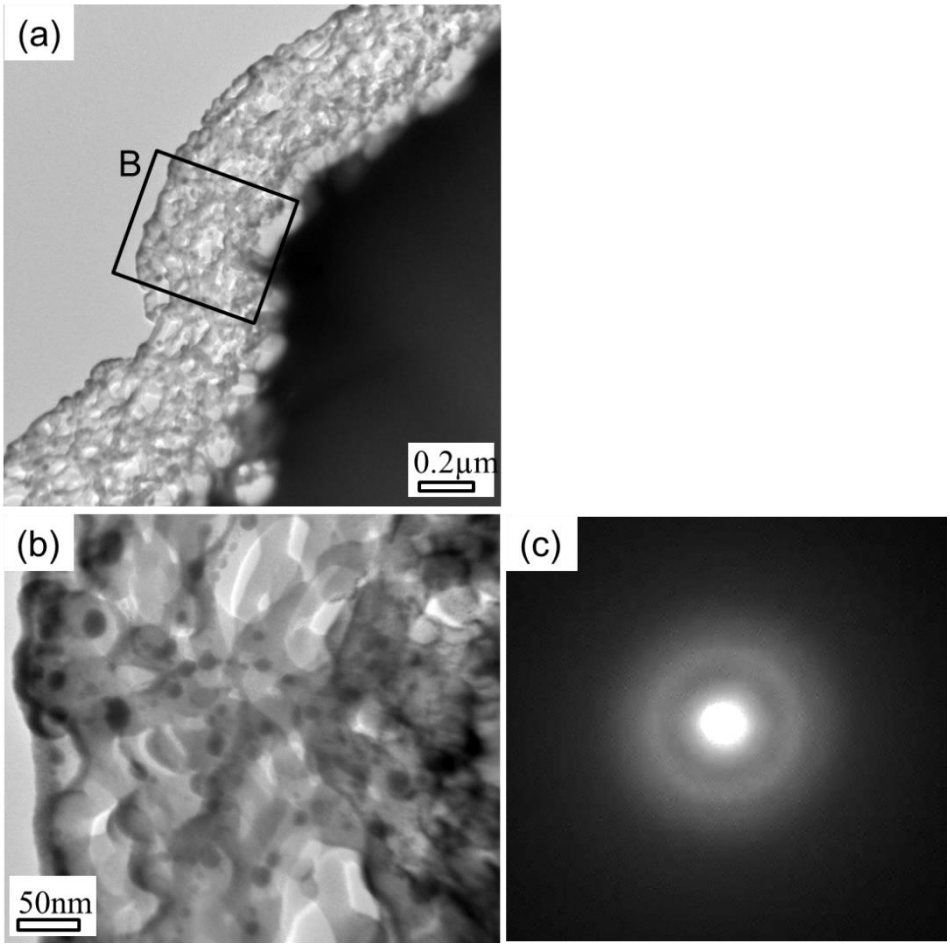

Fig. 8. TEM observation of ACMC with 27.7 at%. (a) Low-magnified image. (b) Magnified image of B in (a). (c) SAED pattern from the area in (b)

3-2 Characterization of crystallized ACC

XRD analyses

XRD patterns from the samples kept in the humid condition at 60 °C for a week are shown in Fig. 9. Control ACC and ACMC samples with 1.4 at% transformed to calcite and vaterite. For ACMC samples with 6.2 at% and 12.0 at%, the aragonite peaks appeared instead of the vaterite peaks. Because the calcite peaks clearly shift to higher angles, the crystals are considered to be magnesium-calcite (Mg-calcite). ACMC samples with 27.7 at% and 37.5 at% formed only aragonite. It is possible to assign one small peak indicated with "m" in the figure to magnesite ($MgCO_3$), but the peak is also possible assign to aragonite 121 peak. This result is nearly consistent with that in Zhang *et al.* (2012).

To investigate the crystalline phase transformed from ACMC by heating, ACMC samples with 27.7 at% were heated at 400 °C and 500 °C, and analyzed using XRD. The heated sample transformed to calcite although the sample kept under the humid condition transformed to aragonite (Fig. 10). In addition, the peaks of the 400 °C sample are broader than those of 500 °C sample and shift to higher degrees. Hence, 400 °C and 500 °C sample peaks seem to be assigned to Mg-calcite and pure calcite, respectively. 500 °C sample also shows a broad peak around 43^o, which can be assigned to periclase (MgO). These results indicate that fine Mg-calcite crystals formed at 400 °C were grown to large crystals at 500 °C, segregating the Mg component from the crystals.

Magnesium contents were calculated from the peak position of the 202 reflection (around 43.2^o for pure calcite). The correlation between the peak position and Mg content in calcite was calculated from ICSD and JCPDS data (Fig. 11). $CaCO_3$ (JCPDS 47-1743), $Ca_{0.94}Mg_{0.06}CO_3$ (JCPDS 89-1305), $Ca_{0.936}Mg_{0.064}CO_3$ (JCPDS 86-2335),

$Ca_{0.9}Mg_{0.1}CO_3$ (ICSD 10405), $Ca_{0.871}Mg_{0.129}CO_3$ (JCPDS 86-2336), $Ca_{0.864}Mg_{0.136}CO_3$ (JCPDS 43-0697) were used for the calculation. From Fig. 11, the correlation is expressed as y = -0.0018x + 2.0916, where x, y are Mg content (at%) and d_{202} value (Å), respectively. The Mg contents in the Mg-calcite estimated from the d_{202} values are listed in Table 2 and Fig. 12. The Mg contents in the control and ACMC samples with 1.4 at%, 6.2 at% and 12.0 at% were calculated from the samples crystallized under the humid condition (shown in Fig. 8), and those in Mg-calcite formed from ACMC samples with 27.7 at% and 37.5 at% by annealing at 400 °C and 500 °C were estimated.

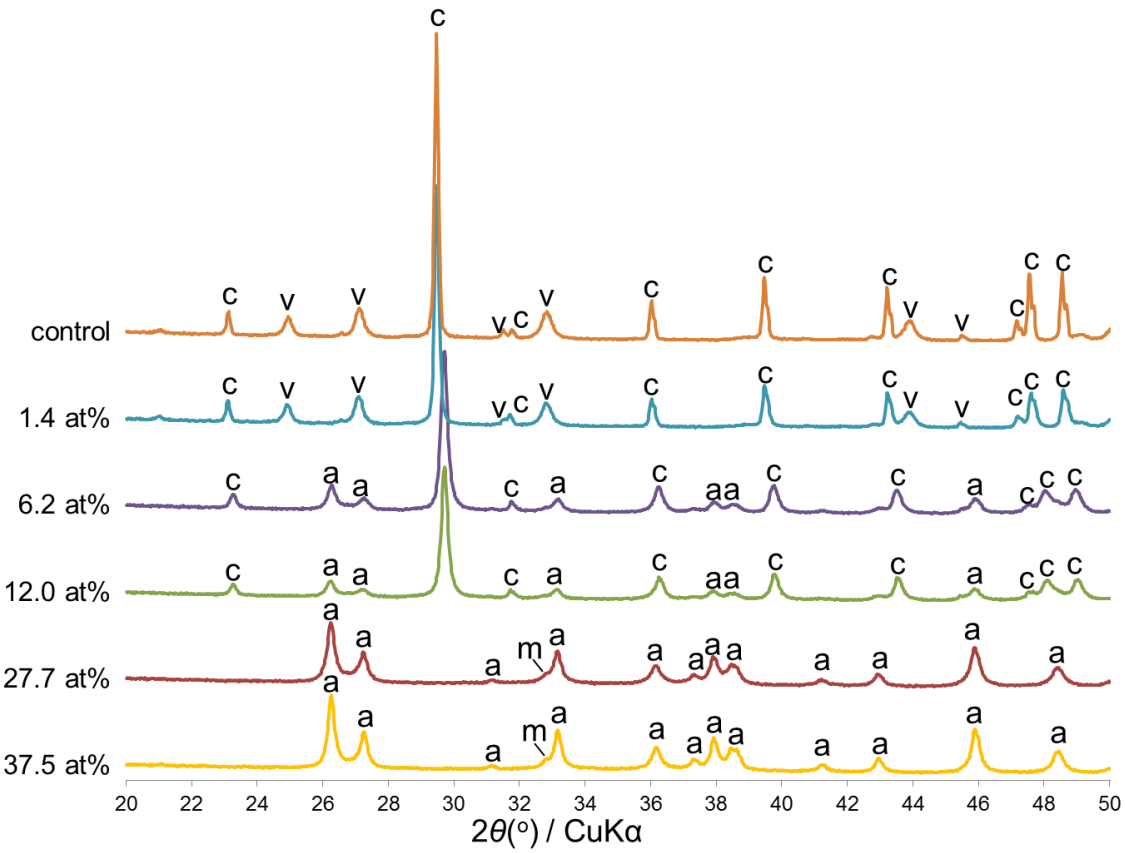

Fig. 9. XRD patterns from the samples under the humid condition for one week. The "c" peaks are assigned to calcite or Mg-calcite, "v" peaks to vaterite, "a" peaks to aragonite. "m" peak is possible to assign to $MgCO_3$.

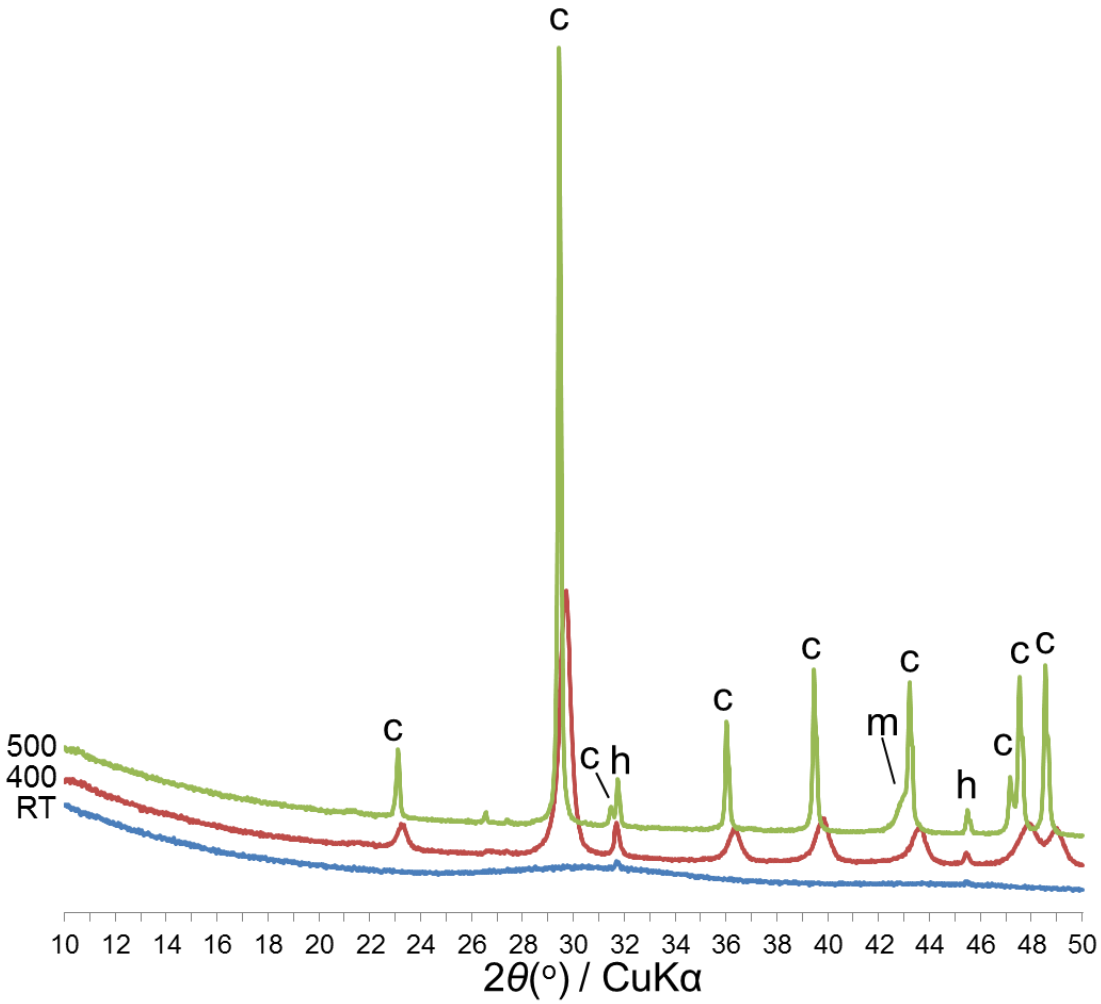

Fig. 10. XRD patterns of room temperature (RT), 400 °C heat (400) and 500 °C heat (500) sample of ACMC with 27.7 at%. The peaks indicate with “c” are assigned to calcite, “h” to halite (NaCl). “m” is possible to be assigned to periclase (MgO).

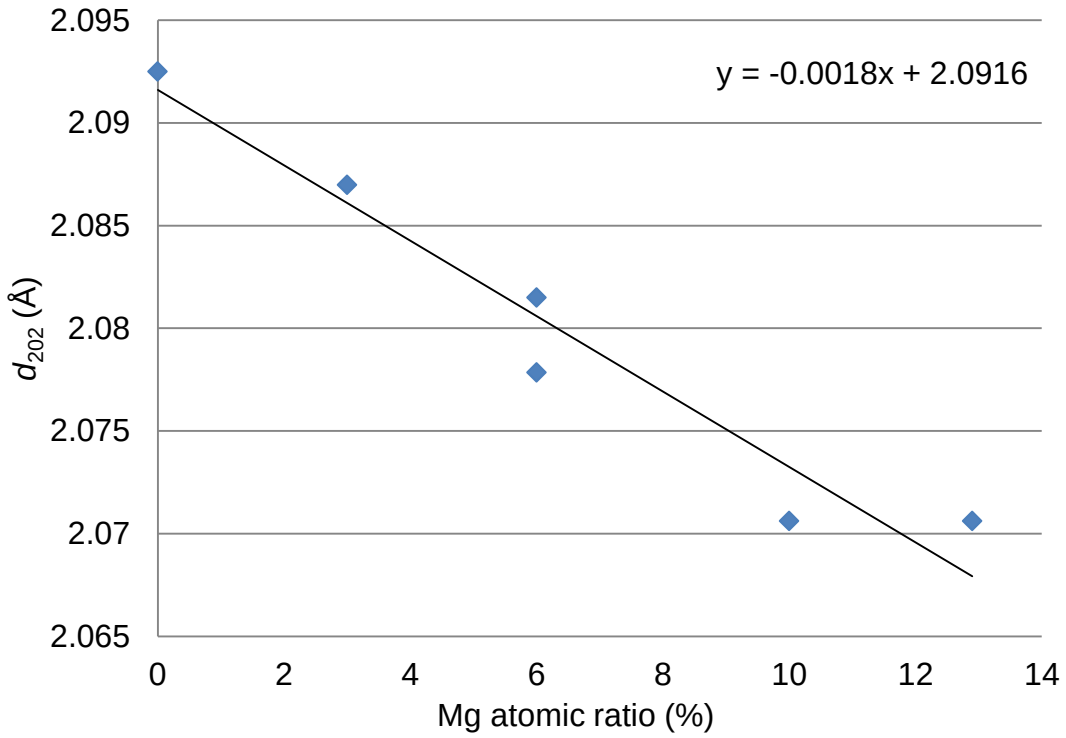

Fig. 11. Correlation between the d_{202} and Mg contents for Mg-calcite. The data are obtained from ICPDS 47-1743, ICPDS 89-1305, ICPDS 86-2335, ICSD 10405, ICPDS 86-2336, and ICPDS 43-0697.

Table 2. Mg contents in crystallized ACC which is calculated from d_{202} measured by XRD using the result in Fig. 11. 400 and 500 indicate the heating temperature, respectively.

	control	1.4 at%	6.2 at%	12.0 at%	27.7 at% (400)	37.5 at% (400)	27.7 at% (500)	37.5 at% (500)
2θ (°)	43.20	43.22	43.51	43.53	43.61	43.63	43.20	43.20
d_{202} (Å)	2.09	2.09	2.08	2.08	2.07	2.07	2.09	2.09
Mg (at%)	0.00	0.01	7.39	7.89	9.90	10.41	0.00	0.00

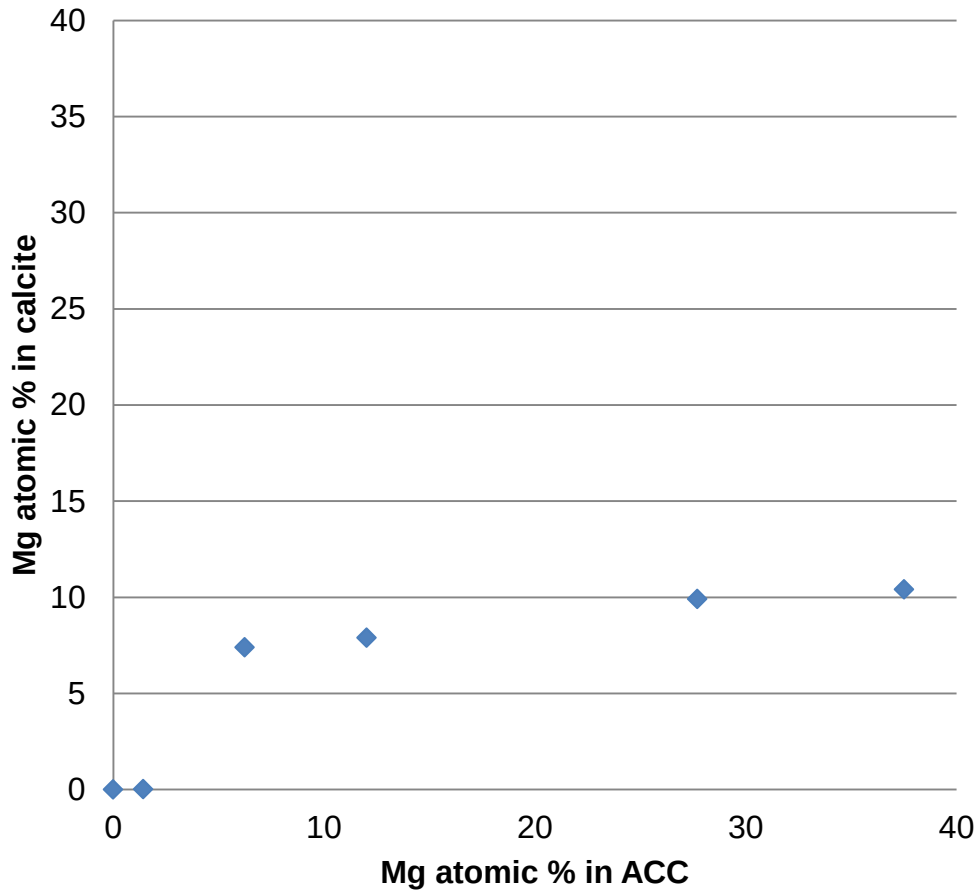

Fig. 12. Amount of Mg included in Mg-calcite. The data are described at Table 2. 400 °C heated samples are plotted for ACMC with 27.7 at% and 37.5 at%.

SEM observation

Morphologies of the samples crystallized in the humid condition observed by SEM are shown in Figs. 13-15. The samples transformed from control ACC, ACMC with 1.4 at%, 6.2 at%, and 12.0 at% (Figs. 13 and 14) probably consist of calcite and Mg-calcite from XRD analyses. The samples transformed from ACMC with 27.7 at% and 37.5 at%, which should consist of aragonite based on XRD analysis, are shown in Fig. 15.

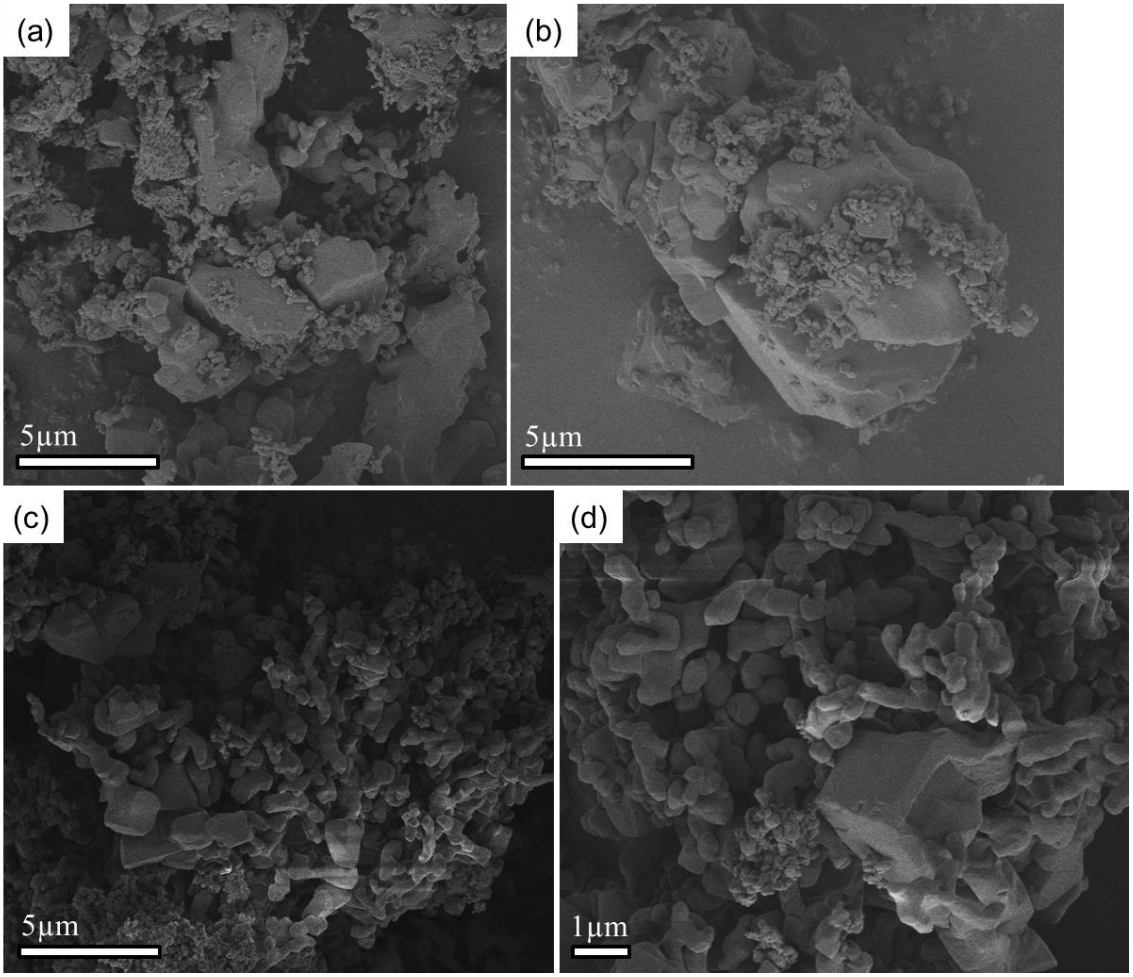

Fig. 13. SEM images of the crystallized samples from (a, b) control ACC and (c, d) ACMC with 1.4 at%.

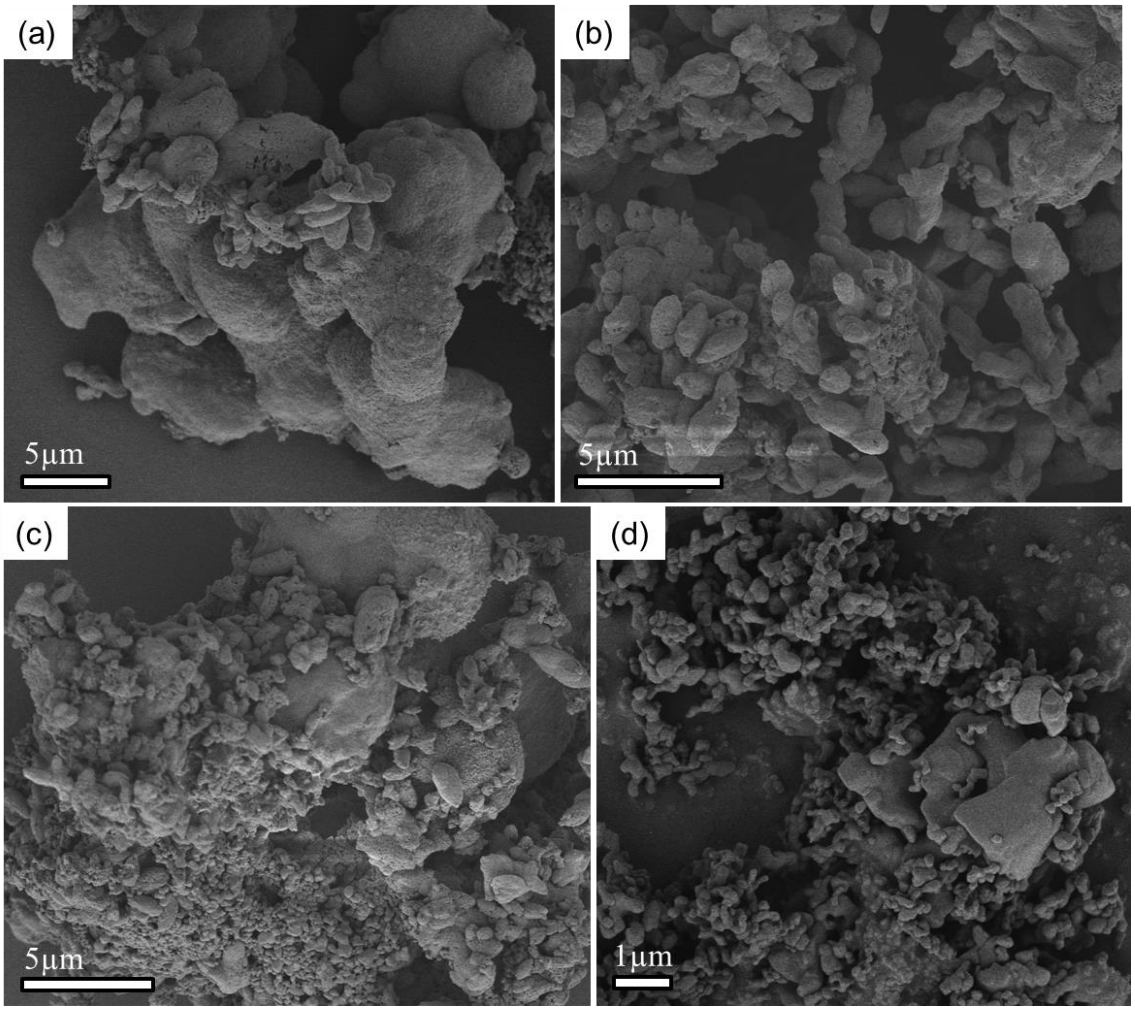

Fig. 14. SEM images of the crystallized samples from (a, b) ACMC with 6.2 at% and (c, d) ACMC with 12.0 at%.

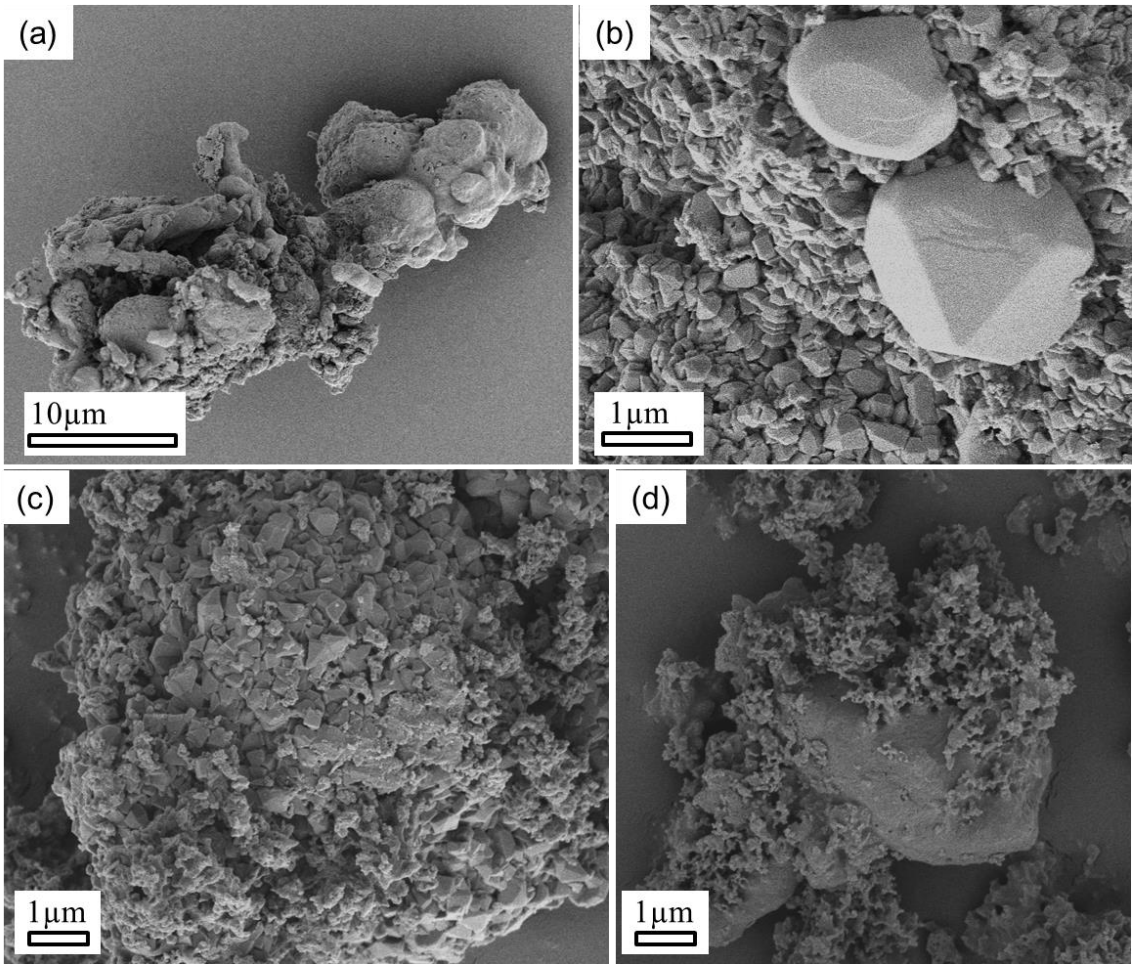

Fig. 15. SEM images of the crystallized samples from (a, b) ACMC with 27.7 at% and (c, d) ACMC with 37.5 at%.

TEM observation of selected samples

The sample crystallized from ACMC sample with 27.7 at% in the humid condition was analyzed in TEM (Fig. 16). Relatively large and euhedral crystals were found in the sample (Fig. 16b). SAED patterns indicate that all of these crystals are aragonite (Fig. 16d), in consistent with the result of XRD analysis. Besides, very fine crystals which form Debye-Scherrer rings in the SAED pattern were observed (Fig. 16c, e) between the large aragonite crystals. They were identified as magnesite ($MgCO_3$) from the SAED pattern (Fig. 16e).

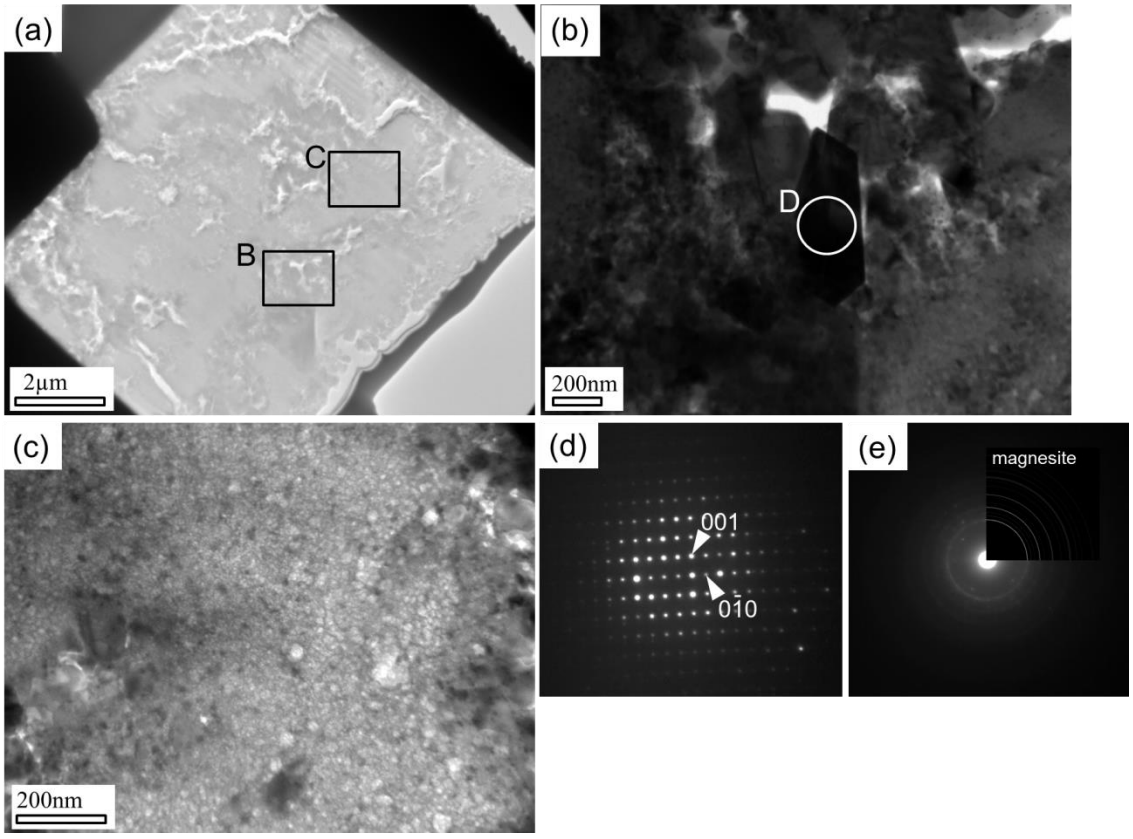

Fig. 16. TEM observation of the sample crystallized from ACMC sample with 27.7 at% in the humid condition. (a) Low-magnified image. (b) Magnified image of B in (a). (c) Magnified image of C in (a). (d) SAED pattern from D in (b). (e) SAED pattern from (c) area. Inset at the top-right shows the theoretical Debye-Scherrer pattern of magnesite.

On the other hand, the samples from the same ACMC with 27.7 at% but crystallized by heating at 400 °C and 500 °C were observed to investigate the behavior of magnesium. The sample heated at 400 °C shows very fine particles of calcite (Fig. 17a, b). From TEM-EDS analyses, actually they are considered Mg-calcite (Fig. 17c). This is consistent with the result of XRD analysis. The sample heated at 500 °C shows two types of crystals; large calcite crystals and small (around 40 nm) crystals adhered to the calcite crystals (Fig. 18a, c). These microcrystals contain Mg and O mainly (Fig. 18b, d). From the peak position of XRD and this EDS spectrum, these small crystals are suggested to be periclase (MgO). Thus, Mg was segregated from Mg-calcite and form magnesium oxide at 500 °C.

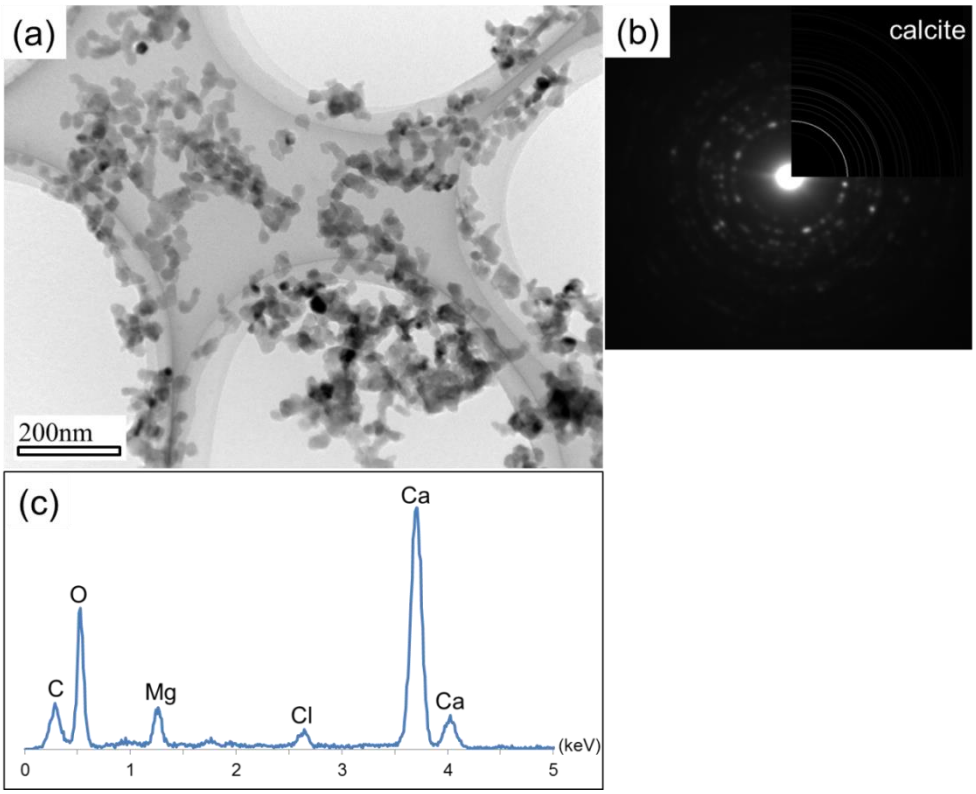

Fig. 17. (a) TEM image of the dispersed ACMC sample with 27.7 at% heated at 400 °C. (b) SAED pattern from the particles. Inset at the top-right shows the theoretical Debye-Scherrer pattern of calcite. (c) TEM-EDS spectrum from ACMC sample with 27.7 at% heated at 400 °C.

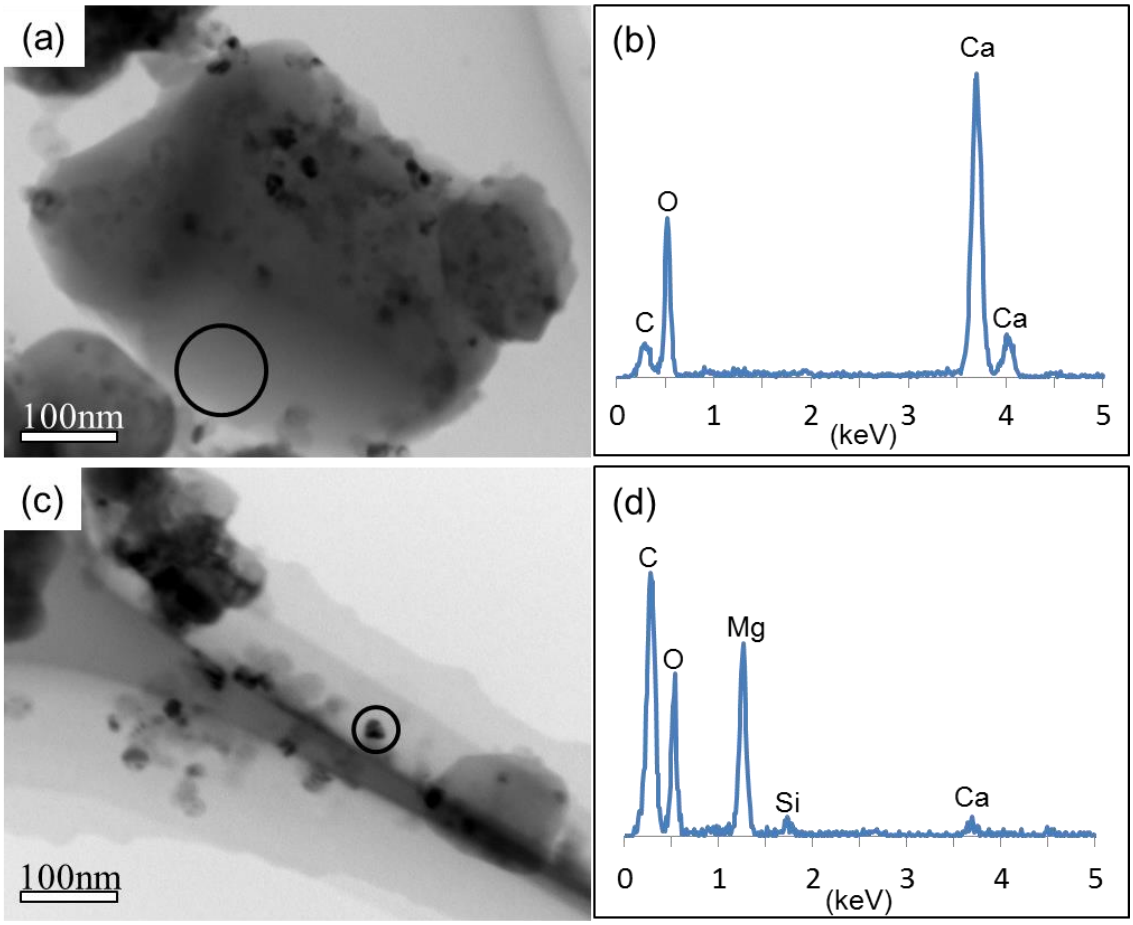

Fig. 18. TEM results for the ACMC sample with 27.7 at% crystallized by heating at 500 °C. (a) TEM image. (b) TEM-EDS spectrum from the black circle in (a). (c) TEM image. (d) TEM-EDS spectrum from the black circle in (c).

4. Discussion

Formation of ACMC

Mg content in ACMC determined by SEM-EDS analysis indicates that Mg was incorporated to the precipitated ACC almost with the same Mg content as that in solution, if the Mg content was low in the solution. However, as the Mg content in the solution increased, the amount of Mg content in ACMC was definitely lower than that in solution (Table 1). This result suggests that although the structure is amorphous and precipitation occurs quickly with a very far-equilibrium (supersaturated) condition, the amount of Mg incorporated in ACC as solid solution is still limited. On the other hand, in spite of considerable amounts of Mg incorporated in ACMC, the morphology of ACMC is very similar, regardless of the Mg content (Fig. 3). The TG curves in Fig. 6 also suggest that the amount of water in ACMC, which is estimated by the loss of the weight until around 200 °C, is also similar among the five ACMC samples.

Crystallization of ACMC in the humid condition

The result in Fig. 9 suggests that the crystalline phase from ACMC strongly depends on the content of Mg. Aragonite starts to form from ACMC with 6.2 at% of Mg and only aragonite was formed with 27.7 at% of Mg in ACMC (Table 1). Generally if we try to precipitate aragonite instead of calcite in solution, Mg should be about 10 times more than Ca in the solution (*e.g.* Ohde and Kitano, 1978). The amount of Mg necessary to form aragonite from ACC is far smaller than that in solution. However, this result may not be so surprising, considering the environment of the reaction in the humid condition. Because ACMC is porous aggregates of fine particles as shown in the TEM images (Fig. 7), vapor evaporated in the microplate is probably condensed as droplets inside the pores in ACMC and such aqueous droplets will be the media for the

"dissolution-precipitation" reaction. If we consider the higher solubility of $MgCO_3$ than $CaCO_3$, $MgCO_3$ component in ACMC may dissolve preferentially from ACMC to the aqueous droplets. As a result, the composition of the droplets can be considerably Mg-rich compared to that in ACMC. Consequently, aragonite precipitates when the droplet solution is oversaturated with respect to $CaCO_3$, by a large Mg content in the droplet. Formation of $MgCO_3$ as found in the TEM experiment (Fig. 16) may be a product at a late stage or formed by the desiccation after the reaction.

Crystallization of ACMC by heating

On the other hand, only calcite or Mg-calcite was formed from ACMC by heating in the TG-DTA instrument, in spite of the high Mg content (27.7 and 37.5 at%). In this case, the crystallization temperature was increased by ~ 30 °C compared to pure ACC (Fig. 5c). However, the degree of the temperature increase does not depend on the amount of Mg in ACMC. The explanation for this irrelevance between Mg concentration and the crystallization temperature is not clear at present.

XRD patterns in Fig. 10 indicate that at 400 °C, ACMC transforms to Mg-calcite. In this case, the peaks of Mg-calcite are very broad, which corresponds to very small grain size as observed in the TEM image (Fig. 17). This small grain size is comparable with that of ACMC observed in the SEM image (Fig. 3). Probably ACMC crystallized into Mg-calcite without grain growth or sintering, at this temperature and heating rate (10 °C/min.). However, the chemical composition of the Mg-calcite is estimated about 12.0 at% from the peak shift in the XRD pattern (Fig. 10, Table 2). This amount is far smaller than those of the original ACMC (27.7 and 37.5 at%). Because no other peaks than those of Mg-calcite were observed in the XRD pattern, the rest of $MgCO_3$ component may be still in the amorphous state. At 500 °C, grain size of the crystal was

increased considerably as indicated by the sharp profile in the XRD pattern (Fig. 10) and TEM images (Fig. 18), probably intense diffusion of elements at this temperature. At the same time, Mg was segregated from Mg-calcite to form relatively pure calcite and MgO.

5. Conclusions

The crystallization process of Mg-containing amorphous calcium carbonate (ACMC) is considerably different from that of pure ACC. In particular, it can transform to aragonite in humid conditions, with a certain amount of Mg in ACMC. This phenomenon is probably explained by a small ratio of solution/solid in the condition and preferential dissolution of $MgCO_3$ component into the solution, which results in a higher Mg content in the solution to enhance aragonite precipitation. The crystallization by heating in a dry condition generates only calcite or Mg-calcite, irrespective of Mg concentration in ACMC. The crystallization temperature was increased compared to that for pure ACC but its dependence on the Mg concentration was not clearly observed.

References

Addadi, L., Raz, S., Weiner, S.: Taking advantage of disorder: amorphous calcium carbonate and its roles in biomineralization. *Advanced Materials*, **15** (12), 959-970, 2003

Becker, A., Bismayer, U., Epple, M., Fabritius, H., Hasse, B., Shi, J., Ziegler, A.: Structural characterisation of X-ray amorphous calcium carbonate (ACC) in sternal deposits of the crustacea *Porcellio scaber*. *Journal of the Chemical Society, Dalton transactions*, **4**, 551-555, 2003

Becker, A., Ziegler, A., Epple, M.: The mineral phase in the cuticles of two species of Crustacea consists of magnesium calcite, amorphous calcium carbonate, and amorphous calcium phosphate. *Journal of the Chemical Society, Dalton transactions*, **10**, 1824-1820, 2005

Gal, A., Hirsch, A., Siegel, S., Li, C., Aichmayer, B., Politi, Y., Fratzl, P., Weiner, S., Addadi, L.: Plant cystoliths: a complex functional biocomposite of four distinct silica and amorphous calcium carbonate phases. *Chemistry-A European Journal*, **18**, 10262-10270, 2012

Gal, A., Weiner, S., Addadi, L.: The stabilizing effect of silicate on biogenic and synthetic amorphous calcium carbonate. *Journal of American Chemical Society*, **132**, 13208-13211, 2010

Heinemann, A., Fietzke, J., Melzner, F., Böhm, F., Thomsen, J., Garbe-Schönberg, D., Eisenhauer, A.: Conditions of *Mytilus edulis* extracellular body fluids and shell composition in a pH-treatment experiment: acid-base status, trace elements and δ^{11}B. *Geochemistry Geophysics Geosystems*, **13** (1), 1-17, 2012

Kim, I. W., Robertson, R. E., Zand, R.: Effects of some nonionic polymeric additives on

the crystallization of calcium carbonate. *Crystal Growth & Design*, **5** (2), 513-522, 2005

Koga, N. and Yamane, Y.: Thermal behaviors of amorphous calcium carbonates prepared in aqueous and ethanol media. *Journal of Thermal Analysis and Calorimetry*, **94** (2), 379-387, 2008

Long, X., Ma, Y., Qi, L.: *In vitro* synthesis of high Mg calcite under ambient conditions and its implication for biomineralization process. *Crystal Growth & Design*, **11**, 2866-2873, 2011

Loste, E., Wilson, R. M., Seshadri, R., Meldrum, F. C.: The role of magnesium in stabilizing amorphous calcium carbonate and controlling calcite morphologies. *Journal of Crystal Growth*, **254**, 206-218, 2003

Neues, F., Hild, S., Epple, M., Marti, O., Ziegler, A.: Amorphous and crystalline calcium carbonate distribution in the tergite cuticle of moulting *Porcellio scaber* (Isopoda, Crustacea). *Journal of Structural Biology*, **175**, 10-20, 2011

Ohde, S. and Kitano, Y.: Synthesis of protodolomite from aqueous solution at normal temperature and pressure. *Geochemical Journal*, **12**, 115-119, 1978

Politi, Y., Arad, T., Klein, E., Weiner, S., Addadi, L.: Sea urchin spine calcite forms via a transient amorphous calcium carbonate phase. *Science*, **306**, 1161-1164, 2004

Ries, G. B.: Review: geological and experimental evidence for secular variation in seawater Mg/Ca (calcite-aragonite seas) and its effects on marine biological calcification. *Biogeosciences*, **7**, 2795-2849, 2010

Sato, A., Nagasaka, S., Furihata, K., Nagata, S., Arai, I., Saruwatari, K., Kogure, T., Sakuda, S., Nagasawa, H.: Glycolytic intermediates induce amorphous calcium carbonate formation in crustaceans. *Nature Chemical Biology*, **7**, 197-199, 2011

Tao, J., Zhou, D., Zhang, Z., Xu, X., Tang, R.: Magnesium-aspartate-based crystallization switch inspired from shell molt of crustacean. *Proceedings of the National Academy of Sciences*, **106** (52), 22096-22101, 2009

Weiss, I. M., Tuross, N., addadi, L., Weiner, S.: Mollusc larval shell formation: amorphous calcium carbonate is a precursor phase for aragonite. *Journal of experimental zoology*, **293**, 478-491, 2002

Zhang, Z., Xie, Y., Xu, X., Pan, H., Tang, R.: Transformation of amorphous calcium carbonate into aragonite. *Journal of Crystal Growth*, **343**, 62-67, 2012

Zidar, P., Drobne, D., Štrus, J.: Determination of moulting stages of *Porcellio scaber* (isopoda) for routine use. *Crustaceana*, **71** (6), 646-654, 1998